

Nanoscale Charge Conservation and Transfer in Quantum Dot Assembly

Lucy UiYeon Yoon

A dissertation submitted to the School of Engineering and Applied Science

University of Virginia

in partial fulfillment of the requirements for the degree of Doctor of Philosophy

Charlottesville, Virginia

August 2021

Abstract

Quantum dots (QDs) are nano-size building blocks that can be shaped and assembled to yield novel and tunable properties. They have drawn significant research interests in the last several decades due to the tremendous potential in engineering applications - their tunable optical and electronic properties as well as low-temperature and facile manufacturing processing conditions allow to compete with other materials in the fields of light-emitting diodes, photovoltaics, photodetectors, optical memories, etc.

In the first part of my thesis, I attempt to provide insights on understanding the impact of cation and anion interaction of an ionic ligand passivant to eradicate detrimental charge traps on perovskite (CsPbBr_3) QDs, thus minimizing charge loss. We focus, in this study, on the pairing of cation – anion by varying cation choice on the degree of defect passivation efficacy on CsPbBr_3 QD surface. In collaboration with computational calculations, we experimentally confirm that the photoluminescence quantum yield (PLQY) of CsPbBr_3 QD is substantially impacted by the pairing between cation and anion, validating our hypothesis.

In the second part of my thesis, I experimentally tackle, using dielectric constant of an antisolvent, as a reasonable metric to study the nucleation and growth of perovskite thin film. Our results, supported by the absorbance and ^{207}Pb -nuclear magnetic resonance (NMR) measurements, show that lower dielectric solvent environment promotes formation of methylammonium (MA^+) – iodoplumbate complexes, resulting in smaller grain size.

Lastly, I report the first proof-of-concept study on quantum tunneling induced exciton dissociation by varying potential barrier height in the photochromic molecule (PCM) bridged PbS QD assembly. The potential barrier height, defined as highest-occupied molecular orbital (HOMO)

or lowest unoccupied molecular orbital (LUMO) difference between the QD and photochromic molecule, can be swiftly varied via light-induced configuration switch of the PCM. Supported by a series of experiments, I corroborate that the quantum tunneling induced exciton dissociation in the PbS QD assembly occurs predominantly when the potential barrier height decreases upon closing the photochromic molecule's configuration. On the other hand, a radiative recombination acts as a dominant exciton relaxation pathway with larger potential barrier height, from the photochromic molecule's open configuration.

Dedication to

My husband, parents, brother, and grandmothers

Acknowledgement

I would like to express my foremost gratitude to Prof. Joshua J. Choi, my Ph.D. advisor for his unconditional support, guidance, and advice during my Ph.D. career. His patience and understanding allowed me to grow as a better researcher. I would also like to thank my committee members, Prof. Gary M. Koenig, Prof. Gaurav Giri, Prof. Seung-Hun Lee, and Prof. David L. Green for the keen insights from their various perspectives of research. I thank many brilliant colleagues, former and current lab members, Dr. Ben Foley, Dr. Alex Chen, Dr. Matt Alpert, Dr. Scott Niezgoda, Dr. Xiaoyu Deng, Kate Dagnall, Ashley Conley, Eric Holmgren, and Ephraiem Sarabamoun for the years of support and advice. I also had an invaluable experience to have collaborated with many outstanding people in and outside of UVa, including Dr. Hongxi Luo in Geise group at UVa, Michael Schapowal in Paolucci group at UVa, Blaire Sorenson in Clancy group at Johns Hopkins University, Surya Adhikari and Jonathan Bietsch in Wang group at Old Dominion University, and Esther Tsai in Brookhaven National Lab. Very special thanks to my colleagues whom I have shared and endured years of challenges together.

I would like to express my gratitude to my parents, who have made the life I live possible. I cannot merely grasp how difficult it was for them to give me the opportunity I have. Their utter trust in me was the driving force of my motivations in my life, and I am sincerely thankful for that. Lastly, none of my careers would have been realizable without an unconditional support, encouragement, care and love from my husband, James. It was his reassurance that I decided to pursue my Ph.D. and is still the sole reason that I am completing one. The words cannot describe how much I am grateful for his sacrifice and will continue to appreciate it. I cannot wait to see what the next chapter of our lives holds for us.

Table of Contents

Abstract	I
Acknowledgement	IV
Chapter 1: Introduction	1
1.1. Quantum Dots (QDs) properties and their applications	1
1.2. Exciton generation and recombination pathways in QD-based active layer	2
1.3. Perovskite-based QDs and major charge traps affecting device performance	3
1.4. Nanoscale charge transfer and electronic coupling in QD assembly	7
1.5. Quantum tunneling induced exciton dissociation in QD assembly	9
1.6. QD – photochromic molecule bridged system as an experimental platform to study the potential barrier height effect on exciton dissociation	11
1.7. Other exciton dissociation mechanisms in QD assembly	12
1.8. QD – photochromic molecule system for optical switching application	13
1.9. Reference	15
Chapter 2: The impact of cation and anion pairing in ionic salts on surface defect passivation in CsPbBr₃ NCs	18
2.1. Abstract	18
2.2. Introduction	18
2.3. Methods.....	21
2.3.1. Materials.....	21
2.3.2. Cesium oleate (Cs-oleate) synthesis	22
2.3.3. CsPbBr ₃ NCs synthesis	22

2.3.4.	Purification process of CsPbBr ₃ NCs	22
2.3.5.	X bromide (X = OLAm ⁺ , TriBAm ⁺ , DiBAm ⁺ , nBAm ⁺) ligands syntheses.....	23
2.3.6.	X-Y ionic salt (X = OLAm ⁺ , TriBAm ⁺ , DiBAm ⁺ , nBAm ⁺ ; Y = BA ⁻ , DFA ⁻) ligands preparation	24
2.3.7.	Optical characterization	24
2.3.8.	High-resolution transmission electron microscopy (HR-TEM), and X-ray Diffraction (XRD) characterizations.....	24
2.3.9.	Molecular dynamics simulations	25
2.3.10.	B3LYP calculations	25
2.4.	Results and Discussion	27
2.4.1.	NCs synthesis and characterization	27
2.4.2.	PLQY results.....	30
2.4.3.	NC size and PL lifetime measurement	33
2.4.4.	DFT calculations and analysis	35
2.5.	Conclusion.....	39
2.6.	Reference	41
2.7.	Supplementary Information.....	45
Chapter 3: A new metric to control nucleation and grain size distribution in hybrid organic-inorganic perovskites by tuning the dielectric constant of the antisolvent		
48		
3.1.	Abstract.....	48
3.2.	Introduction.....	49
3.3.	Methods.....	51
3.3.1.	DFT computational details	51

3.3.2.	Absorbance characterization	52
3.3.3.	²⁰⁷ Pb-NMR characterization	52
3.3.4.	Thin film fabrication	53
3.4.	Results and Discussion	53
3.4.1.	Solvent-antisolvent interactions.....	53
3.4.2.	Antisolvent-HOIP precursor interactions.....	55
3.4.3.	UV-Vis absorbance results analysis.....	59
3.4.4.	²⁰⁷ Pb-NMR results analysis	64
3.4.5.	Effect of antisolvent on grain sizes of MAPbI ₃ film	67
3.5.	Conclusion.....	70
3.6.	Reference	71
3.7.	Supplementary Information	75
3.7.1.	Solvent-antisolvent interaction	75
3.7.2.	Solvent-HOIP precursor interactions	75
3.7.3.	Effect of changing PbI ₂ concentration	76
3.7.4.	Effect of changing MAI concentration	76
3.7.5.	Effect of antisolvents of varying dielectric constant and increasing MAI concentration	77
3.7.6.	Fabricated thin films	78
Chapter 4: Exciton Dissociation in Quantum Dots Connected with Photochromic Molecule Bridges		81
4.1.	Abstract.....	81
4.2.	Introduction.....	81
4.3.	Methods.....	85

4.3.1.	Photochromic molecules (PCMs) syntheses	85
4.3.2.	PbS QD synthesis.....	89
4.3.3.	PCM treated PbS QD assembly preparation	89
4.3.4.	Absorbance, photoluminescence (PL), time-resolved photoluminescence (TR-PL) and Raman spectroscopy measurements	90
4.3.5.	PL measurements on PCM treated QD samples.....	90
4.3.6.	GISAXS measurement.....	91
4.4.	Results and Discussion	91
4.5.	Conclusion.....	101
4.6.	Reference	103
4.7.	Supplementary Information.....	111
4.7.1.	¹ H and ¹³ C NMR spectra of as-synthesized compound 6 (PCM) and compound 7 (mono-esterified PCM)	111
4.7.2.	Raman spectra for probing ligand exchange on PCM treated QD films	117
4.7.3.	Absorbance spectra of PCM bridged 3.6nm QD assembly with closed and open PCM state	117
4.7.4.	GISAXS scattering images and integrated intensity plots of 2.9 nm QD films with a closed and open PCM state.....	118
4.7.5.	The average inter-QD distance values of various QD size assemblies with open and closed PCM state	119
4.7.6.	Absorbance spectra of mono-esterified PCM (compound 7) in MeOH	119
4.7.7.	PL cycle of PCMs treated 3.6 nm QD solution sample	120
Chapter 5:	Conclusion	121

Chapter 1: Introduction

1.1. Quantum Dots (QDs) properties and their applications

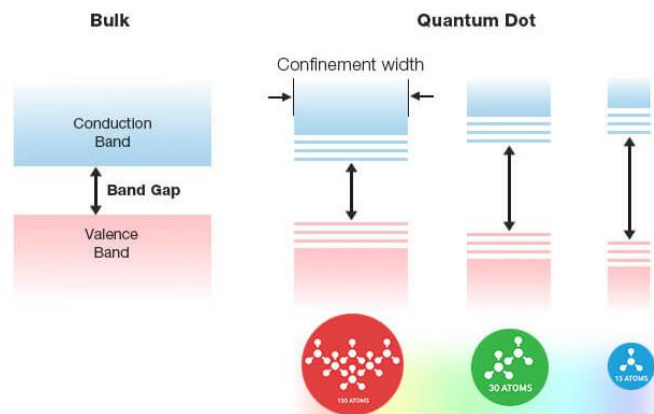


Figure 1. Illustration displaying the difference in electronic properties of bulk versus quantum confined particles. For quantum dots (QDs), smaller sizes result in stronger quantum confinement, yielding higher highest occupied molecular orbital (HOMO) – lowest unoccupied molecular orbital (LUMO) gap. Figure was adopted from reference 1.

Quantum dots (QDs) are nano-sized semiconductor particles that exhibit tunable optical and electronic properties due to quantum confinement in all three dimensions. Quantum confinement occurs when the dimension of the particle becomes on the order of magnitude or smaller than the exciton Bohr radius.² Subsequently, due to the presence of fewer atoms that make up individual QD, energy levels become more discrete. Their tunable optoelectronic properties arise from controlling a degree of quantum confinement, mainly by tuning the size and shape of QDs. In general, a degree of quantum confinement decreases as QD size increases – this results in photoluminescence (PL) emission with lower energy (higher wavelength) (Figure 1).

QDs have a wide range of applications based on their material properties. Some include photodetectors,³⁻⁴ lasers,⁵⁻⁶ optical memory switches,⁷ bio-imaging,⁸ photocatalysts,⁹

scintillators,¹⁰ etc. Particularly, QD based devices have shown remarkable advances in photovoltaics and light-emitting-diodes (LEDs) applications with their performance on par with the other competitive materials. Indeed, QD based applications have practical and economically viable advantages. For example, QDs have forgivable manufacturing process, relatively low synthesis temperature, and solution-processable.¹¹ Their highly controllable emission wavelength and full-width-half-max (FWHM) allow pure and saturated emission, allowing a greater displayable range of colors. Depending on the material choice, the emission range can easily be extended from deep ultra-violet (UV) to infrared (IR) region, making them more versatile for broader applications.

1.2. Exciton generation and recombination pathways in QD-based active layer

QDs are composed of only a few tens or hundreds of atoms attributing to a formation of discrete energy level. The difference in energy is equivalent of bandgap for bulk semiconductor material. Only when there is an energy equivalent or higher than the HOMO-LUMO gap, an electron from the HOMO is excited to LUMO. An excited electron can undergo relaxation through mainly two mechanisms: 1) radiative recombination during which photon emission takes place and 2) non-radiative recombination. Some non-radiative recombination processes include 1) trap-mediated recombination during which the remaining energy may dissipate as phonon and 2) auger recombination, where an excess energy is not used toward photon generation but instead to excite another carrier to excite to a higher energy state.

For application purpose, such as LEDs, it is very crucial to preserve the injected carriers to achieve radiative recombination as the number of photons is directly correlated to the device efficiency. In specific, the external quantum efficiency (EQE) of LEDs is proportional to the

number of emitted photons divided by the number of injected electrons. The injected charges may be lost in other layers before reaching to the active layer and could attribute to the device efficiency. However, a major charge loss likely occurs within the QD-based active layer due to i.e. traps that form on the QD surface.

QDs have nanometer dimensions that have substantially large surface area to volume ratio. For instance, 3 nm PbS QD has approximately 50% of all the atoms residing on the surface,¹² meaning, the surface condition may have a significant effect on carrier recombination mechanism. Many years of research support the importance of the surface chemistry of QDs (i.e. elements exposed on the surface and defects associated with them) and its impact on the optoelectronic device performance. Extensive studies continue to be done on understanding the type, nature, and characteristic of surface traps that detrimentally affect the charge conservation and transport. Having deeper insights on the nature of charge traps allows the innovative engineering approach to eliminating thus increasing device efficiency.

1.3. Perovskite-based QDs and major charge traps affecting device performance

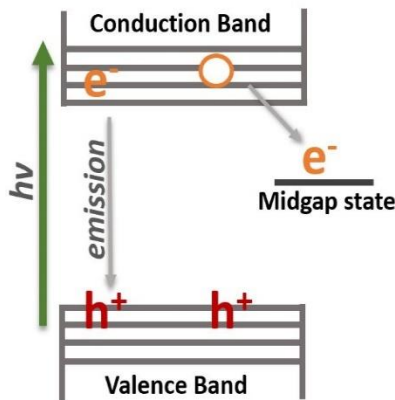


Figure 2. Schematic diagram showing the exciton radiative recombination (left) and trap-assisted non-radiative recombination (right). The remaining energy is generally dissipated as phonon upon relaxation.

Due to a predominant surface effect, surface defects serve as one of the main origins of the charge traps on the QD. In the QD electronic structure, these defects form midgap states between HOMO and LUMO; an excited electron, instead of falling back to recombine with hole in HOMO and emit photon, instead gets trapped in one of these midgap states (Figure 2). Depending on the nature of midgap state, a carefully selected ligand may effectively eradicate these defects, ultimately improving photoluminescence quantum yield (PLQY) of the QDs.

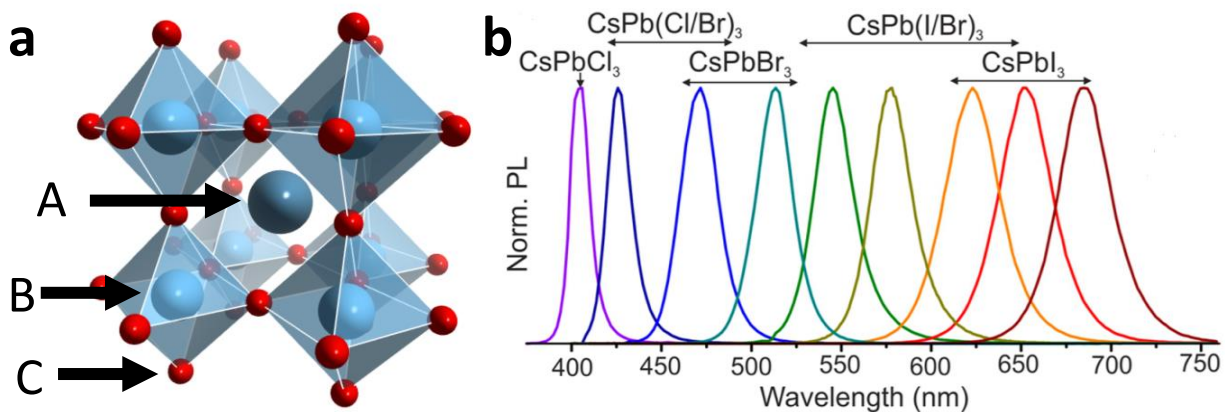


Figure 3. a) Perovskite crystal structure with A-site monovalent cation surrounded by four octahedra that has B-site divalent connected with six C-site halide atoms. b) PL emission spectra achieved by varying the halide composition in CsPbX_3 QDs. Figure 3b was adopted from reference 13.

The semiconductor material used for studying the surface chemistry – ligand interaction in this study is hybrid organic inorganic perovskite (HOIP). Perovskite material has a chemical structure of ABX_3 , where A is either an organic or inorganic monovalent cation ($\text{A} = \text{Cs}^+$,

methylammonium (MA^+), formamidinium (FA^+), B is a divalent cation (Pb^{2+} , Sn^{2+} , Ge^{2+}) and X is a halide ($\text{X} = \text{Cl}^-$, Br^- , I^-) (Figure 3a). Perovskite QDs have drawn tremendous attention in the research field due to their intrinsically defect-tolerant nature as well as narrow FWHM, highly suitable for the next-generation optoelectronic material. Simply changing the halide composition (Cl^- , Br^- , I^-) or using halide alloy composition allows formation of QD that essentially covers the entire visible light spectrum (400 – 700 nm) (Figure 3b). Perovskite based quantum-LED (QLED) has already achieved its record EQE efficiency of over 21% (specifically cesium lead bromide (CsPbBr_3) QD,¹⁴ on par with the record efficiency from CdSe based QDs (EQE = 22.9%)¹⁵.

To further improve the quantum efficiency by minimizing charge loss in the active layer, it is necessary to gain insights on the surface chemistry of perovskite QDs. To investigate the surface chemistry of perovskite QDs, De Roo *et al.*¹⁶ has done a systematic study using techniques such as $^1\text{H-NMR}$, Two-dimensional Diffusion Ordered Spectroscopy, and Nuclear Overhauser Effect Spectroscopy on QD surface – various ligands dynamics in solution state samples. Based on the experimental results, it was found that the main ligand dynamically interacting with the CsPbBr_3 surface is oleylammonium bromide (OLAmBr) as a pair of X-type ligands, among many other ligands presented in the solution (oleic acid (HOA), lead oleate, etc). The evidence was further supported by DOSY measurement, in which OLAmBr indeed showed much lower diffusion coefficient when introduced to QD dispersed solution compared to their free state. The discovery led to numerous other in-depth studies on finding optimal ligand for an effective surface defect passivation.

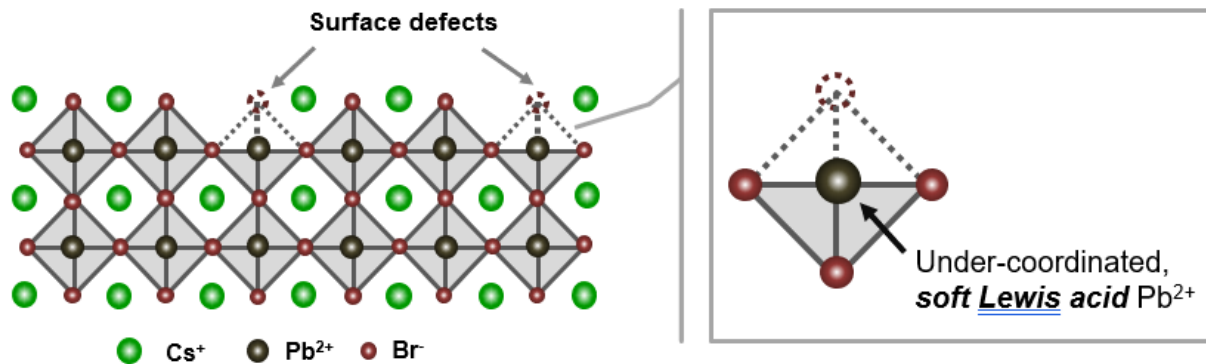


Figure 4. Schematic diagram of CsPbBr₃ QD surface displaying the types of surface defects. The dominant halide atomic vacancies leave the soft Lewis acid Pb²⁺ undercoordinated.

A combination of experimental and computational results in the recent research supports that the dominant charge traps on the CsPbBr₃ is the halide atomic vacancies on the surface (Figure 4). Nenon *et al.*,¹⁷ employed the spectroscopic techniques as well as *ab initio* calculations to confirm that the dominant charge traps are halide atomic vacancies, leaving Pb²⁺ undercoordinated (Figure 4). Based on this finding, a vital approach was proposed on finding softer, X-type Lewis base anion that can effectively coordinate with soft Lewis acid, under-coordinated Pb²⁺ atoms. Their experimental results show a general correlation between the Lewis basicity of the anion employed for defect passivation and PLQY of CsPbBr₃ QDs.

In Chapter 2, I present the work that used this study as a base model to elucidate the impact of pairing between cation and anion of the ionic ligand on the passivation efficiency. In the previous study, the role of cation was not extensively explored. The importance of halide atomic vacancies is sufficiently acknowledged, though due to charge neutrality, cation of the ionic ligand will need to partake in the passivation process as well. Based on our rationale that ionic ligand is not readily to dissociate in a highly non-polar QD solvent, I performed PLQY measurements using the ligands containing various Lewis base anions paired with cations that yield varying binding

strengths (when paired with anions) and attempted to rationalize the obtained results with our density functional theory (DFT) calculations.

1.4. Nanoscale charge transfer and electronic coupling in QD assembly

Nanoscale charge transfer from QD to QD in the assembly is as important for efficient devices as preserving generated carriers within QD. It has been reported in the past years that obtaining a strong electronic coupling between QDs is a crucial aspect of enhancing charge transfer. For LED device application, exciton binding energy (overlap integral of the electron and hole wavefunctions) higher than the coupling energy is needed. As such, a careful selection of surface ligands is required to maximize charge transfer across the active (QD) layer (i.e. replacing a long chain insulating ligand with a shorter ligand) but to minimize exciton dissociation (i.e. too short ligand may enhance exciton delocalization). Optimizing the electronic coupling between QDs for an engineering application by Sun *et al.*¹⁸ has led PbS QLED device with eight-fold increase in radiance compared to the previous champion result.

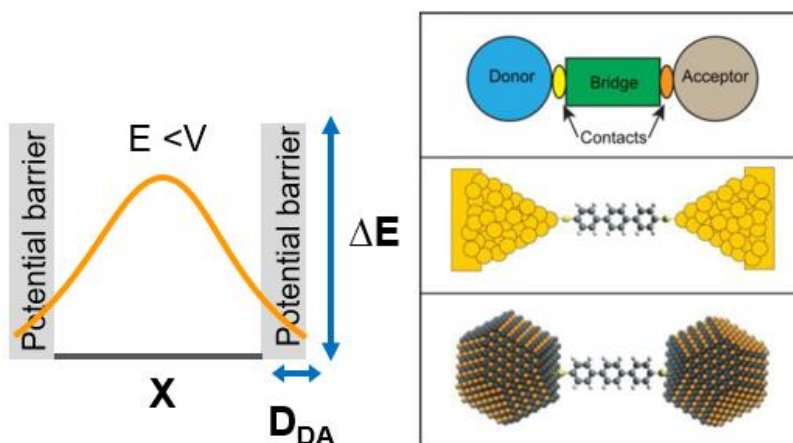


Figure 5. Illustration showing high electronic coupling induced electron wavefunction leakage as a result of finite potential barrier (ΔE) or inter-QD distance (D_{DA}) (left). Illustration of a donor – bridge – acceptor system signifying the nature of bridge molecules on the electronic coupling between the donor and the acceptor.

Electronic coupling occurs when QDs are well within proximity that their electronic wavefunctions interact to a greater extent or when the potential barrier, which is dictated by the electronic states between the QD and bridge molecule, decreases (Figure 5). Hence, the role of bridge molecules, the molecules that interconnect between the QDs, is very critical (Figure 5). Electron transfer rate and the relevant parameters for a non-adiabatic regime with weak electronic coupling between the QDs have been well explained by the fundamentals of Marcus theory¹⁹:

$$k_{et}(\text{electron transfer rate}) = \frac{2\pi}{\hbar} |H_{DA}|^2 \frac{1}{\sqrt{4\pi\lambda k_B T}} \exp\left[-\frac{\lambda + \Delta G^0}{4\lambda k_B T}\right] \quad \text{Equation 1}$$

H_{DA} is the electronic coupling between the initial and final state, \hbar is Planck's constant, λ is the reorganization energy representing the energy required to allow nuclei reorganization without an electron transfer, k_B is the Boltzmann constant, and ΔG^0 is the stand free energy of the electron transfer reaction. H_{DA} can be expressed using tunneling formula approximation and Wentzel-Kramers-Brillouin approximation of a finite square potential well²⁰:

$$H_{DA} = H^o_{DA} \exp\left[-\frac{\sqrt{2m\Delta E}}{\hbar} D_{DA}\right] \quad \text{Equation 2}$$

H^o_{DA} is the electronic coupling when the distance between the donor and acceptor is zero, ΔE is the potential barrier height, and D_{DA} is the inter-QD distance. As described in Equation 2, the electronic coupling has an exponential dependence on inter-QD distance and the square root of potential barrier height.

1.5. Quantum tunneling induced exciton dissociation in QD assembly

Quantum tunneling is one of the pathways of exciton dissociation. It is a non-classical quantum mechanical phenomenon that occurs due to a leakage of electron wavefunction outside of the potential barrier. This mechanism is favorable in the material system with high coupling energy and low exciton binding energy. Numerous studies^{18,21} have reported that the quantum tunneling induced exciton dissociation that validates the relationship described in Equation 2.

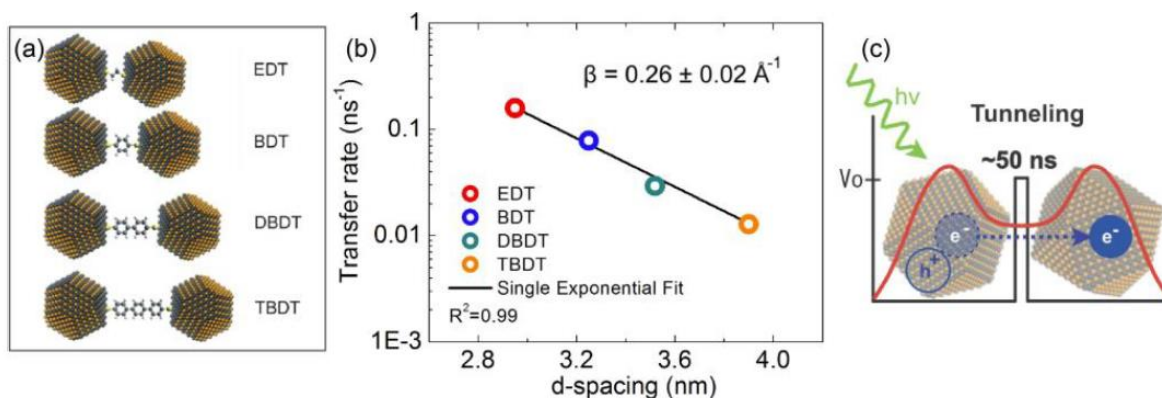


Figure 6. a) Schematic diagram of PbS QD bridged with variable length molecules: 1,2-ethanedithiol (EDT), 1,4-benzenedithiol (BDT), 4,4'-dibenzenedithiol (DBDT), and 4,4'-tribenzenedithiol (TBDT). b) A semi-log plot of charge transfer rate as a function of d-spacing; the relationship shows an exponential dependence of charge transfer rate on the inter-QD distance between QDs. c) A schematic diagram of delocalized wavefunction of QDs and quantum tunneling induced exciton dissociation.²¹ Figure was adopted from reference 21.

For example, tuning the inter-QD distance to control exciton dissociation rate has been extensively studied in QD – bridge molecule system. For the first time, Choi *et al.*²¹ performed a systematic experimental study aiming to elucidate inter-QD distance dependent exciton

dissociation in PbS QD assembly by varying the length of the bridge molecules (Figure 6). In agreement with the theoretical expectation, their experimental results supported that the rates varied exponentially with respect to the inter-QD distance. They further elucidated that the exciton dissociation mechanism is indeed tunneling through potential barrier between the QD and the bridge molecule, not other de-excitation pathways such as surface trapping, charge transfer to proximate molecule,²² or Förster resonance energy transfer (FRET)²³.

While there have been several other studies²⁴⁻²⁵ that reported very similar observations to Choi *et al.*'s findings,²¹ not much progress has been made on investigating other parameters that affect the charge transfer rate. For example, the potential barrier height (ΔE), the square root of which variable has an exponential dependence on charge transfer rate, has not been well-studied. This is particularly challenging to study because it is practically very difficult to change only the potential barrier height while keeping other variables constant. Varying the potential barrier height usually requires the bridge molecules with different HOMO-LUMO levels, which inevitably change many other factors that are affected by using different donor – acceptor pair and the surface chemistry at contact. For example, factors may include a degree of surface trapping (which will mostly depend on the end moiety of the bridge molecules), inter-QD distance (unless two comparable bridge molecules have the exactly the same length), etc.

1.6. QD – photochromic molecule bridged system as an experimental platform to study the potential barrier height effect on exciton dissociation

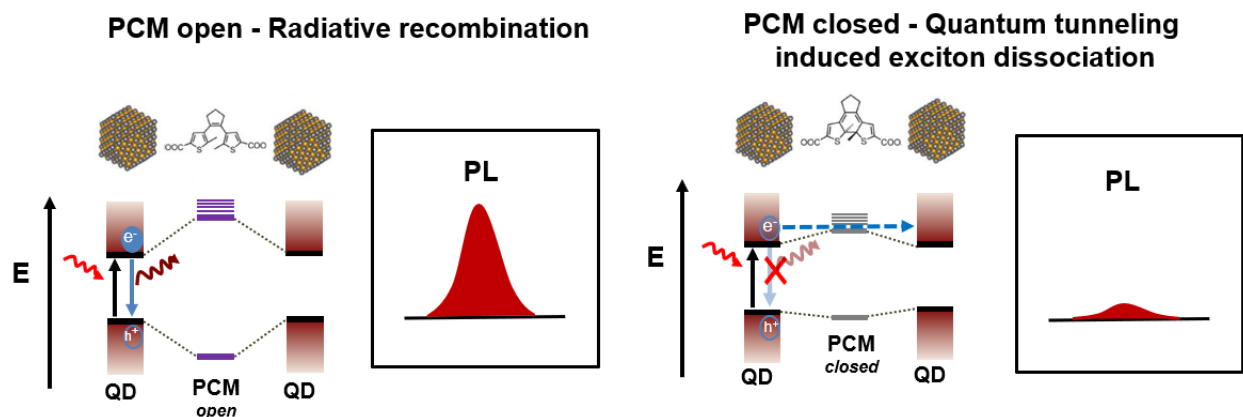


Figure 7. Illustration showing electronic structure of photochromic molecule (PCM) bridged QD with open PCM state. The dominant exciton relaxation pathway will be a radiative recombination (strong PL emission) when the potential barrier height is large (left). On the right, the dominant exciton relaxation pathway is a quantum tunneling induced exciton dissociation as a result of small potential barrier height upon a closed PCM state.

In our study, we take an advantage of photochromic molecule, as a bridge molecule, that changes its configuration upon different light exposure. Upon the configurational change, the molecule goes under electronic transition with a few electronvolts difference. As depicted in Figure 7, the general idea is that when the photochromic molecule is in a closed configurational state upon UV light exposure, its HOMO-LUMO gap decreases and as a result the potential barrier height between the QD (donor) and the photochromic molecule (bridge) decreases, allowing tunneling induced exciton dissociation as a dominant exciton relaxation pathway. On the other hand, when the photochromic molecule is in an open state upon visible light (~540 nm) exposure,

its HOMO-LUMO gap increases and therefore the potential barrier height increases. As a result, an exciton radiative recombination will be a dominant exciton relaxation pathway.

Photochromic molecule bridged QD assembly will serve as a great experimental platform for studying the potential barrier height parameter on the nanoscale charge transfer rate because the measurements can be done on the same exact sample with exactly the same QD population (and QD size distribution), QD surface chemistry, a degree of QD surface trapping, QD-PCM contact, any variability / heterogeneity that the sample (or the spot within the sample) inevitably can have. This is because this experimental platform needs only different light exposure to vary the main variable, potential barrier height, as a result of configurational change of the photochromic molecule. More details of the work will be discussed in Chapter 3.

1.7. Other exciton dissociation mechanisms in QD assembly

Exciton dissociation could occur via other mechanisms depending on the electronic structure of the QDs as well as their interaction with the bridge molecules. Two main mechanisms discussed in this section are PET and FRET.

PET from the QD to the bridge molecule may occur when the LUMO of the bridge molecule lies below that of the QD. Similarly, if the HOMO of the bridge molecule lies above that of the QD, hole transfer will take place. FRET occurs due to a dipole – dipole interaction between the donor and the acceptor when they are within proximity. The condition to satisfy for this energy transfer to occur is the overlap of a wavelength region between the PL of the donor and the absorption of the acceptor. The degree of FRET is also inversely correlated with the sixth power of the distance between the donor and the acceptor.

1.8. QD – photochromic molecule system for optical switching application

The two mechanisms mentioned in the previous section, yielding PL on/off cycle, are widely used for optical switching and data storage applications, which require durable optical switching cycle capability, high temperature endurance, fast switching speed, etc.

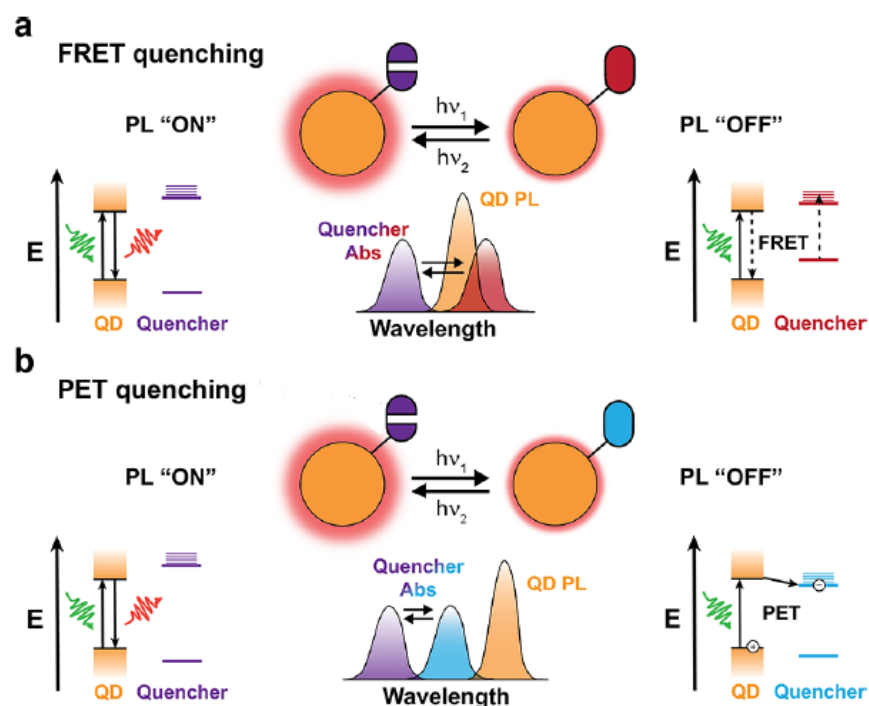


Figure 8. Illustration showing difference between FRET and PET quenching for PL on/off cycles in optical switching applications. Both mechanisms involve an inevitable spectral overlap between the QD PL emission and the photochromic molecule absorption, detrimentally affecting optical switch readout capability. Figure was adopted from reference 26.

As depicted in Figure 8, the current challenge involved with both mechanisms (PET with a lesser degree) is that due to an overlap of a ‘write/erase’ and ‘read’ wavelength regions, the readout capability of such systems is self-destructive, thus highly inefficient. Our system that uses

quantum tunneling induced PL on/off essentially solves this problem because of a large wavelength gap between QD PL emission and the photochromic molecule absorption region (Figure 9).

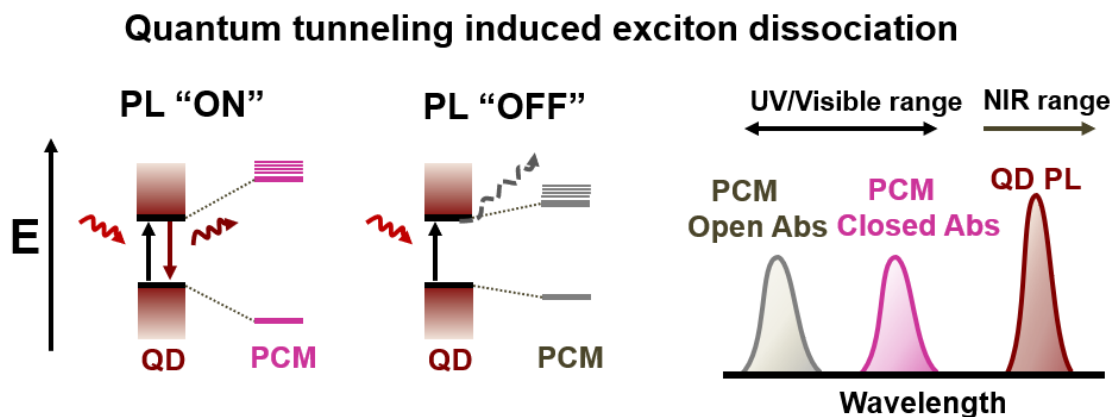


Figure 9. Schematic diagram depicting our novel QD – photochromic molecule system with PL on/off behavior based on quantum tunneling induced exciton dissociation. Unlike PET or FRET based system, there is no spectral overlap between QD PL emission and photochromic molecule absorption region.

1.9. Reference

1. Quantum Dot Physics: A Guide to Understanding QD Displays. <
<https://pid.samsungdisplay.com/en/learning-center/white-papers/guide-to-understanding-quantum-dot-displays>> (2021).
2. Roduner, E., Size matters: why nanomaterials are different. *Chemical Society Reviews* **2006**, *35* (7), 583-592.
3. Barve, A. V.; Lee, S. J.; Noh, S. K.; Krishna, S., Review of current progress in quantum dot infrared photodetectors. *Laser & Photonics Reviews* **2010**, *4* (6), 738-750.
4. Stiff-Roberts, A. D., Quantum-dot infrared photodetectors: a review. *Journal of Nanophotonics* **2009**, *3* (1), 031607.
5. Park, Y.-S.; Roh, J.; Diroll, B. T.; Schaller, R. D.; Klimov, V. I., Colloidal quantum dot lasers. *Nature Reviews Materials* **2021**, *6* (5), 382-401.
6. Norman, J. C.; Jung, D.; Zhang, Z.; Wan, Y.; Liu, S.; Shang, C.; Herrick, R. W.; Chow, W. W.; Gossard, A. C.; Bowers, J. E., A review of high-performance quantum dot lasers on silicon. *IEEE Journal of Quantum Electronics* **2019**, *55* (2), 1-11.
7. Asakawa, K.; Sugimoto, Y.; Watanabe, Y.; Ozaki, N.; Mizutani, A.; Takata, Y.; Kitagawa, Y.; Ishikawa, H.; Ikeda, N.; Awazu, K., Photonic crystal and quantum dot technologies for all-optical switch and logic device. *New Journal of Physics* **2006**, *8* (9), 208.
8. Bilan, R.; Nabiev, I.; Sukhanova, A., Quantum dot-based nanotools for bioimaging, diagnostics, and drug delivery. *ChemBioChem* **2016**, *17* (22), 2103-2114.
9. Sharma, S.; Dutta, V.; Singh, P.; Raizada, P.; Rahmani-Sani, A.; Hosseini-Bandegharai, A.; Thakur, V. K., Carbon quantum dot supported semiconductor photocatalysts for efficient degradation of organic pollutants in water: a review. *Journal of Cleaner Production* **2019**, *228*, 755-769.
10. Bertrand, G. H.; Hamel, M.; Sguerra, F., Current status on plastic scintillators modifications. *Chemistry—A European Journal* **2014**, *20* (48), 15660-15685.
11. Sanderson, K., Quantum dots go large. Nature Publishing Group: 2009.

12. Kovalenko, M. V., Opportunities and challenges for quantum dot photovoltaics. *Nature nanotechnology* **2015**, *10* (12), 994-997.
13. Protesescu, L.; Yakunin, S.; Bodnarchuk, M. I.; Krieg, F.; Caputo, R.; Hendon, C. H.; Yang, R. X.; Walsh, A.; Kovalenko, M. V., Nanocrystals of cesium lead halide perovskites (CsPbX₃, X= Cl, Br, and I): novel optoelectronic materials showing bright emission with wide color gamut. *Nano letters* **2015**, *15* (6), 3692-3696.
14. Fang, T.; Wang, T.; Li, X.; Dong, Y.; Bai, S.; Song, J., Perovskite QLED with an external quantum efficiency of over 21% by modulating electronic transport. *Science Bulletin* **2021**, *66* (1), 36-43.
15. Shen, H.; Gao, Q.; Zhang, Y.; Lin, Y.; Lin, Q.; Li, Z.; Chen, L.; Zeng, Z.; Li, X.; Jia, Y., Visible quantum dot light-emitting diodes with simultaneous high brightness and efficiency. *Nature Photonics* **2019**, *13* (3), 192-197.
16. De Roo, J.; Ibáñez, M.; Geiregat, P.; Nedelcu, G.; Walravens, W.; Maes, J.; Martins, J. C.; Van Driessche, I.; Kovalenko, M. V.; Hens, Z., Highly dynamic ligand binding and light absorption coefficient of cesium lead bromide perovskite nanocrystals. *ACS nano* **2016**, *10* (2), 2071-2081.
17. Nenon, D. P.; Pressler, K.; Kang, J.; Koscher, B. A.; Olshansky, J. H.; Osowiecki, W. T.; Koc, M. A.; Wang, L.-W.; Alivisatos, A. P., Design principles for trap-free CsPbX₃ nanocrystals: enumerating and eliminating surface halide vacancies with softer Lewis bases. *Journal of the American Chemical Society* **2018**, *140* (50), 17760-17772.
18. Sun, L.; Choi, J. J.; Stachnik, D.; Bartnik, A. C.; Hyun, B.-R.; Malliaras, G. G.; Hanrath, T.; Wise, F. W., Bright infrared quantum-dot light-emitting diodes through inter-dot spacing control. *Nature nanotechnology* **2012**, *7* (6), 369-373.
19. Adams, D. M.; Brus, L.; Chidsey, C. E.; Creager, S.; Creutz, C.; Kagan, C. R.; Kamat, P. V.; Lieberman, M.; Lindsay, S.; Marcus, R. A., Charge transfer on the nanoscale: current status. *The Journal of Physical Chemistry B* **2003**, *107* (28), 6668-6697.

20. Luisier, M.; Klimeck, G., Simulation of nanowire tunneling transistors: From the Wentzel–Kramers–Brillouin approximation to full-band phonon-assisted tunneling. *Journal of Applied Physics* **2010**, *107* (8), 084507.
21. Choi, J. J.; Luria, J.; Hyun, B.-R.; Bartnik, A. C.; Sun, L.; Lim, Y.-F.; Marohn, J. A.; Wise, F. W.; Hanrath, T., Photogenerated exciton dissociation in highly coupled lead salt nanocrystal assemblies. *Nano letters* **2010**, *10* (5), 1805-1811.
22. Tvrdy, K.; Frantsuzov, P. A.; Kamat, P. V., Photoinduced electron transfer from semiconductor quantum dots to metal oxide nanoparticles. *Proceedings of the National Academy of Sciences* **2011**, *108* (1), 29-34.
23. Medintz, I. L.; Hildebrandt, N., *FRET-Förster resonance energy transfer: from theory to applications*. John Wiley & Sons: 2013.
24. Nakazawa, N.; Zhang, Y.; Liu, F.; Ding, C.; Hori, K.; Toyoda, T.; Yao, Y.; Zhou, Y.; Hayase, S.; Wang, R., The interparticle distance limit for multiple exciton dissociation in PbS quantum dot solid films. *Nanoscale horizons* **2019**, *4* (2), 445-451.
25. Xu, F.; Gerlein, L. F.; Ma, X.; Haughn, C. R.; Doty, M. F.; Cloutier, S. G., Impact of different surface ligands on the optical properties of PbS quantum dot solids. *Materials* **2015**, *8* (4), 1858-1870.
26. Padgaonkar, S.; Eckdahl, C. T.; Sowa, J. K.; López-Arteaga, R.; Westmoreland, D. E.; Woods, E. F.; Irgen-Gioro, S.; Nagasing, B.; Seideman, T.; Hersam, M. C., Light-Triggered Switching of Quantum Dot Photoluminescence through Excited-State Electron Transfer to Surface-Bound Photochromic Molecules. *Nano letters* **2021**, *21* (1), 854-860.

Chapter 2: The impact of cation and anion pairing in ionic salts on surface defect passivation in CsPbBr₃ NCs

This chapter was adopted from the published work: *Journal of Materials Chemistry C* **2021**, 9, 991-999.

2.1. Abstract

Imperfect passivation of surface charge traps on metal halide perovskite (MHP) nanocrystals remains a key obstacle to achieving higher performance in optoelectronic devices. Due to the strong ionic nature of MHPs, ionic salts have been identified as effective surface charge trap passivating ligands. In this study, based on photoluminescence quantum yield (PLQY) and time-resolved photoluminescence (TRPL) measurements on cesium lead bromide nanocrystals (CsPbBr₃ NCs), we find that the pairing between cation and anion of an ionic salt results in a significant impact on trap passivation. Using density of functional theory (DFT) calculations, we identify the binding interaction between the cation and anion of the ionic pair to be a major factor in determining the trap passivation efficacy.

2.2. Introduction

Metal halide perovskites (MHPs) are promising semiconductors for a wide variety of optoelectronic applications including photovoltaics, light-emitting diodes (LEDs), photodetectors, and lasers.¹⁻⁶ MHPs combine superb optical and electrical properties with the possibility of low-cost solution based manufacturing.^{3, 7-15} Properties of MHPs such as the widely tunable bandgap, narrow full-width-half-maximum (FWHM) emissions, and

bright photoluminescence (PL) with a versatility of low-temperature processing conditions¹⁶⁻¹⁹ are essential features for the advancement of (LED) technology, which requires highly saturated color displays, lower manufacturing costs, and high quantum efficiency.²⁰⁻²³ Among the various MHPs, cesium lead halide perovskites (CsPbX_3) are promising for practical device applications due to their intrinsic stability^{16, 24-28} and defect-tolerant nature. In particular, CsPbBr_3 nanocrystals (NCs) have shown superior optical properties including near-unity photoluminescence quantum yield (PLQY),^{29, 30} sharp PL emission peak,³¹ and a highly saturated color emission. Recently, CsPbBr_3 NCs-based LEDs have shown encouraging progress with their performance exceeding an external quantum efficiency (EQE) of 16%.³²

Despite the promising potentials, a further increase in the performance of MHP NC-based optoelectronic devices is currently limited by non-radiative electron-hole recombination at trap sites on the NC surfaces.³³⁻³⁹ One facile yet effective solution to this challenge is a post-synthesis surface treatment with trap passivating ligand molecules.⁴⁰⁻⁴⁷ Depending on the nature of defect sites on the surface, various types of ligands^{31, 48} can be employed to improve trap passivation. Charge neutral Lewis base L-type ligands bind with a Lewis acid site on the NC surface by donating an electron pair. Conversely, charge neutral Lewis acid Z-type ligands bind with a Lewis base on the NC surface by accepting an electron pair. Due to a strong ionic nature of MHP surface, ionic salts^{47, 49-53} recently have been studied as trap passivating ligands. Cation and anion of ionic salts behave as charged X-type ligands which passivate charge traps by either donating or accepting an electron to under-coordinated surface atoms. Despite of all the studies so far, precise mechanisms

through which ligands and MHP surface interact are still not well understood and methods of selecting effective ligand species for particular MHP surfaces remain elusive.

In order to optimize MHP NC surface – ligand interactions for superior charge trap passivation, the surface environment and the defect properties of NCs must be understood. A collection of studies^{53, 54} on Pb-based MHPs has reported that a majority of the detrimental surface charge traps is based on halide vacancies. In order to eradicate these detrimental defects, exposed Pb^{2+} , an under-coordinated atom due to absence of halides, needs to be coordinated with a counterion. As such, finding an anion with effective binding affinity to Pb^{2+} is an essential aspect to improving charge trap passivation. One study recently proposed that the Lewis basicity of anion in ionic salt plays a crucial role in trap passivation and used Hard-Soft Acid-Base theory as a guiding principle to discover that soft Lewis base anion binds best with soft Lewis acid Pb^{2+} *via* coordinative bonding.⁵³

While halide vacancies serve as detrimental trap sites and appear to have the most eminent effect on non-radiative recombination, other vacancies, such as monovalent cations are still present. Yet, computational studies^{54, 55} suggest that their defect energy levels are likely to either lie outside of the MHP bandgap or are too shallow to serve as significant charge traps. For that reason, the choice of cation and the cation – anion pairing have not yet been carefully taken into consideration when selecting an ionic pair as charge passivating ligands. Although passivation *via* binding of cations directly onto the MHP surface may not directly result in any significant charge trap passivation, we believe that the dissociation ability of the cation – anion pair into ionic species will be an important factor as ionic salts need to initially dissociate into ions for them to act as X-type ligands.

Therefore, we hypothesize that the binding affinity of cation and anion pairing has a significant impact on surface charge trap passivation in MHP NCs.

Here, we study the relationship between cation-anion pairing in ionic salts and their efficacy in passivating surface charge traps in CsPbBr₃ NCs. CsPbBr₃ is the most widely studied composition in MHP NC field and is a great model system for this work. Our PLQY and PL lifetime results show that, given the identical anions, their pairing with different cations has a major impact on the degree of surface trap passivation. Our systematic comparison across different cation and anion pairs shows that certain anions can passivate traps well regardless of cations while other anions require pairing with specific cations for effective trap passivation. Using density functional theory (DFT) calculations, we identify the varying interaction energies of the cation – anion pair combinations to be a major factor resulting in the observed differences in trap passivation efficacy.

2.3. Methods

2.3.1. Materials

Cesium carbonate (Cs₂CO₃, 99.9%), octadecene (ODE, 90%), oleic acid (HOA, >99%), oleylamine (OLAm, 70%), anhydrous dimethyl sulfoxide (DMSO, 99.9%) were purchased from Sigma-Aldrich. Lead bromide (PbBr₂, >99.99%) was purchased from TCI America. Cesium bromide (CsBr, >99.999%) was purchased from Alfa Aesar. Tetrabutylammonium bromide (TeBAmBr, >98%), tributylamine (>99%), dibutylamine (>99.5%), n-butylamine (99.5%), acetic acid (>99.85%), benzoic acid (>99.5%), difluoroacetic acid (98%), hydrobromic acid (HBr, 48%), and tetrabutylammonium hydroxide solution (TeBAmOH, 40 wt.% in H₂O) were purchased from Sigma-Aldrich and used as received.

2.3.2. Cesium oleate (Cs-oleate) synthesis

Using Schlenk line setup, 0.407 g of Cs_2CO_3 , 20 mL of ODE, 1.25 mL of HOA were placed in 100 mL three neck round flask. Under vacuum, the flask was heated at 120 °C for 1 hour to evaporate mostly water and impurities. Under Argon, the temperature was heated to 150 °C and solution was stirred until all Cs_2CO_3 is dissolved. The final concentration of Cs-oleate is approximately 0.12 M. The final product needs to be heated prior to use as it often precipitates at room temperature.

2.3.3. CsPbBr₃ NCs synthesis

0.207 g (0.564 mmol) PbBr_2 , 1.5 mL HOA, 1.5 mL OLAm and 15 mL of ODE were placed in 100 mL three neck round flask. Under vacuum, solution was constantly stirred at 110 °C for 1 hour until all PbBr_2 forms complexes with HOA and OLAm. Under Argon, temperature was raised to 180 °C at which preheated 1.2 mL Cs-oleate (1.4 mmol) was swiftly injected. The reaction took place about 5 s, immediately followed by quenching with an ice bath. The resulting NCs are highly luminescent. NCs were cannula-transferred to prevent ambient exposure and then brought into the glovebox for further purification.

2.3.4. Purification process of CsPbBr₃ NCs

To ensure most of excess ligands, by-products, and unreacted species were removed, an extensive purification process was performed. The crude solution was centrifuged at 6k rpm for 45 min and the strongly colored supernatant is discarded. 5 mL of each methyl acetate (MeAc) and toluene were added to disperse NCs. The solution was centrifuged at 6k rpm for 15 min and the

colored supernatant is discarded again. NCs were dispersed in 5 mL toluene, along with an addition of 200 μ L of dried HOA and OLAm. Another 5 mL of MeAc added and the solution was centrifuged again. The less colored supernatant was discarded this time. The previous procedure was repeated once more but only with an addition of 75 μ L of HOA and OLAm. After centrifuging, the supernatant was removed. The NCs were dispersed once more in 5 mL toluene, centrifuged at 3k rpm for 3 min. The final supernatant was collected and stored in the glovebox.

For gentle purification process, the crude solution was centrifuged at 6k rpm for 45 min and the supernatant was discarded. 5 mL of toluene was added once again and the solution was centrifuged at 3 krpm for 3 min. Strongly colored supernatant was collected.

2.3.5. X bromide (X = OLAm⁺, TriBAm⁺, DiBAm⁺, nBAm⁺) ligands syntheses

48% aqueous HBr and 10 mol % excess amine were reacted in ethanol and stirred overnight. H₂O introduced from aqueous HBr was removed by the rotary evaporator. The condensed product was introduced in excess diethyl ether and placed in a freezer at -20 °C until salt was reprecipitated while unreacted amine stayed dissolved in diethyl ether. This procedure was repeated twice more to yield highest purity. The finally filtered salts were further dried in a vacuum oven at room temperature.

2.3.6. X-Y ionic salt (X = OLAm⁺, TriBAm⁺, DiBAm⁺, nBAm⁺; Y = BA⁻, DFA⁻) ligands preparation

Ligand solutions that do not need to be directly synthesized were prepared by simple mixing. Amines and acids were placed in anhydrous toluene (in which solvent that CsPbBr₃ NCs are dispersed) and stirred overnight in the glovebox.

2.3.7. Optical characterization

NC solution was sealed in a 1 mm path length quartz cuvette for optical measurements. Toluene in a cuvette was taken as a blank. PerkinElmer Lambda 950S spectrophotometer was used for absorbance measurement. PTI Quantamaster 400 system was used for photoluminescence measurement. For relative PLQY measurement, fluorescein (99%, Sigma-Aldrich) dispersed in 0.1 M sodium hydroxide in ethanol was used as a standard dye. For TRPL measurement, time correlated single photon counting setup (TCSPC) was used on QM-400 system to measure lifetimes with 433 nm laser diode as a light source. The lifetimes and their values are listed in Table S1 in Electronic Supplementary Information.

2.3.8. High-resolution transmission electron microscopy (HR-TEM), and X-ray Diffraction (XRD) characterizations

FEI Titan 80-300 TEM with 300 kV voltage was used for high-resolution TEM images. XRD was taken using a Malvern PANalytical Empyrean system with 40 kV and 40 mA.

2.3.9. Molecular dynamics simulations

Ab-initio molecular dynamics was performed to sample structures (for subsequent geometry optimization) for each of the isolated cations and ion-pairs using the Perdew-Burke-Ernzerhof (PBE) exchange-correlation form of the generalized gradient approximation (GGA).⁵⁶ The calculations were performed using version 5.4.4 of the Vienna Ab Initio Simulation Package (VASP).⁵⁷ The NVT ensemble was used with a Nose-Hoover thermostat. AIMD was performed at 373K and 0.5 fs time steps for a minimum of 2 ps. The calculations were spin-polarized with a plane-wave cut-off of 400 eV (chosen due to the presence of C, N, O, and F in some complexes), and an energy convergence criterion of 10^{-4} eV, and we considered only the Γ point for sampling the first Brillouin zone. For OLA⁺, 22 Å of vacuum was added in all directions, 18 Å for TriBA⁺, and 16 Å for DiBA⁺. The five minimum energy structures, spaced apart by at least 50 fs, were visually compared, and the lowest energy structures with unique conformations were selected for subsequent geometry optimizations. We emphasize that the sole purpose of the planewave AIMD simulations was to sample structures that were then optimized per the method described below.

2.3.10. B3LYP calculations

Individual ion structures and the selected ion-pair structures were optimized using B3LYP/aug-cc-pvtz and the Gaussian software.⁵⁸ The structures were optimized with ‘tight’ convergence, to a root mean square force of 5.1×10^{-4} eV/Å and max force of 7.7×10^{-4} eV/Å, and a root mean square displacement of 2.1×10^{-5} Å and a maximum displacement of 3.2×10^{-5} Å. We chose B3LYP for its reasonable performance for covalent and non-covalent interactions of small molecules.⁵⁹ To test the effect of our choice of computational method on ion pair energetics, we also performed

calculations using B3LYP/ aug-cc-pvtz and the D3 dispersion correction with Becke-Johnson dampening (D3(BJ)),⁶⁰ and the ω B97X-D hybrid-exchange functional,⁶¹ and MP2⁶² calculations for select Ion pairs. We found that the trend in energies with respect to the identity of the anion remained the same (Table S3-S5 in Electronic Supplementary Information) across all methods tested. All structure files from final optimized geometries are attached in the *Ionic pairs molecular structure* attachment file.

2.4. Results and Discussion

2.4.1. NCs synthesis and characterization

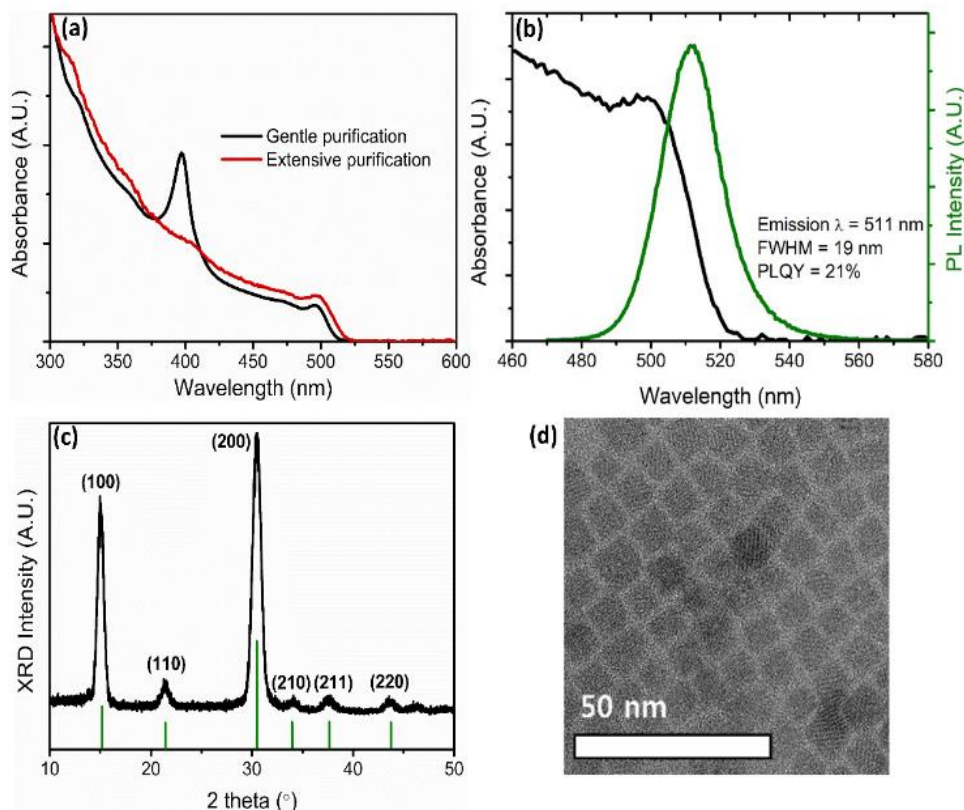


Figure 1. (a) Absorbance spectra of two differently purified CsPbBr₃ NCs with (OLAm⁺)(Br⁻) treatment. NCs prepared with gentle purification show a peak at around 390 nm upon ligand treatment, indicating a formation of other complex species. (b) Absorbance and PL spectra of CsPbBr₃. (c) XRD patterns indicating cubic phase of CsPbBr₃ NCs (d) TEM image showing an average NC size of 7.9 ± 1.4 nm.

For this study, it is beneficial to prepare NCs with a minimum number of native surface ligands while still keeping NCs colloidally stable. This is to more clearly elucidate the interactions between the ligand species of interest and the NC surface. Indeed, NCs with *gentle* purification processes (see Purification process of CsPbBr₃ NCs in Experimental section) showed complications upon ligand treatment likely due to significant amount of

various species including Pb-oleate, unreacted species, and excess native ligands such as OLAm and HOA. As shown in Figure 1a, ligand treated NCs with *gentle* purification show a peak in light absorbance at around 390 nm. The peak is at much lower wavelength than 503 nm, the first excitonic absorption peak of CsPbBr₃ NCs. This is likely due to light absorption by MHP precursor complexes, formed between unreacted precursor and ligands, that are much smaller than the size of NCs. NCs with the *extensive* purification process demonstrate consistent absorbance spectra with no additional peaks, suggesting that they have cleaner surface system for our ligand – surface interaction study. Therefore, for this study, control (as-synthesized) NCs were placed under *extensive* purification processes to remove the excess ligands and unreacted species.

Figure 1 provides characterization results of the extensively purified NCs prior to ligand treatment. Figure 1b features absorbance and PL spectra. The PL peak is located at 511 nm with FWHM of 19 nm. The relatively low PLQY value of 21% compared to the values typically reported in the literature^{31, 53} is due to removal of native ligands as much as possible during the extensive purification step. Figure 1c displays X-ray diffraction (XRD) peaks at 16° and 32° corresponding to strong orientations of (100) and (200) planes parallel to the substrate, respectively. The peaks of (110) at 22°, (210) at 34°, (211) at 37° and (220) at 44° are also in a good agreement with CsPbBr₃ without any detectable presence of impurities.²⁶ Based on transmission electronic microscope (TEM) images (Figure 1d), the average size of NCs is measured to be 7.9 ± 1.4 nm which is consistent with the absorbance and PL peak wavelengths.⁶³ These characterization results confirm that CsPbBr₃ NCs were successfully prepared as the base system for ligand treatment study.

A study by Neron *et al.*⁵³ suggests that the interaction between the anion of an ionic salt and under-coordinated Pb^{2+} plays a significant role in passivation efficacy. Particularly, the degree of match between the Lewis basicity of the anion and the soft Lewis acid Pb^{2+} sites seems to be a major factor in charge trap passivation efficacy on CsPbBr_3 NC surface. Based on those findings, we selected a range of anions with various Lewis basicity that previously showed widely different degrees of trap passivation: bromide (Br^-), difluoroacetate (DFA^-), and benzoate (BA^-). A set of cations was chosen to yield various interaction energies when paired with the anions: oleylammonium (OLAm^+), n-butylammonium (nBAm^+), dibutylammonium (DiBAm^+), tributylammonium (TriBAm^+), tetrabutylammonium (TeBAm^+). Cations with differing numbers of carbon chains were selected to alter the electron density around nitrogen of cation, and thus its binding strength with the anions. Each cation and anion were matched to form total of 15 pairs of ionic salts to study their effect on trap passivation in CsPbBr_3 NCs.

2.4.2. PLQY results

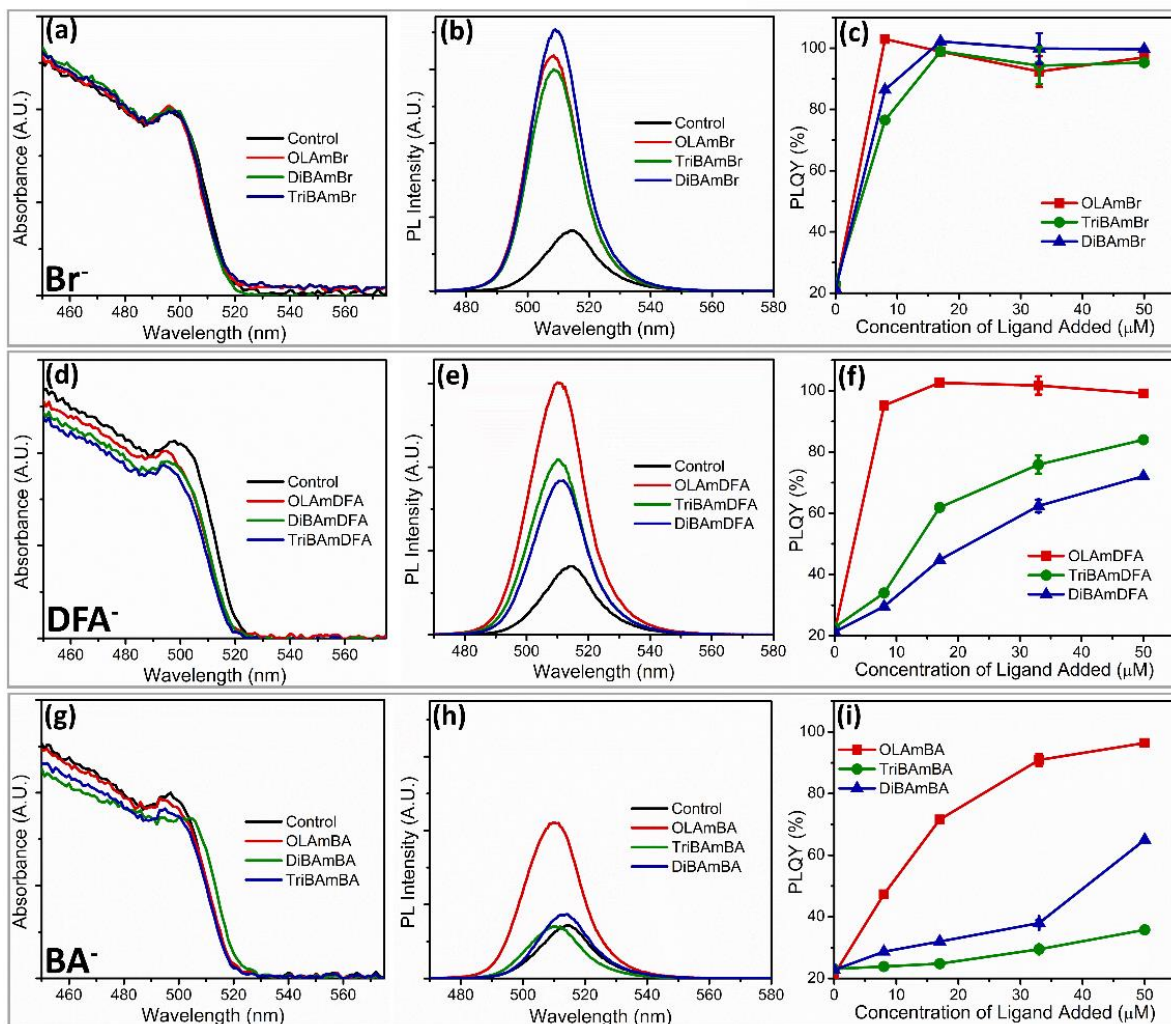


Figure 2. (a, d, h) Absorbance spectra of NCs treated with $33 \mu\text{M}$ of various cation – anion pairs. Each row represents the data from a set of various salt with the same anion. (b, e, h) PL spectra of the corresponding samples. Varying degrees of PL intensity with respect to that of untreated control NCs is observed depending on the combination of anion and cation. (c, f, i) PLQYs as a function of concentration of ligand treated on NCs show a clear dependence on each cation and anion.

The absorbance, PL, and PLQY results of NCs treated with various cation – anion pairs are displayed in Figure 2. Absorbance spectra in Figure 2a, d, and g show relatively minimal shifts and changes in magnitude, indicating a negligible change in energy levels and population of NCs in the solution due to ligand treatment. However, their PL spectra show significant variations in intensities depending on specific combination of cation and anion (Figure 2b, e, and h). Our PL results suggest that a degree of trap passivation strongly depends on both cation and anion of choice. In the case of the Br⁻ anion set, all treatment with OLAm⁺, DiBAm⁺, and TriBAm⁺ pairs resulted in superb passivation, yielding PLQY values of over 95%. In other words, there is no appreciable dependence of PLQY on the cation when paired with the Br⁻ anion. These results imply that, first, the extra Br⁻ anions from the introduced ionic salt effectively fill in the Br⁻ vacancies on CsPbBr₃ NC surface. Second, the interaction energy of all cation – Br⁻ pairs may be low such that sufficient amount of charged X-type ligands successfully passivates detrimental defects. Lastly, all OLAm⁺, DiBAm⁺, and TriBAm⁺ cations do not inherently possess compatibility issues such as steric hindrance with CsPbBr₃ NC surface.

DFA⁻ has been recently discovered as a promising charge trap passivating anion for Br⁻ vacancy on CsPbBr₃ NC surface.⁵³ Based on energy level calculations, PLQY, and ¹H-nuclear magnetic resonance (NMR) results, Nenon *et al.*⁵³, found that the soft Lewis basicity of DFA⁻ matches well with soft Lewis acidity of Pb²⁺ and can serve as an effective trap passivating agent.⁵³ Our results also show that DFA⁻, when paired with OLAm⁺, show superior passivation (Figure 2f). However, interestingly, we found that the passivation efficacy drastically decreases when DFA⁻ is paired with DiBAm⁺ and TriBAm⁺. Treatment with (DiBAm⁺)(DFA⁻) yielded at most 80% PLQY while treatment with (TriBAm⁺)(DFA⁻)

) produced an even lower PLQY (~70%). This observation of a large variation in PLQY from ~70% to ~100% observed in DFA⁻ set with various cation pairs strongly suggests that the charge trap passivation efficacy of ionic salts is significantly impacted by the pairing with cation. Our results show that, although DFA⁻ can be an effective passivating anion, it is not as competent as Br⁻, especially when paired with cations other than OLAm⁺. The difference in passivation efficacy of each anion is possibly explained by the variation in their interaction with their cation counterpart.

The third anion used in testing, BA⁻, has softer Lewis basicity than DFA⁻ and is expected to be superior for Pb²⁺ coordination according to the study by Nenon *et al.*⁵³ However, the study⁵³ showed that BA⁻ may not be as effective passivating ligand. In this study, we found that BA⁻ can effectively passivate charge traps depending on the choice of cations. The (OLAm⁺)(BA⁻) pair yielded superior passivation with ~90% PLQY while the (DiBAm⁺)(BA⁻) and (TriBAm⁺)(BA⁻) pairs showed relatively low PLQYs of 60% and 30%, respectively. Similar with the DFA⁻ set, the results from the BA⁻ set also shows ionic pairing dependent PLQY variations. Overall, the BA⁻ pairs were found to be not as effective for passivation compared to DFA⁻ pairs, which is consistent with the results in Nenon *et al.*⁵³ Though this may be explained by the large size of the benzoate anion causing steric hindrance, we propose that the interaction strengths of the cation – BA⁻ pairs may be larger than those of cation – DFA⁻ or Br⁻ pairs, hindering their ability to dissociate and ultimately passivate trap sites.

We note that the nBAm⁺ and TeBAm⁺ cations, regardless of anions they were paired with, behaved very differently from DiBAm⁺, TriBAm⁺, and OLAm⁺. Absorbance spectra of NCs treated with (nBAm⁺)(Br⁻) and (TeBAm⁺)(Br⁻) in Figure S1 (Electronic

Supplementary Information) feature a significant decrease in absorption intensity of the entire spectra, but especially the first excitonic peaks at 503 nm. These results suggest that all pairs with $n\text{BAm}^+$ and TeBAm^+ cations that we used cause degradation of NCs. Due to this complication, further studies with $n\text{BAm}^+$ and TeBAm^+ sets were not pursued.

2.4.3. NC size and PL lifetime measurement

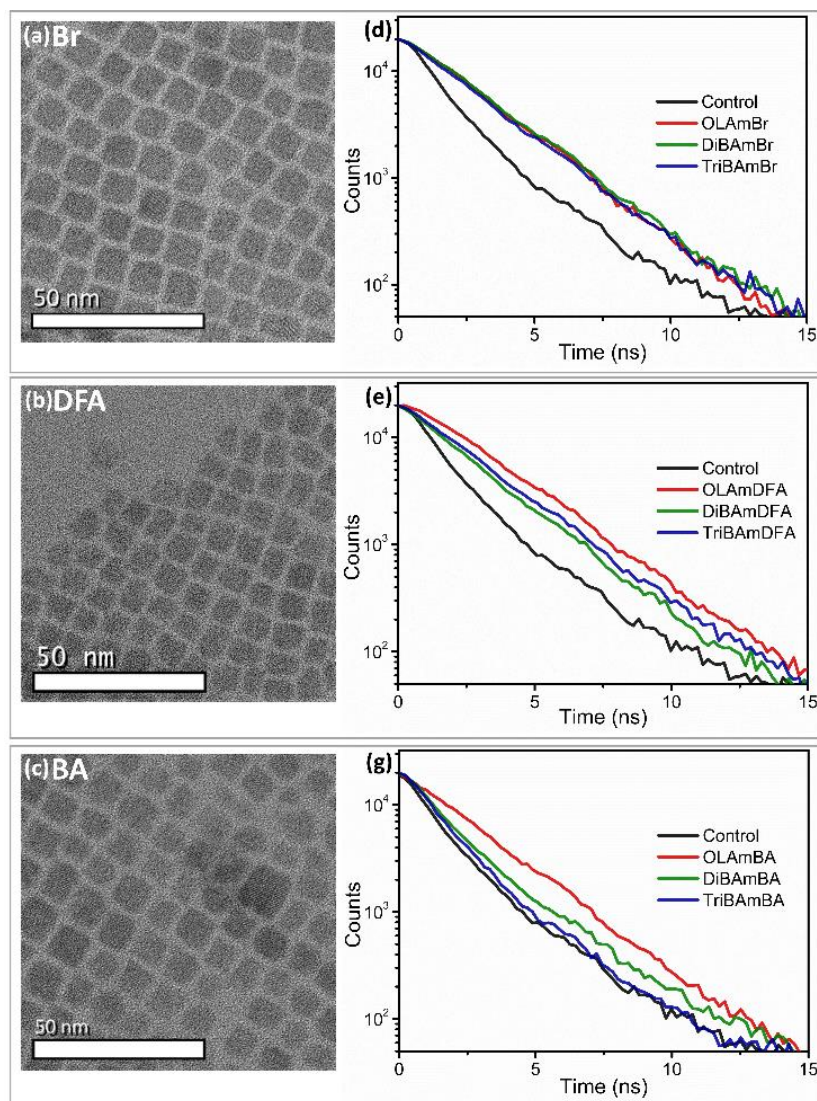


Figure 3. TEM images of NCs treated with the highest molar ratio of (a) OLAmBr, (b) OLAmDFA and (c) OLAmBA used for PLQY measurements. No significant structural change is observed. PL lifetime measurements of control (untreated) NCs versus NCs treated with various cations (OLAm⁺, DiBAm⁺, TriBAm⁺) paired with (d) Br⁻, (e) DFA⁻, and (f) BA⁻.

To check for a possibility that PLQY variation results shown in Figure 2 was caused by change in defect density through structural reconfiguration or deformation of NCs due to ligand treatment, we obtained TEM images of the NCs before and after the ligand treatments. For the measurements, the samples were prepared with the highest molar ratio of NCs and ligands that were used for PLQY measurements shown in Figure 2. OLAm⁺ was selected as the cation for the measurements due to the most drastic PLQY results with paired with the various anions. The average sizes of NCs determined from the TEM images displayed in Figure 3a-c are 7.8 ± 1.1 nm, 7.9 ± 1.2 nm, and 7.4 ± 1.2 nm for NCs treated with (OLAm⁺)(Br⁻), (OLAm⁺)(BA⁻), and (OLAm⁺)(DFA⁻) respectively. The average values of all samples fall within the statistical variation when compared to the as-synthesized NCs. Also, there were no significant changes to shapes of NCs. These results indicate that the ligand treatment-induced structural changes are statistically insignificant and not likely to be responsible for the observed differences in PLQY shown in Figure 2.

To better understand the origin of different PLQY values with various cation – anion pair treatment, we performed time-resolved photoluminescence (TRPL) measurements. A comparison of PL lifetimes allows us to gauge relative differences in a degree of non-radiative recombination that is primarily caused by charge trap states. Average lifetimes of NCs treated with cation – Br⁻ pairs, which yielded >95% PLQY (Figure 2c), are measured to be at least 2.5 times longer compared to those of untreated NCs (Figure 3d and Table

S1). The trend in PL lifetime is also successfully reflected in cation-dependent PLQY results in DFA⁻ and BA⁻ sets. In DFA⁻ set, (OLAm⁺)(DFA⁻) yielded the longest lifetime, followed by (TriBAm⁺)(DFA⁻) and then (DiBAm⁺)(DFA⁻). BA⁻ set showed the least increase of lifetime, as predicted in PLQY; highest lifetime from (OLAm⁺)(BA⁻), followed by (DiBAm⁺)(BA⁻) and (TriBAm⁺)(BA⁻). The PL lifetime values are provided in Table S1 in Electronic Supplementary Information. As a result, the PL lifetime results suggest that increase in PLQY upon ligand treatment is due to reduction in non-radiative recombination which largely depends on the combination of cation – anion pairs.

2.4.4. DFT calculations and analysis

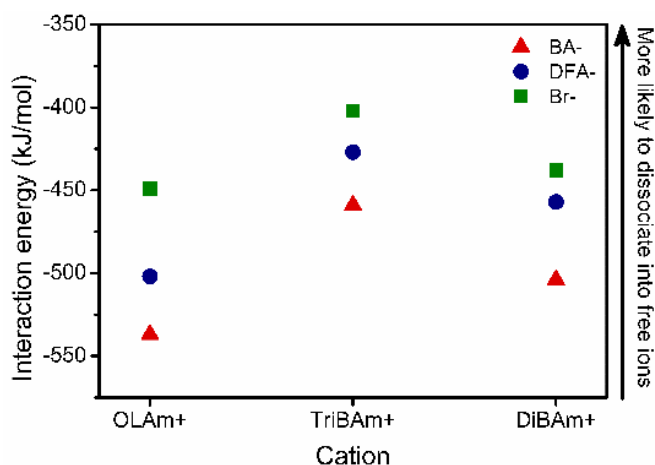


Figure 4. Interaction energies of various ionic pairs. Lower negative interaction energy is related to a higher tendency of the ionic pair dissociating into free ion species.

To test our hypothesis that interaction energies of ion pairs are a major factor in determining charge trap passivation efficacy, DFT calculations were performed. Initial ionic pair structures were found using ab initio molecular dynamics trajectories (details provided in Experimental section: Molecular Dynamics Simulations), and structures were

then subsequently optimized with the B3LYP/aug-cc-pvtz functional and basis set. Simulations were conducted in the absence of a solvent, full calculation details are provided in Experimental section: B3LYP Calculations and all DFT – optimized molecular structures are provided in *Ionic pairs molecular structure* file attachment. Additionally, images of the ion pair structures are provided in the Electronic Supplementary Information, Figure S2. The reaction between the cations and anions is not purely electrostatic for all complexes. Optimization of the DFA⁻ and BA⁻ ion pairs result in transfer of a proton from the cation to the anion (forming two approximately neutral molecules) for all pairs except (TriBAM⁺)(DFA⁻) where we found retention of the proton by TriBAM⁺ to be slightly (2 kJ/mol) more favorable (Figure S2). We do not observe proton transfer for the Br⁻ pairs. The interaction energy was calculated using the B3LYP/aug-cc-pvtz energies for ion pairs and individual ions and cations as:

$$\Delta E_{\text{inter.}} = E_{\text{AB}} - E_{\text{A}^+} - E_{\text{B}^-} \quad (1)$$

More exothermic interaction energy values indicate that the cation-anion pair is in a more stable and energetically favorable state. Conversely, the less exothermic the interaction energy is, the more likely the pair is to dissociate into the free ion species. Figure 4 reports the DFT results (values displayed in Table S2 in Electronic Supplementary Information); the trend in calculated interaction energies of ionic pairs is generally consistent with the PLQY results, as discussed below.

Among the ionic pairs, cation – BA⁻ pairs show the most exothermic interaction energies overall; they have the highest tendency to stay as an ionic pair and are expected to show the least effective trap passivation. Cation – DFA⁻ pairs have the second highest tendency to stay as a pair while the cation – Br⁻ pairs have the lowest. The calculation

results closely resemble our PLQY results, in which overall cation – BA⁻ pairs yielded lower PLQY ranging from 30 to 90%, followed by cation – DFA⁻ pairs from 70 to 100% and cation – Br⁻ from 95% to 100%. The interaction energy values among the set of ionic pairs with the same cation show a strong correlation with the trend observed in the PLQY results. For example, the interaction energy of (TriBAm⁺)(Br⁻) is the least exothermic (-400 kJ/mol) followed by (TriBAm⁺)(DFA⁻) with -430 kJ/mol and (TriBAm⁺)(BA⁻) with -460 kJ/mol while their respective PLQY (highest) values are 100%, 84%, and 36%. Similarly, the interaction energy values of (DiBAm⁺)(Br⁻) (-440 kJ/mol), (DiBAm⁺)(DFA⁻) (-460 kJ/mol), and (DiBAm⁺)(BA⁻) (-500 kJ/mol) are in a good agreement with the trend of their PLQY values (100%, 72% and 65%, respectively). OLAm⁺ – anion pairs also show similar results, with the exception of passivation by (OLAm⁺)(DFA⁻), which is as superior as (OLAm⁺)(Br⁻) despite its 50 kJ/mol more exothermic interaction energy. Additionally, our observation of all cation – Br⁻ pairs yielding superior passivation is consistent with their more endothermic interactions energies relative to cation – DFA⁻ and cation – BA⁻ pairs. With respect to the cation identity, no discernable trend between PLQY results and DFT results was observed amongst the cations studied in this study.

Our results suggest that interaction energy of an ionic pair may impose a considerable impact on the trap passivation efficacy. However, it is precarious to conclude that the interaction energy of an ionic pair is the only major factor governing the trap passivation efficacy. It is one of many factors that can contribute to the overall passivation mechanism such as the interaction of ions with MHP NC surfaces, the interaction with the native ligands, the entropic effects on the system, etc. In addition, we emphasize that the chemical properties of the anions, such as Lewis basicity,⁵³ is also very important as they

govern the direct interaction between the anions and the exposed Pb^{2+} atoms. Therefore, our DFT results can not entirely account for our experimental results, as evidenced in the absence of a trend between cations in comparison to the experimental data. However, a general correlation of our DFT results with the PLQY results is a strong indication that the interaction energy of cation-anion pair is a considerable factor in determining the passivation efficacy of the ionic pair.

Here it should be noted that our results may help explain the peculiar behavior of BA^- as an ineffective trap passivating anion that was previously observed in the literature.⁵³ The soft Lewis base BA^- was initially thought to be well-matched for coordination with soft Lewis acid Pb^{2+} . However, experimental results showed that using BA^- resulted in poor charge trap passivation. The authors speculated that the steric hindrance due to bulky benzene ring may be the cause.⁵³ Our results in this work suggest that another important factor that can explain this peculiarity is the lower tendency of cation- BA^- pairs to dissociate into ionic species compared to other cation-anion pairs.

Based on the findings from this work, ideal ionic pairs can be selected by carefully considering several factors. As supported by a previous study⁵³ and our results, the affinity of an anion to coordinate with exposed Pb^{2+} is an important factor to consider. The anion should be chosen to have soft Lewis basicity to match the soft Lewis acidity of the under-coordinated Pb^{2+} atoms on the surface, without any major steric hindrance. Additionally, as we have demonstrated in this work, it is beneficial to select an anion – cation pair with relatively low interaction energy. Therefore, the choice of cation should be carefully considered as it imposes a considerable influence on passivation mechanism as well.

Interaction energy between the cation and anion of an ionic salt can be exploited as a key factor for a facile and rapid screening platform for an optimal ligand selection. In the process of selecting a range of ionic salts for NC surface treatments, conducting numerous ligand treatment tests demands a large amount of time, cost and effort. However, an initial screening of ligand candidates by using the cation – anion interaction energy as a variable can significantly reduce the number of physical tests that need to be completed. It also substantially increases a range of ligands to be screened, which elevates the chance of finding a novel and effective ligand. This screening process is readily applicable for defect passivation of other perovskite-based NCs, and therefore bulk thin film compositions, as NCs have been shown to be an excellent model system for studying surface passivation treatments for bulk thin films.⁴⁸ For instance, it could be greatly beneficial for CsPbCl₃ and CsPbI₃ NC compositions, which have demonstrated low stabilities and challenges for PLQY improvement.²⁵ Low stability causes inevitable difficulties on experimental testing such as NC batch variability and a limited number of ligands for treatment. A wide range of computational screening of various ionic pairs may save time and cost caused by such complexities and help finding optimal ligands for effective surface defect passivation on MHP NCs.

2.5. Conclusion

In this work, we studied the impact of various cation – anion pairs on CsPbBr₃ surface trap passivation. Collective findings from PLQY, TEM and lifetime results show that a degree of trap passivation is not only determined by the compatibility of anion in ionic pair to passivate Br⁻ vacancies, but also the choice of cation that is paired with.

Although it is hard to elucidate how cation partakes in trap passivation mechanism, our work suggests that one of the governing factors to the passivation efficacy is the nature of ionic pairing, or particularly, interaction energy of cation – anion pair. The implication of this work for applications suggests that the interaction energy between cation – anion pairs needs to be taken into account when selecting ideal ligand for surface trap passivation on MHP NCs.

2.6. Reference

1. Y. Fu, H. Zhu, J. Chen, M. P. Hautzinger, X. Y. Zhu and S. Jin, *Nature Reviews Materials*, 2019, **4**, 169-188.
2. J. Sun, J. Wu, X. Tong, F. Lin, Y. Wang and Z. M. Wang, *Advanced Science*, 2018, **5**, 1700780.
3. S. Bai, Z. Yuan and F. Gao, *Journal of Materials Chemistry C*, 2016, **4**, 3898-3904.
4. Z. Song, S. C. Watthage, A. B. Phillips and M. J. Heben, *Journal of Photonics for Energy*, 2016, **6**, 022001.
5. H. Dong, C. Zhang, X. Liu, J. Yao and Y. S. Zhao, *Chemical Society Reviews*, 2020, **49**, 951-982.
6. Y. Dong, Y. Zou, J. Song, X. Song and H. Zeng, *Journal of Materials Chemistry C*, 2017, **5**, 11369-11394.
7. X. Di, L. Shen, J. Jiang, M. He, Y. Cheng, L. Zhou, X. Liang and W. Xiang, *Journal of Alloys and Compounds*, 2017, **729**, 526-532.
8. Y.-H. Kim, H. Cho and T.-W. Lee, *PNAS*, 2016, **113**, 11694-11702.
9. G. Li, F. W. R. Rivarola, N. J. L. K. Davis, S. Bai, T. C. Jellicoe, F. d. I. Peña, S. Hou, C. Ducati, F. Gao, R. H. Friend, N. C. Greenham and Z.-K. Tan, *Advanced Materials*, 2016, **28**, 3528-3534.
10. A. Perumal, S. Shendre, M. Li, Y. K. E. Tay, V. K. Sharma, S. Chen, Z. Wei, Q. Liu, Y. Gao, P. J. S. Buenconsejo, S. T. Tan, C. L. Gan, Q. Xiong, T. C. Sum and H. V. Demir, *Scientific Reports*, 2016, **6**, 1-10.
11. N. Wang, L. Cheng, R. Ge, S. Zhang, Y. Miao, W. Zou, C. Yi, Y. Sun, Y. Cao, R. Yang, Y. Wei, Q. Guo, Y. Ke, M. Yu, Y. Jin, Y. Liu, Q. Ding, D. Di, L. Yang, G. Xing, H. Tian, C. Jin, F. Gao, R. H. Friend, J. Wang and W. Huang, *Nature Photonics*, 2016, **10**, 699-704.
12. Z. Xiao, R. A. Kerner, L. Zhao, N. L. Tran, K. M. Lee, T.-W. Koh, G. D. Scholes and B. P. Rand, *Nature Photonics*, 2017, **11**, 108-115.
13. F. Yan, J. Xing, G. Xing, L. Quan, S. T. Tan, J. Zhao, R. Su, L. Zhang, S. Chen, Y. Zhao, A. Huan, E. H. Sargent, Q. Xiong and H. V. Demir, *Nano Lett.*, 2018, **18**, 3157-3164.
14. X. Zhang, H. Lin, H. Huang, C. Reckmeier, Y. Zhang, W. C. H. Choy and A. L. Rogach, *Nano Lett.*, 2016, **16**, 1415-1420.

15. X. Zhang, C. Sun, Y. Zhang, H. Wu, C. Ji, Y. Chuai, P. Wang, S. Wen, C. Zhang and W. W. Yu, *J. Phys. Chem. Lett.*, 2016, **7**, 4602-4610.
16. H. Guan, S. Zhao, H. Wang, D. Yan, M. Wang and Z. Zang, *Nano Energy*, 2020, **67**, 104279.
17. X. Li, Y. Wu, S. Zhang, B. Cai, Y. Gu, J. Song and H. Zeng, *Advanced Functional Materials*, 2016, **26**, 2435-2445.
18. Q. Mo, T. Shi, W. Cai, S. Zhao, D. Yan, J. Du and Z. Zang, *Photonics Research*, 2020, **8**, 1605.
19. S. Zhao, Y. Zhang and Z. Zang, *Chem Commun (Camb)*, 2020, **56**, 5811-5814.
20. R. E. Beal, D. J. Slotcavage, T. Leijtens, A. R. Bowring, R. A. Belisle, W. H. Nguyen, G. F. Burkhard, E. T. Hoke and M. D. McGehee, *J. Phys. Chem. Lett.*, 2016, **7**, 746-751.
21. M. Kulbak, S. Gupta, N. Kedem, I. Levine, T. Bendikov, G. Hodes and D. Cahen, *J. Phys. Chem. Lett.*, 2016, **7**, 167-172.
22. J.-F. Liao, H.-S. Rao, B.-X. Chen, D.-B. Kuang and C.-Y. Su, *J. Mater. Chem. A*, 2017, **5**, 2066-2072.
23. R. J. Sutton, G. E. Eperon, L. Miranda, E. S. Parrott, B. A. Kamino, J. B. Patel, M. T. Hörantner, M. B. Johnston, A. A. Haghighirad, D. T. Moore and H. J. Snaith, *Advanced Energy Materials*, 2016, **6**, 1502458.
24. Q. A. Akkerman, V. D’Innocenzo, S. Accornero, A. Scarpellini, A. Petrozza, M. Prato and L. Manna, *J. Am. Chem. Soc.*, 2015, **137**, 10276-10281.
25. G. Nedelcu, L. Protesescu, S. Yakunin, M. I. Bodnarchuk, M. J. Grotevent and M. V. Kovalenko, *Nano Lett.*, 2015, **15**, 5635-5640.
26. D. Parobek, Y. Dong, T. Qiao, D. Rossi and D. H. Son, *J. Am. Chem. Soc.*, 2017, **139**, 4358-4361.
27. Y. Tong, E. Bladt, M. F. Aygüler, A. Manzi, K. Z. Milowska, V. A. Hintermayr, P. Docampo, S. Bals, A. S. Urban, L. Polavarapu and J. Feldmann, *Angewandte Chemie International Edition*, 2016, **55**, 13887-13892.
28. D. Yan, S. Zhao, H. Wang and Z. Zang, *Photonics Research*, 2020, **8**, 1086.
29. F. Di Stasio, S. Christodoulou, N. Huo and G. Konstantatos, *Chemistry of Materials*, 2017, **29**, 7663-7667.

30. G. Li, J. Huang, H. Zhu, Y. Li, J.-X. Tang and Y. Jiang, *Chemistry of Materials*, 2018, **30**, 6099-6107.
31. J. De Roo, M. Ibanez, P. Geiregat, G. Nedelcu, W. Walravens, J. Maes, J. C. Martins, I. Van Driessche, M. V. Kovalenko and Z. Hens, *ACS Nano*, 2016, **10**, 2071-2081.
32. J. Song, T. Fang, J. Li, L. Xu, F. Zhang, B. Han, Q. Shan and H. Zeng, *Advanced Materials*, 2018, **30**, 1805409.
33. L. M. Herz, *Annual Review of Physical Chemistry*, 2016, **67**, 65-89.
34. M. B. Johnston and L. M. Herz, *Acc. Chem. Res.*, 2016, **49**, 146-154.
35. M. Stolterfoht, C. M. Wolff, J. A. Márquez, S. Zhang, C. J. Hages, D. Rothhardt, S. Albrecht, P. L. Burn, P. Meredith, T. Unold and D. Neher, *Nature Energy*, 2018, **3**, 847-854.
36. S. D. Stranks, *ACS Energy Lett.*, 2017, **2**, 1515-1525.
37. S. D. Stranks, V. M. Burlakov, T. Leijtens, J. M. Ball, A. Goriely and H. J. Snaith, *Phys. Rev. Applied*, 2014, **2**, 034007.
38. W. Tress, N. Marinova, O. Inganäs, M. K. Nazeeruddin, S. M. Zakeeruddin and M. Graetzel, *Advanced Energy Materials*, 2015, **5**, 1400812.
39. G.-J. A. H. Wetzelaer, M. Scheepers, A. M. Sempere, C. Momblona, J. Ávila and H. J. Bolink, *Advanced Materials*, 2015, **27**, 1837-1841.
40. Q. Chen, H. Zhou, T.-B. Song, S. Luo, Z. Hong, H.-S. Duan, L. Dou, Y. Liu and Y. Yang, *Nano Lett.*, 2014, **14**, 4158-4163.
41. B. A. Koscher, J. K. Swabeck, N. D. Bronstein and A. P. Alivisatos, *J. Am. Chem. Soc.*, 2017, **139**, 6566-6569.
42. N. K. Noel, A. Abate, S. D. Stranks, E. S. Parrott, V. M. Burlakov, A. Goriely and H. J. Snaith, *ACS Nano*, 2014, **8**, 9815-9821.
43. J. Pan, Y. Shang, J. Yin, M. De Bastiani, W. Peng, I. Dursun, L. Sinatra, A. M. El-Zohry, M. N. Hedhili, A.-H. Emwas, O. F. Mohammed, Z. Ning and O. M. Bakr, *J. Am. Chem. Soc.*, 2018, **140**, 562-565.
44. H. Wu, Y. Zhang, M. Lu, X. Zhang, C. Sun, T. Zhang, V. L. Colvin and W. W. Yu, *Nanoscale*, 2018, **10**, 4173-4178.
45. D. Yang, X. Li and H. Zeng, *Advanced Materials Interfaces*, 2018, **5**, 1701662.
46. H. Zhang, M. K. Nazeeruddin and W. C. H. Choy, *Advanced Materials*, 2019, **31**, 1805702.

47. X. Zheng, B. Chen, J. Dai, Y. Fang, Y. Bai, Y. Lin, H. Wei, X. C. Zeng and J. Huang, *Nature Energy*, 2017, **2**, 1-9.
48. M. R. Alpert, J. S. Niezgoda, A. Z. Chen, B. J. Foley, S. Cuthriell, L. U. Yoon and J. J. Choi, *Chemistry of Materials*, 2018, **30**, 4515-4526.
49. T. Chiba, Y. Hayashi, H. Ebe, K. Hoshi, J. Sato, S. Sato, Y.-J. Pu, S. Ohisa and J. Kido, *Nature Photonics*, 2018, **12**, 681-687.
50. Y. Wang, T. Zhang, M. Kan and Y. Zhao, *J. Am. Chem. Soc.*, 2018, **140**, 12345-12348.
51. T. Zhao, C.-C. Chueh, Q. Chen, A. Rajagopal and A. K. Y. Jen, *ACS Energy Lett.*, 2016, **1**, 757-763.
52. X. Zheng, B. Chen, J. Dai, Y. Fang, Y. Bai, Y. Lin, H. Wei, Xiao C. Zeng and J. Huang, *Nature Energy*, 2017, **2**, 17102.
53. D. P. Nenon, K. Pressler, J. Kang, B. A. Koscher, J. H. Olshansky, W. T. Osowiecki, M. A. Koc, L.-W. Wang and A. P. Alivisatos, *J. Am. Chem. Soc.*, 2018, **140**, 17760-17772.
54. J. Kang and L.-W. Wang, *J. Phys. Chem. Lett.*, 2017, **8**, 489-493.
55. H. Uratani and K. Yamashita, *J. Phys. Chem. Lett.*, 2017, **8**, 742-746.
56. J. P. Perdew and Y. Wang, *Phys Rev B Condens Matter*, 1992, **45**, 13244-13249.
57. G. Kresse, Furthmüller, J. , *Physical Review B*, 1996, **54**, 11169.
58. M. Frisch, G. Trucks, H. B. Schlegel, G. E. Scuseria, M. A. Robb, J. R. Cheeseman, G. Scalmani, V. Barone, B. Mennucci, G. Petersson and H. Nakatsuji, *gaussian 09, Revision d. 01*, Gaussian. Inc., Wallingford CT, 2009, **201**.
59. L. Goerigk, A. Hansen, C. Bauer, S. Ehrlich, A. Najibi and S. Grimme, *Physical Chemistry Chemical Physics*, 2017, **19**, 32184-32215.
60. S. Grimme, S. Ehrlich and L. Goerigk, *Journal of computational chemistry*, 2011, **32**, 1456-1465.
61. J.-D. Chai and M. Head-Gordon, *Physical Chemistry Chemical Physics*, 2008, **10**, 6615-6620.
62. M. J. Frisch, M. Head-Gordon and J. A. Pople, *Chemical Physics Letters*, 1990, **166**, 275-280.
63. J. Maes, L. Balcaen, E. Drijvers, Q. Zhao, J. De Roo, A. Vantomme, F. Vanhaecke, P. Geiregat and Z. Hens, *The journal of physical chemistry letters*, 2018, **9**, 3093-3097.

2.7. Supplementary Information

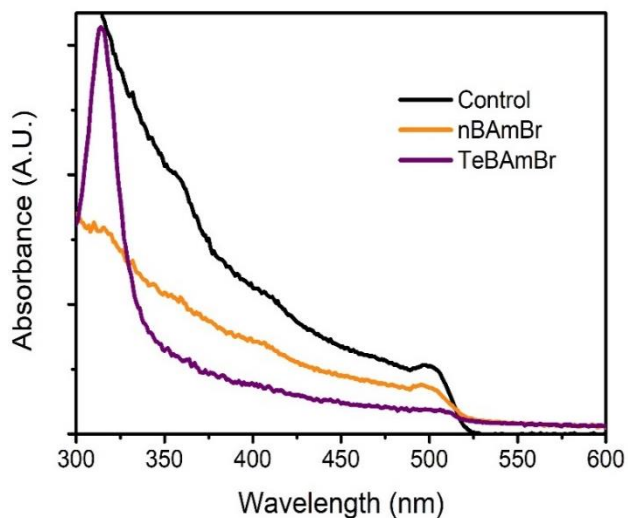


Figure S1. Absorbance spectra of NCs treated with 50 μM of $(\text{nBAm}^+)(\text{Br}^-)$ and $(\text{TeBAm}^+)(\text{Br}^-)$. A decrease in first excitonic peak indicates a general decrease in NC population upon ligand treatment.

Table S1. Averaged PL lifetime values (ns) of control versus various cation – anion pairs.

PL lifetime (ns) Untreated NCs = 1.1	Br^-	DFA^-	BA^-
OLAm^+	2.7	2.9	2.5
TriBAm^+	2.5	2.1	1.2
DiBAm^+	2.7	2.0	1.4

Table S2. Interaction energies of various cation – anion pairs in kJ/mol, computed with B3LYP/aug-cc-pvtz

Interaction energy (kJ/mol)	Br^-	DFA^-	BA^-
OLAm^+	-449	-502	-537

TriBAm ⁺	-402	-427	-459
DiBAm ⁺	-438	-457	-504

Table S3. Interaction energies of various cation – anion pairs in kJ/mol, computed with B3LYP/ aug-cc-pvtz with D3(BJ) dispersion corrections.

Interaction energy (kJ/mol)	Br ⁻	DFA ⁻	BA ⁻
OLAm ⁺	-459	-507	-548
TriBAm ⁺	-426	-454	-482
DiBAm ⁺	-449	-470	-517

Table S4. Interaction energies of various cation – anion pairs in kJ/mol, computed with ω B97X-D/ aug-cc-pvtz.

Interaction energy (kJ/mol)	Br ⁻	DFA ⁻	BA ⁻
OLAm ⁺	-453	-511	-547
TriBAm ⁺	-423	-457	-485
DiBAm ⁺	-444	-474	-518

Table S5. Interaction energies of various cation – anion pairs in kJ/mol, computed with MP2/ aug-cc-pvtz.

Interaction energy (kJ/mol)	Br ⁻	DFA ⁻	BA ⁻
OLAm ⁺	NC ¹	NC	NC
TriBAm ⁺	-456	-467	NC
DiBAm ⁺	-470	-479	-522

¹ Not Calculated (NC) due to memory cost.

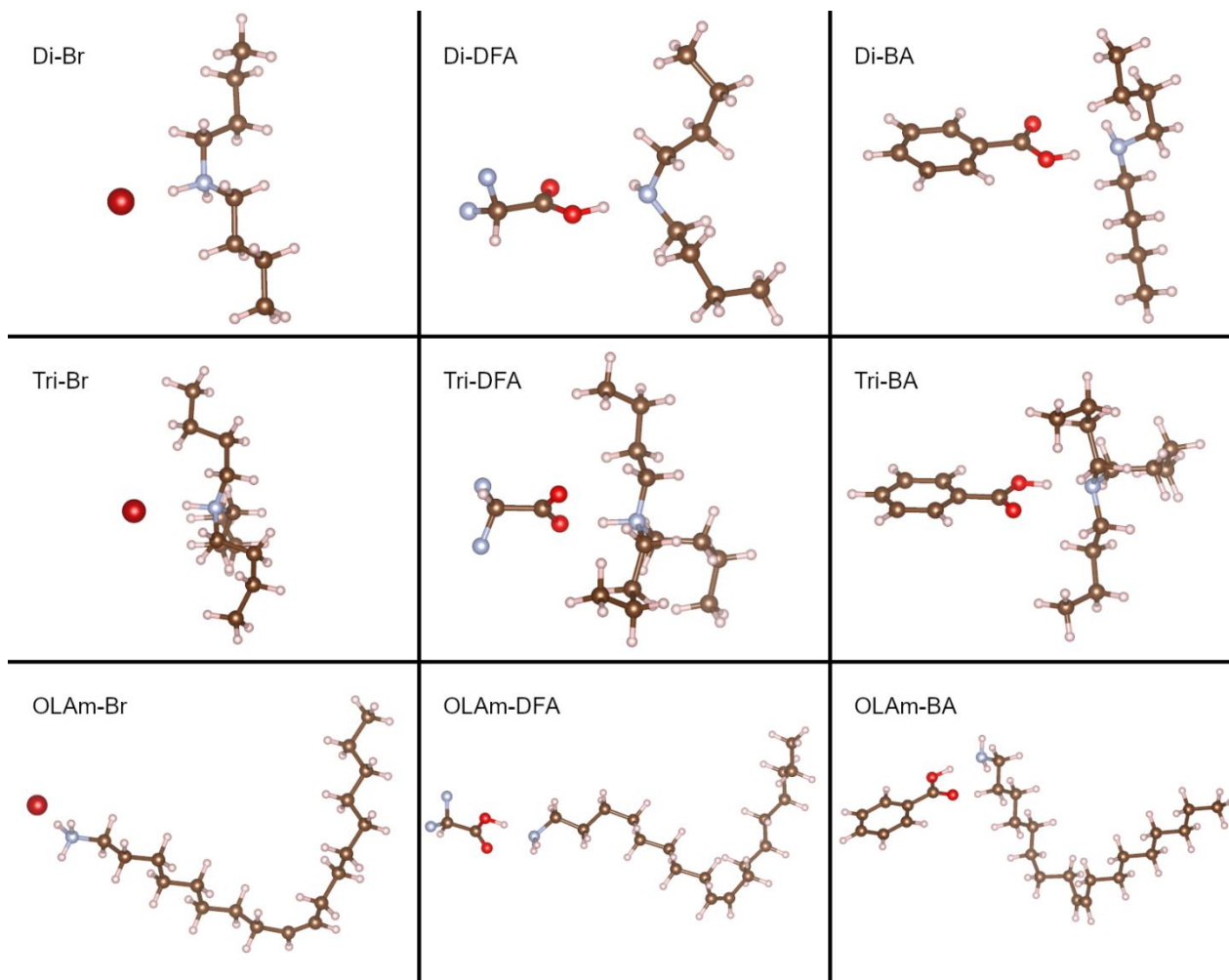


Figure S2. Molecular structures for the B3LYP/aug-cc-pvtz optimized cation – anion pairs. Colors are: C (brown), H (white), O (red), N (light blue), Br (maroon).

Chapter 3: A new metric to control nucleation and grain size distribution in hybrid organic-inorganic perovskites by tuning the dielectric constant of the antisolvent

This chapter was adopted from a published work: *Journal of Materials Chemistry A* **2021**, 9(6), 3668-3676.

3.1. Abstract

In perovskite research, there is a widely exploited but poorly explained phenomenon in which the addition of “antisolvents (ATS)” to precursor solutions results in higher-quality films. We explain the mechanism and driving force underlying an antisolvent-driven solvent extraction process. Density functional theory calculations uncover the defining effects of antisolvent choice on the extent of complexation between a lead salt and a methylammonium cation in solution. We experimentally validate the computational results using ultraviolet-visible spectroscopy and ^{207}Pb nuclear magnetic spectroscopy of methylammonium lead iodide solutions, containing both a processing solvent and an antisolvent. Furthermore, we uncover, and subsequently identify, the appearance of new species in solution as a result of the addition of the antisolvent. We observe that the choice of antisolvent has a substantial effect on the nature of the complexation of the methylammonium lead iodide (MAPbI_3) precursor species, whose origin we explain at an atomic level; specifically, the lower the dielectric of the antisolvent, the stronger the intermolecular binding energy between methylammonium cation (MA^+) cation and PbI_3^- plumbate, independent of the solvent or antisolvent interaction with the lead salt. Thin films were characterized using scanning electron microscopy; images of the films show how the addition of an antisolvent

influences and, importantly, can be used to alter thin-film grain size. Grain size and distribution in thin films is reflected by the choice of antisolvent, promoting slower nucleation rates, a lower nucleation density, and hence larger final grain size.

1.1. Introduction

Hybrid organic-inorganic perovskites (HOIPs) have shown significant and growing effectiveness as prospective solar cell materials since their emergence in 2009¹. With their current certified solar cell efficiency of over 25.0%,² HOIPs are now a competitive solar cell material with mature techniques established for thin film fabrication^{3,4}. Multiple studies have emphasized the importance of understanding how HOIP film formation is governed by solution processing to achieve uniform film morphology, large grain size and high crystallinity^{5,6}. All of these desirable characteristics are directly correlated to processing choices in the search for improved device performance.⁷⁻¹⁵ Unfortunately, the focus on increasing power conversion efficiency (PCE) has outstripped our understanding, and hence control, of the fundamentals of solution chemistry that gives rise to the nucleation and growth of HOIP crystallization pathways and hence film quality. Solvent “engineering” for perovskites was first proposed in 2014 to expedite nucleation and achieve smooth, full-coverage perovskite films by the addition of antisolvents during spincoating¹⁶.

This has been one of the most important contributions to the field, as it has proven to achieve uniform coverage, pinhole-free surface morphology and better device performance while inducing fast nucleation¹⁶⁻¹⁹. Zhou *et al.* later demonstrated an alternative method incorporating antisolvents using an “antisolvent bath method,”^{20,21} in which the perovskite thin film is immersed in a bath of antisolvent. This eliminated the difficulties of precise timing and uniform deposition needed for antisolvent treatment during spin-casting and it reduced film damage. Currently, the

criteria used to constitute an antisolvent in the context of perovskite solar cells is that the antisolvent is miscible with the processing solvent used to dissolve HOIP precursor species such as the lead salts and methylammonium iodide (MAI), and that it does not dissolve the perovskite or perovskite species.⁵ The wide range of antisolvents used to date for perovskite films has produced variable results for film quality, dependent on the chemistry of the antisolvent.^{16,22–24} Xiao *et al.*¹⁸ studied the effect of different antisolvents on methylammonium lead iodide (MAPbI₃) thin films deposited from dimethylformamide (DMF) to show that films exposed to acetonitrile, benzonitrile and tetrahydrofuran produced transparent films, for reasons that are still not fully understood. Alcohol-containing antisolvents such as methanol, ethanol, and ethylene glycol produced a large amount of PbI₂ in the resulting thin film due to the high solubility of the perovskite in these solvents. Toluene, chlorobenzene and xylene, however, produced good coverage and large grain sizes²⁵. To date, the induced nucleation observed as a result of antisolvent addition is thought to occur through a solvent extraction process, induced by the antisolvent.^{20,21} But the mechanism by which this occurs is still largely undefined. Further, no thorough study has been conducted on the interactions between the processing solvent and antisolvents, nor the interaction of antisolvents with HOIP precursor species. To shed light on this, we have conducted an in-depth examination on the effect of using four commonly used antisolvents, dichloromethane (DCM), chlorobenzene (CB), anisole (ANS) and toluene (TOL), on an archetypal perovskite precursor solution containing MAPbI₃ in DMF.

The focus of this work is to uncover the mechanism and driving force underlying antisolvent-solvent extraction and explain how antisolvents promote fast HOIP nucleation. To do so, we employ a combination of computational and experimental approaches. Computationally, we use density functional theory (DFT) to probe interactions at an atomic-level. We include

experimental validation of these calculations using Ultraviolet Visible spectroscopy (UV-Vis), and ^{207}Pb Nuclear Magnetic Spectroscopy (^{207}Pb -NMR) of the perovskite precursor solutions containing DMF and antisolvents. We use scanning electron microscopy (SEM) to characterize thin films deposited from different solution choices.

3.3. Methods

3.3.1. DFT computational details

Solvent molecules and perovskite precursor species were built using the molecule visualization tool, Avogadro²⁶. Their geometries were optimized using the quantum mechanical software package, Orca,²⁷ which we have employed extensively in the past to study perovskite moieties.^{9,28,29} DFT calculations of the molecular geometries were converged using a pure generalized gradient approximation (GGA) B9730,³¹ and a polarized basis set, TZVPP32 with dispersion corrections, as recommended by Grimme.^{31,33} All the molecular species and complexes were further optimized using PW6B95, the well-ranked hybrid functional in Grimme *et al.*'s thorough benchmark.³⁴ The Geometrical Counterpoise Correction (gCP)³⁵ was added to remove artificial over-binding effects from basis set superposition errors (BSSE). All systems were given “Tight SCF” and slow convergence criteria with a grid size of 7. The processing solvent chosen for this study was DMF as it is one of the most widely employed solvents for HOIPs and has been shown to produce films with superior morphology compared to other processing solvents.^{16,36} The antisolvents included in this study are DCM, CB, ANS, and TOL (acronyms described in section

1). For each set of simulations, we used a single explicit solvent molecule in conjunction with the COSMO implicit solvation model^{37,38} to incorporate the dielectric of the solvent, or solvent mixture, into the simulations.

3.3.2. Absorbance characterization

To examine the effect of MAI concentration in MAPbI₃ precursor solution, we prepared a solution of 2.5 mM lead iodide (PbI₂) (TCI, 99.999%) and varying concentrations (2.5 mM - 0.75 M) of methylammonium iodide (MAI) (Dyesol, 99.99%) dissolved in DMF (Sigma-Aldrich, 99.8%). To study the effect of the dielectric constant of the antisolvent in a MAPbI₃ precursor solution, we maintained constant concentrations of PbI₂ and MAI as we varied the molar ratio of DMF to the antisolvent (DCM, CB, ANS, and TOL) from 3:1, to 2:1, to 1:1. The solutions were stirred until the precursors were completely dissolved and the solution became clear. The solutions were kept in a N₂-purged glovebox and transferred into airtight capped cuvettes until immediately before the absorbance measurement in order to minimize ambient exposure. Absorbance measurements were taken using a PerkinElmer Lambda 950S spectrophotometer. The corresponding DMF or DMF-antisolvent solvent mixture was used as a blank reference for calibration. It should be noted that absorbance spectra of excess MAI with PbI₂ concentrations above 2.5 mM could not be measured due to the saturation of measured signal.

3.3.3. ²⁰⁷Pb-NMR characterization

We performed ²⁰⁷Pb-NMR spectroscopic measurements of DMF and DMF-antisolvent solution samples using a Varian NMRS 600 at a frequency of 125.7 MHz. The delay time, acquisition time, and pulse were set at values of 10 ms, 42.6 ms, and 3.125 μs, respectively. The chemical shifts were referenced to Pb(NO₃)₂ in D₂O. We prepared the samples using an identical

procedure described in the Experimental Absorbance Characterization section. Solutions were stored and transferred into airtight NMR tubes in the N₂ glovebox prior to measurement.

3.3.4. Thin film fabrication

We prepared a precursor solution of 1M MAPbI₃ in DMF and stirred overnight in a N₂ glovebox to ensure a complete precursor dissolution. For film fabrication, we cleaned glass substrates by sonicating in a Hellmanex soap solution and then in deionized H₂O for 10 min. The substrates were further sonicated in iso-propanol and acetone for 10 min each. The cleaned substrates were UV-ozone treated for 10 min and brought into the N₂ glovebox for spin-coating and an annealing process. On the substrate, we statically dispensed 45 μ L of precursor solution, immediately initiated spin-coating at 4000 rpm. Six seconds after the start of the spin-coating process, we rapidly dispensed 200 μ L of antisolvent onto the substrate. After the spin-coating was finished, we annealed the thin film at 110 °C for 10 min. The samples were stored in a glovebox prior to SEM characterization. We performed planar SEM imaging with a FEI Quanta 650 SEM operating at a 2 kV accelerating voltage to examine the morphologies and grain sizes of films prepared via extraction with different antisolvents.

3.4. Results and Discussion

3.4.1. Solvent-antisolvent interactions

DFT calculations provided information on the pre-nucleation moieties and the interactions of the precursor species, solvent and antisolvents studied in this work. To understand the molecular-scale interactions that occur between DMF and the different antisolvents, we calculated the intermolecular binding energy between solvent molecules for both the solvent interacting with

itself, *e.g.*, two DMF molecules, which we refer to as “same-solvent” pairs and for mixtures of DMF with antisolvent molecules *e.g.*, one DMF and one DCM molecule, denoted as “DMF-ATS” in Figure 1 (see Figure S1 in the Electronic Supplementary Information for values of solvent-solvent intermolecular binding energies). Sorenson *et al.*²⁹ previously showed that a small system containing as few as one to three explicitly modeled solvent molecules can provide accurate trends in intermolecular binding energies for perovskite precursor species in solution. For the mixed DMF-antisolvent simulations, we calculated the static dielectric of each DMF-antisolvent solution using a 2:1 ratio of DMF:antisolvent for each antisolvent in this study. The dielectric constants of pure DMF, DCM, CB, ANS and TOL are 36.7, 8.98, 5.62, 4.33, 2.38, respectively³⁹. Using the dielectric mixing rules based on the Kirkwood model,^{40,41} and a 2:1 ratio of DMF to antisolvent, this resulted in dielectric values of the precursor solutions being 28.54, 24.38, 23.73, and 22.66 for DMF:DCM, DMF:CB, DMF:ANS and DMF:TOL, respectively.

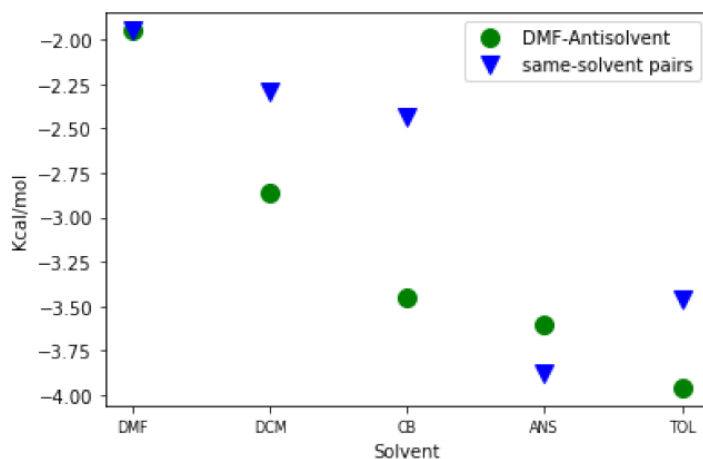


Figure 1. Intermolecular binding energies (in kcal/mol) of 2:1 binary solvent mixtures used in perovskite precursor solution processing and arranged in decreasing value of the mixture's dielectric constant: The binding energy of DMF to an antisolvent is shown as green circles. The binding energy of "same-solvent" pairs is shown as blue triangles.

More negative values of the intermolecular binding energy correspond to stronger interactions between each species or solvents. Figure 1 shows that DMF has a stronger affinity for all the antisolvents we tested than it does with itself. We observe that DMF has the largest attraction to TOL, followed -in order- by ANS, CB and DCM. Antisolvents containing aromatic groups (TOL, ANS and CB) show increased affinity to DMF (ranging between -3.45 and - 3.96 kcal/mol) compared to DCM (-2.86 kcal/mol), which has no aromatic groups, and the intermolecular binding energy between two DMF molecules (-1.95 kcal/mol). Since aromatic rings involve regions of both positive and negative charge on either side of the conjugated ring, the polar oxygen atom on DMF, with its lone pair of electrons, would be more attracted to this region of positive charge. The two electronegative chlorine atoms on the small dichloromethane molecule exhibit more repulsion when mixed with DMF than the other antisolvents in this study. Given the results in Figure 1, the addition of an antisolvent to the DMF precursor solution will clearly promote strong DMF-antisolvent interactions.

3.4.2. Antisolvent-HOIP precursor interactions

To understand the nature of the solvent-antisolvent extraction mechanism, we first probed molecular-scale interactions between an MAPbI_3 precursor species, DMF and each of the antisolvents; then we probed the interaction of the MA^+ cation to the DMF or antisolvent-coordinated PbI_3^- plumbate. The resulting intermolecular binding energies are reported in Figure

2 (see Figure S2 in Electronic Supplementary Information for calculated intermolecular binding energy values). The strength of these interactions provides information about the effects of antisolvent on the complexation between the PbI_3^- and the MA^+ cation, and how each solvent complexes with an MAPbI_3 precursor species. The MAPbI_3 species was chosen based on the idea by Sorenson *et al.*²⁹ that this was the smallest and most energetically favorable perovskite “building block” that contained both the methylammonium cation and an iodoplumbate.

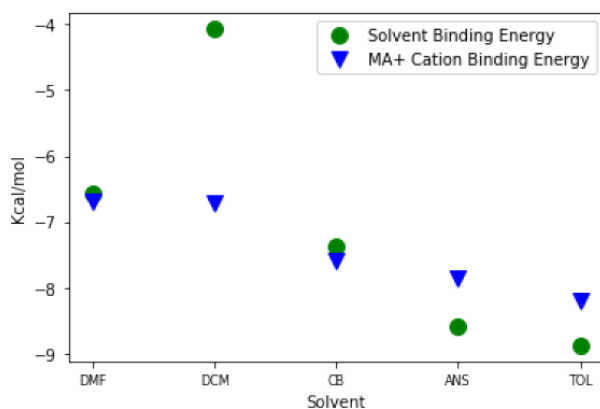


Figure 2. Intermolecular binding energies of DMF and antisolvents to MAPbI_3 species (green circles). The binding energies of a MA^+ cation to a complex formed between PbI_3^- and a single molecule of either DMF or antisolvent (blue triangles). All binding energies are given in kcal/mol.

Most antisolvents, with the exception of DCM, have a considerably stronger attraction to the MAPbI_3 precursor species than the processing solvent DMF. Figure 2 shows the strength of the antisolvents to the MAPbI_3 precursor species denoted by green circles. It shows that CB (-7.38 kcal/mol), ANS (-8.59 kcal/mol) and TOL (-8.88 kcal/mol) each have a stronger affinity for the MAPbI_3 precursor species by 0.8 to 2.3 kcal/mol compared to DMF (-6.66 kcal/mol). The strength of the intermolecular binding energy between the antisolvent and an MAPbI_3 precursor species increases with decreasing dielectric constant of the solution. We postulate that antisolvent-solvent

extraction mechanism is partially driven by the stronger attraction of the antisolvent to the plumbate, thereby displacing DMF solvent molecules that surround the precursor species. Stevenson *et al.* showed that solvents commonly used in perovskite thin film processing, such as DMF, form dative bonds with the Pb atom in the PbX_n plumbate²⁸. We adopt that study's use of the Mayer Bond Order (MBO), a quantum mechanical measure of the electron density between atoms, to measure the interaction and coordination between antisolvents and the MAPbI_3 precursor species. We found that DMF is the only solvent in this study that possessed a detectable MBO between the solvent and MAPbI_3 , specifically between the oxygen atom, and the lead atom (MBO of 0.176), indicating electron donation from DMF to the lead, characteristic of a dative bond. All the antisolvents we studied revealed no detectable MBO between any atom in the MAPbI_3 species, to any atom in the antisolvent molecules, indicating a lack of dative bond formation.

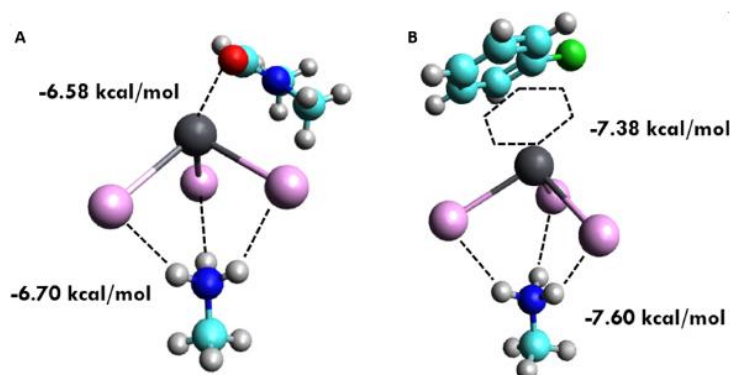


Figure 3. Visualization of the intermolecular binding of (A) DMF solvent coordinated through a dative bond with MAPbI_3 species and (B) the chlorobenzene antisolvent showing a π -cation interaction between the conjugated ring and the Pb atom in the MAPbI_3 species. (Color code: Oxygen (red) Hydrogen (white) Nitrogen (blue), Carbon (cyan), Lead (grey), Iodine (pink))

Looking at the interaction of the antisolvents with the MAPbI₃ precursor species, we found that TOL, ANS and CB all interact with the lead atom in MAPbI₃ through non-covalent p interactions, and not the electronegative chlorine or oxygen atom on CB or ANS, respectively (as illustrated in Figure 3). The lack of detection of an MBO between pairs of atoms here indicates that the region of charge that the antisolvent shares with the lead atom extends over most, if not all, of the carbon atoms in the conjugated ring, and not an isolated atom in the antisolvent molecule. Individually, each carbon atom does not donate enough electron density to form a measurable MBO value. The concept of the antisolvent-solvent extraction mechanism, as we show, is largely driven by, first, the affinity of DMF to the antisolvents that we have calculated above and, secondly, by the antisolvent having stronger, non-covalent interaction with the lead atom, facilitating the exchange of a processing solvent molecule for an antisolvent⁵. The correlation we observed between decreasing solution dielectric and increasing intermolecular binding energy, also extends to the strength of MA⁺ cation complexation to the iodoplumbate to form MAPbI₃ precursor species, as seen in Figure 2. As a result, this increase in the strength of complexation between MA⁺ cations and plumbates in solution is a direct view into the earliest stages of nucleation.

$$\Delta G(r) = \left[\frac{-4\pi r^3}{3V_m} \right] R T \ln(S) + 4\pi r^2 \gamma_{CL} \quad (1)$$

Equation (1)⁴² shows how the total free energy change, ΔG , is a function of the saturation ratio $S = C/C_s$, where C is the concentration of the solute in the perovskite precursor solution, and C_s is the equilibrium solubility limit (r is the nuclei radius, V_m is the molar volume of the nucleus, R is the gas constant, T is temperature, γ_{CL} is the interfacial energy between the solvent and the nucleus). Supersaturation is a driving force of nucleation and growth and will ultimately dictate the final crystal size distribution. As we have shown, antisolvents lower the overall dielectric constant of the perovskite solution and promote complexation between the MA⁺ cation and PbI₃⁻

plumbate, leading to an increase in the formation of new MAPbI_3 precursor species, and thus reducing the amount of MA cations and lead salts in solution. Unlike DMF, or other processing solvents, the antisolvent's inability to dissolve lead salts and perovskites⁴³ implies that it also cannot dissolve the smallest perovskite building block, e.g., MAPbI_3 , or clusters of these building blocks. Supersaturation is achieved by increasing the saturation ratio, S in Equation 1, by simultaneously reducing C_s , the solubility limit of MA^+ cation and lead salts, and increasing C , the concentration of newly generated insoluble (MAPbI_3) species. In general, the supersaturation intervals are decreased with increasing dielectric constant of the solvent or the solution and is evident when you consider that the dielectric constant is a measure of the solvents polarity⁴⁴. In our work here, the addition of each tested antisolvent to different samples of the precursor solution reduces the dielectric constant of the system. All our systems contained the processing solvent DMF, giving rise to dielectric constants of 28.54, 24.38, 23.73, and 22.66 for DMF:DCM, DMF:CB, DMF:ANS and DMF:TOL, respectively. It is therefore palpable that the lower the dielectric of the antisolvent, the smaller the supersaturation interval will be, and therefore the smaller the grain size in the resulting thin films.

3.4.3. UV-Vis absorbance results analysis

Previous studies have assigned the absorbance peaks responsible for iodoplumbate species: PbI_2 at 330 nm, PbI_3^- at 370 nm, and PbI_4^{2-} at 422 nm.⁴⁵ In good agreement with the reported literature,⁴⁶ we observed that the addition of excess MAI in increasing concentrations promotes the formation of higher ordered iodoplumbate species, represented by absorbance increases in the 370 and 422 nm peaks (Figure 4A). The presence of an isosbestic point at 388 nm indicates that species transition from PbI_3^- to PbI_4^{2-} states upon the addition of excess MAI. To probe the role of

the antisolvent in an environment where the concentrations of PbI_2 and MAI are relatively low and at similar degree, we prepared solutions of equimolar 2.5 mM PbI_2 and MAI in DMF (control) and in 1:1 molar ratios of DMF to various antisolvents. As shown in Figure 4B, we observed that the addition of antisolvent shows an increase in higher iodoplumbate species formation in low precursor concentration environment. We also discovered that the extent of PbI_3^- formation is inversely correlated with the dielectric constant trend of an antisolvent incorporated in the solution. Specifically, samples that contain a lower dielectric constant antisolvent yielded a higher degree of PbI_3^- formation. This suggests that, in a low concentration of PbI_2 and MAI precursor solution, addition of a lower dielectric constant antisolvent shows an analogous effect to that of the addition of excess MAI.

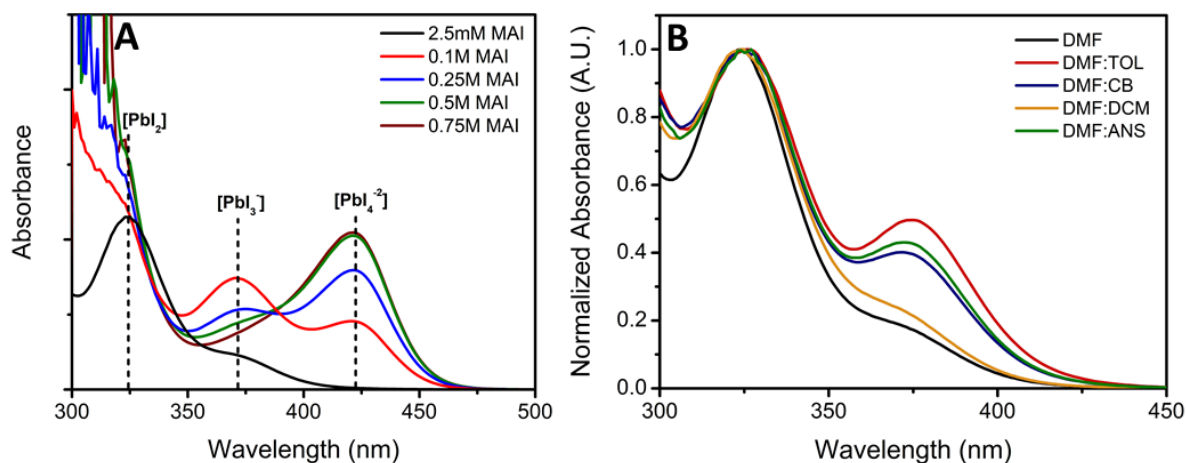


Figure 4. Absorbance spectra of (A) 2.5 mM PbI_2 solution with varying concentrations of MAI (2.5 mM, 0.1 M, 0.25 M, 0.5 M, and 0.75 M). As the MAI concentration increases, higher-ordered iodoplumbates are observed, indicated by an increase in the absorbance peak at 422 nm. (B) Equimolar 2.5mM PbI_2 and MAI solutions dissolved in pure DMF and in 1:1 molar ratios of DMF and various antisolvents.

To investigate the effect of adding antisolvents with different dielectric constants into perovskite precursor environments in which higher-order iodoplumbates species are dominant, we performed UV-Vis absorbance measurements on 1:1 molar ratios of DMF to various antisolvents that incorporated 2.5 mM PbI_2 and 0.75 M MAI solutions (using a procedure provided in the Methods section). As shown in Figure 5, the absorbance spectrum of a perovskite precursor in pure DMF (control) yielded a predominant peak at around 422 nm. As these various antisolvents were introduced into the precursor solutions, the absorbance peaks at 422 nm broadened significantly, and showed an increasing blueshift towards lower wavelengths (Figure 5). The extent of blueshift also depended on the molar ratio of DMF to antisolvent incorporated in each solution. As we decreased the molar ratio of DMF to antisolvent from 3:1 to 1:1, we clearly observed a more pronounced and distinctive peak formation between 422 nm and 372 nm (see Figure 5 A-C). With the exception of DCM, the increment in the blue-shift in absorbance showed a strong correlation with the dielectric constant of the choice of antisolvents incorporated into the solution. For instance, the addition of TOL, which has the lowest dielectric constant, resulted in the largest blue-shift of the 422 nm absorption peak. A similar trend was followed by ANS and CB.

The blue-shifted peak does not correspond to the positions of either the PbI_3^- or PbI_4^{2-} peaks, suggesting the appearance of another, as yet unidentified, precursor species that have a characteristic absorption between 372 nm and 422 nm. Deconvolution of the absorbance peak into two peaks shows that the contribution is composed mostly from peaks at 393 nm (the new peak that we postulate to be a species of the form MA_xPbI_4 in the presence of an antisolvent) and at 422 nm (the PbI_4^{2-} peak). To more clearly compare the degree of formation of the new precursor species responsible for the absorption at 393 nm, the ratio of the areas under the 393 nm and 422 nm peaks in 1:1 molar ratio was plotted with respect to the dielectric constant of the precursor solution. The

DCM plot was not included, as the 393 nm peak could not be fitted. The resulting data (shown in Figure 5D) shows a general trend in which more of the new species (postulated to be MA_xPbI_4) forms as a result of incorporating an antisolvent with increasingly lower dielectric constant into the precursor solution.

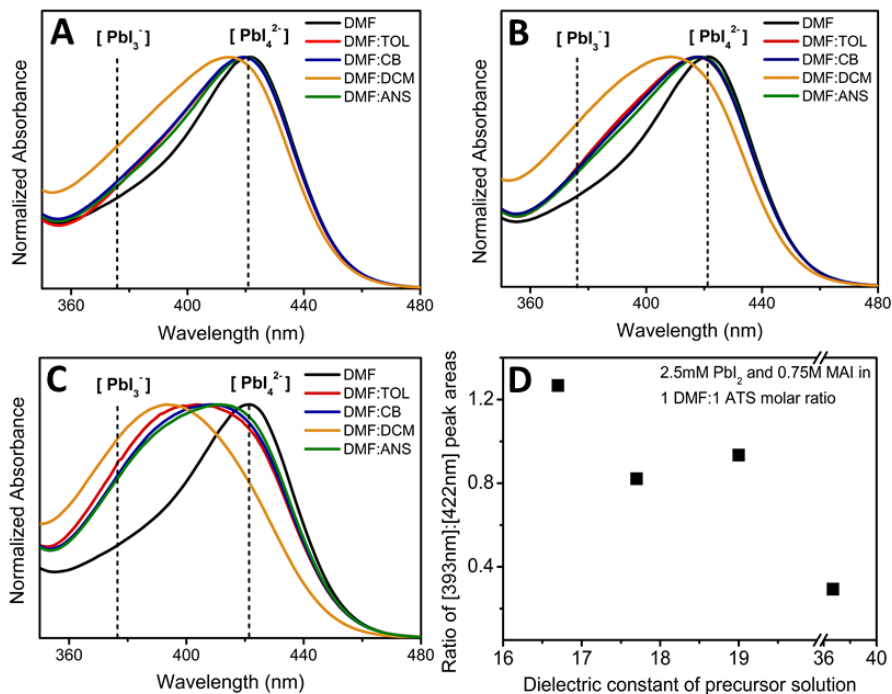


Figure 5. Normalized absorbance spectra of 2.5 mM PbI_2 and 0.75 M MAI dissolved in pure DMF and with a (A) 3:1 (B) 2:1 and (C) 1:1 molar ratio of DMF to a set of antisolvents with varying dielectric constant, as listed in the inset color key. The new absorbance peak positions of PbI_3^- (372 nm) and PbI_4^{2-} (422 nm) are marked with dotted vertical lines. (D) The ratio between the areas under the new peak, appearing at 393 nm, and at 422 nm plotted as a function of dielectric constant of precursor solution. The trend shows a higher ratio of 393 nm and 422 nm peaks for lower dielectric constant precursor solutions.

The absorption of energy observed in UV-Vis spectra has its origin in the excitation of electrons from their ground state to a higher-energy (excited) molecular orbital. This links the absorption peaks in the UV-Vis spectrum to the difference in energy between the Highest Occupied Molecular Orbital (HOMO) and the LUMO (Lowest Unoccupied Molecular Orbital). To test this connection and help identify the precursor species giving rise to the new absorption peak, we performed DFT calculations to obtain the HOMO-LUMO gap energies. The species studied here were built in a so-called “Jacob’s ladder” approach, starting with calculation of Δ HOMO-LUMO gaps for different lead salts (PbI_2 , PbI_3^- , or PbI_4^{2-}). This allowed us to identify precursor species as candidates based on their Δ HOMO-LUMO energy gap, looking for candidates that lie between the Δ HOMO-LUMO energy gaps for PbI_3^- and PbI_4^{2-} , and reported in Figure 6. The HOMO-LUMO gaps were calculated for each precursor species in DMF as well as DFT calculations of the value of the Δ HOMO-LUMO gap are typically an underestimate by about a factor of two; the quality of this approximation to the true energy difference depends sensitively on the nature of the exchange–correlation functional chosen and the amount of Hartree–Fock exchange that is incorporated.⁴⁷ However, for our purposes, we only need to observe trends in the DFT-generated gaps.^{48,49}

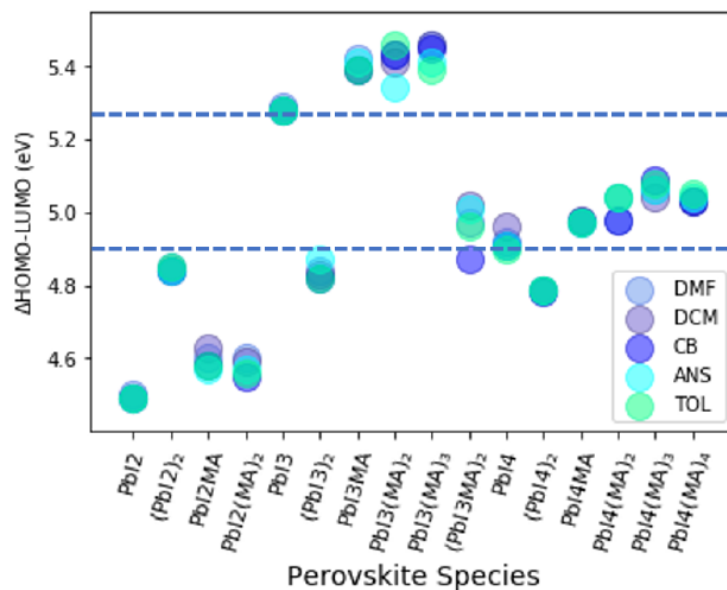


Figure 6. Differences in HOMO-LUMO energy levels (eV) in different DMF/antisolvent solutions for perovskite precursor species. Horizontal dashed lines indicate the characteristic Δ HOMO-LUMO energy gap for PbI_3^- and PbI_4^{2-} , which are used as upper and lower bounds to identify perovskite precursor species in Figure 5A.

Our DFT results suggest that the new absorbance peak that arises when an antisolvent is added is likely to be due to an increasing population of MA_xPbI_4 species. There is a very clear trend that the lower the dielectric constant of the solution, the more abundant the MA_xPbI_4 species that exist compared to PbI_4^{2-} . These results are thus consistent with our computational findings that a lower dielectric constant environment enhances the incorporation of MA^+ cations with iodoplumbate species.

3.4.4. ^{207}Pb -NMR results analysis

^{207}Pb -NMR was employed to probe the change in electron density around the lead atoms in different solvent-antisolvent combinations. First, we studied the effect of changing

concentrations of PbI_2 and MAI, where we found that increasing PbI_2 concentration alone in DMF resulted in an upfield shift (see Figure S1 in Electronic Supplementary Information). It should be noted that the appearance of a single peak, despite the presence of multiple iodoplumbate species in solution, is likely due to chemical exchange occurring on the same order of magnitude time scale as that of the detection period.⁵⁰ This is consistent with a previous report on solution-state ^{207}Pb -NMR study of lead halide perovskites.⁵¹ Therefore, a single peak represents the averaged frequency of the relative populations of iodoplumbate species present in the solution sample. A single peak also indicates that all the iodoplumbate species in the solution are in dynamic equilibrium. Increasing MAI concentration with a fixed PbI_2 concentration initially caused a downfield shift until a considerable excess of MAI was introduced (20 MAI:1 Pb molar ratio), at which point an upfield shift was observed (see Figure S2 in Electronic Supplementary Information†). To understand the effect of varying the dielectric constant of the antisolvent on the electron density around the lead atoms, we performed ^{207}Pb -NMR studies on solution samples of 0.075 M PbI_2 and 0.2 M MAI in a 2:1 molar ratio of DMF to antisolvent; the results are shown in Figure 7. Similarly, a set of samples prepared with identical PbI_2 and MAI concentrations, but in 3:1 ratios of DMF to antisolvent was also measured and analyzed. The results showed an identical trend of chemical shift as a function of dielectric constant of the precursor solution to the results for the 2:1 ratio (see Figure S3 in Electronic Supplementary Information†). Only a single peak was observed from each sample during the ^{207}Pb -NMR measurements, which suggests that multiple species are in dynamic equilibrium, with exchange rates faster than the time scale of the NMR measurements. As a result, the chemical shift represents the average change in relative amounts of multiple species in solution, as well as an overall change in electronic shielding around the lead atoms.

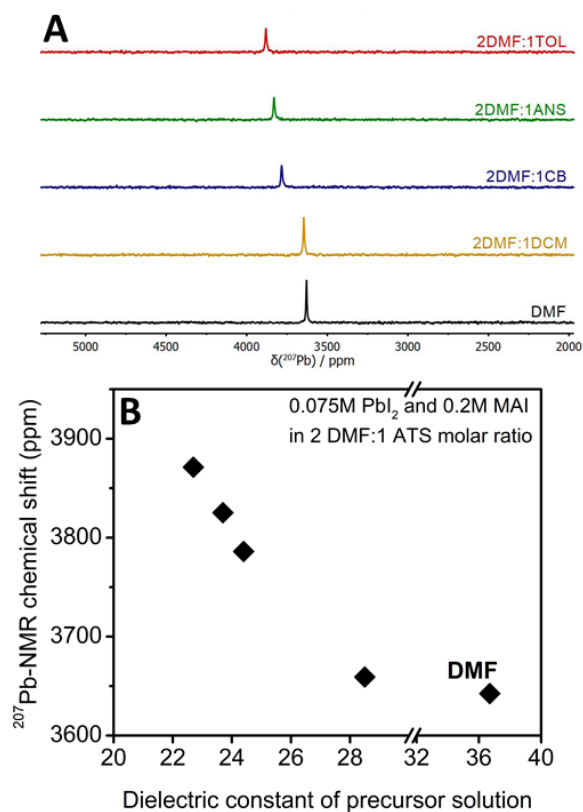


Figure 7. (A) Solution-state ^{207}Pb -NMR spectra of 0.075 M PbI_2 and 0.2 M MAI in pure DMF and in a 2:1 molar ratio of DMF to antisolvents with varying dielectric constants. $\text{Pb}(\text{NO}_3)_2$ was used as a standard. (B) ^{207}Pb -NMR chemical shift as a function of the dielectric constant of the precursor solution. The result shows a clear trend in downfield chemical shift with incorporation of a lower dielectric constant antisolvent.

The ^{207}Pb -NMR results in Figures 7A and B show a clear trend of downfield shift caused by the incorporation of an antisolvent with lower dielectric constant, which, in turn, lowers the dielectric of the precursor solution. Figures S4 and S5 in the Electronic Supplementary Information also show the effect of increasing the MAI concentration on both 3:1 and 2:1 binary solvent mixtures of DMF and antisolvent. These results suggest that the electronic shielding around the lead atoms decreases with the addition of the antisolvents. This trend contradicts the general effect

of dielectric constant on chemical shift in NMR.⁵² Instead, the trend we observed should be viewed as a result of reduced electron density around the lead atoms caused by increased binding of MA⁺ cations to iodoplumbate species. Using this interpretation, our ²⁰⁷Pb-NMR results also support the computational findings that the p interactions between the Pb atom in precursor species and the antisolvent do indeed lack electron donation from the antisolvent to the Pb.

3.4.5. Effect of antisolvent on grain sizes of MAPbI₃ film

Finally, we extended these atomic/molecular-scale studies by looking at the ultimate effect of changing the antisolvent at a more macroscopic level. To do so, we tested the computational findings by characterizing the grain sizes of MAPbI₃ thin films prepared from solutions of each antisolvent in this study. Based on classical nucleation theory,⁵³ we hypothesized that a lower overall dielectric constant of the solution will promote interactions between the MA⁺ cation and iodoplumbate species, and that this would result in higher nucleation rates, higher nucleation density, and smaller final grain size. In contrast, a higher dielectric constant solvent would result in fewer nuclei and thus larger grains. Films were prepared using an antisolvent dripping method, in which an abrupt supersaturation of a MAPbI₃ precursor solution, followed by nucleation and growth of MAPbI₃ crystallites, is induced by dripping the antisolvent during the spin-coating process. A detailed description of this process is provided in the “Thin Film Fabrication” section in Experimental Methods. Images of film samples prepared with 1M MAPbI₃ in DMF and incorporating various dielectric constant antisolvents in this dripping process are shown in Figure S6 of the Electronic Supplementary Information.

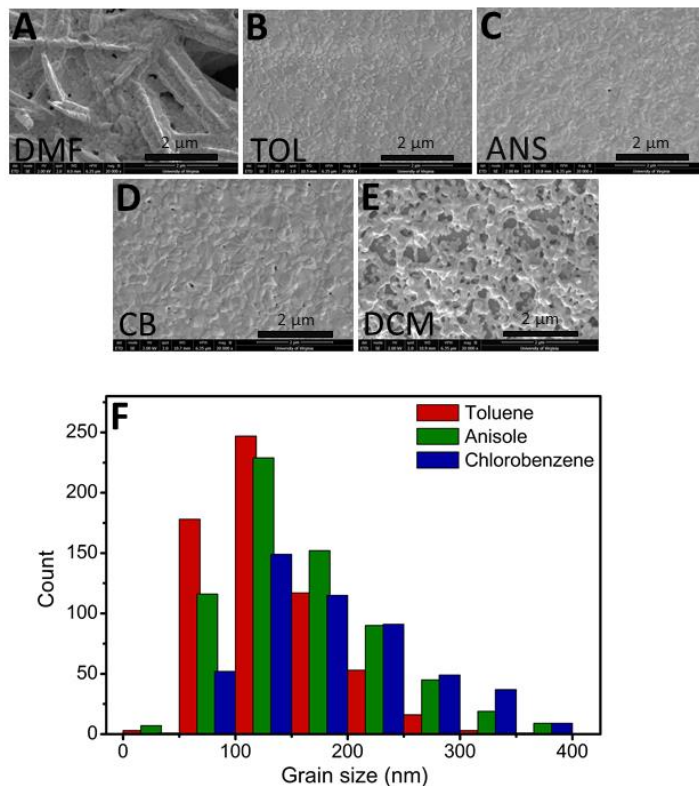


Figure 8. (A-E) SEM images showing grain sizes of MAPbI₃ thin films prepared by the antisolvent dripping method. (A) With no antisolvent dripping process, MAPbI₃ in pure DMF yields grains with needle-like morphology. (B)-(E) MAPbI₃ films made with various antisolvents using a dripping process results in a smoother, more continuous grain morphology. (F) Histogram of grain size population analyzed from MAPbI₃ films prepared with various antisolvents. As the dielectric constant of the antisolvent incorporated in the thin film increases, the larger and more poly-dispersed grains were formed.

Numerous studies in the literature^{24,54-56} have reported the significance of antisolvent-induced perovskite crystallization to yield smooth, high-quality films that are ideal for device application. Similar to previous studies,^{57,58} we observed that the films fabricated with 1M MAPbI₃ in DMF precursor solutions using a one-step method yielded a needle-like morphology (Figure 7A

and Figure S7 in Electronic Supplementary Information), possibly indicating the formation of perovskite-DMF adducts. Similarly, introducing antisolvent directly to the precursor solution prior to spin-coating also produced an impure phase of MAPbI₃, represented by pale yellow discoloration and needle-like structure. On the other hand, films fabricated using an antisolvent dripping method yielded smoother, pinhole-free morphologies with rounder grains, which allowed us to observe a more coherent comparison of grain sizes between films. As shown in Figure 8A and S8, the SEM images of samples prepared using antisolvents of varying dielectric constant show a consistent trend of decreased grain sizes with lower dielectric constant antisolvents. The grain size distribution analysis (8B) revealed that antisolvents with a lower dielectric constant yield smaller average grain sizes, but also a narrower distribution of the grain sizes. The only exception to this trend was the film made with DCM; the morphology of the sample was quite similar to that of the DMF sample in which no antisolvent dripping was employed, with rougher, irregular grains and a less uniform film coverage with many pinholes. The surface of the film resembled that of the DMF sample, with a significantly duller appearance compared to other antisolvent incorporated films (see Figure S6 in the Electronic Supplementary Information). Based on this result, we suspect that DCM with its (relatively) high dielectric constant has similar effects to DMF on the crystallization and growth behavior of MAPbI₃. These results for grain size add further supporting evidence to our hypothesis that the dielectric of the precursor solution, tuned by the judicious addition of a suitable choice of antisolvent can, indeed, promoted slower nucleation rates, a lower nucleation density, and hence larger final grain size.

3.5. Conclusion

This work has provided significant evidence to support the widely held, but largely unexplained, hypothesis that antisolvents “extract” processing solvents when applied during HOIP processing through an unknown atomic-scale mechanism. Using complementary approaches of DFT calculations, UV-Vis and ^{207}Pb NMR experiments, we provide details on the complexation between the precursor species and explain how the dielectric of the precursor solution can be used to control nucleation by the addition of an antisolvent. We demonstrate the ability of antisolvents to be tuned (using its dielectric constant) to promote the formation of a newly identified MA_xPbI_4 species, which decreases the solute concentration of MA^+ and PbI_3^- in solution, thus decreasing the saturation ratio S in equation 1. Importantly, our findings suggest that control over grain size and distribution in the final thin film can be gained by making a rational choice of antisolvents based on its dielectric constant and the nature of the interaction between the antisolvent and precursor plumbates.

3.6. Reference

1. A. Kojima, K. Teshima, Y. Shirai and T. Miyasaka, *Journal of the American Chemical Society*, 2009, **131**, 6050–6051.
2. <https://www.nrel.gov/pv/cell-efficiency.html-01-24-2019.pdf>. *The National Renewable energy Laboratory*, Accessed October 19 2018.
3. N. J. Jeon, H. Na, E. H. Jung, T.-Y. Yang, Y. G. Lee, G. Kim, H.-W. Shin, S. I. Seok, J. Lee and J. Seo, *Nature Energy*, 2018, **3**, 682–689.
4. W. S. Yang, B.-W. Park, E. H. Jung, N. J. Jeon, Y. C. Kim, D. U. Lee, S. S. Shin, J. Seo, E. K. Kim, J. H. Noh *et al.*, *Science*, 2017, **356**, 1376–1379.
5. W. A. Dunlap-Shohl, Y. Zhou, N. P. Padture and D. B. Mitzi, *Chemical reviews*, 2018, **119**, 3193–3295.
6. H.S. Kim, A. Hagfeldt and N.-G. Park, *Chemical communications*, 2019, **55**, 1192–1200.
7. A. Sharenko and M. F. Toney, *Journal of the American Chemical Society*, 2016, **138**, 463–470.
8. B. J. Foley, J. Girard, B. A. Sorenson, A. Z. Chen, J. S. Niezgod, M. R. Alpert, A. F. Harper, D.-M. Smilgies, P. Clancy, W. A. Saidi *et al.*, *Journal of Materials Chemistry A*, 2017, **5**, 113–123.
9. A. G. Ortoll-Bloch, H. C. Herbol, B. A. Sorenson, M. Poloczek, L. A. Estroff and P. Clancy, *Crystal Growth & Design*, 2019.
10. L. Li, Y. Chen, Z. Liu, Q. Chen, X. Wang and H. Zhou, *Advanced materials*, 2016, **28**, 9862–9868.
11. Y. Zhou, M. Yang, A. L. Vasiliev, H. F. Garces, Y. Zhao, D. Wang, S. Pang, K. Zhu and N. P. Padture, *Journal of Materials Chemistry A*, 2015, **3**, 9249–9256.
12. G. E. Eperon, V. M. Burlakov, P. Docampo, A. Goriely and H. J. Snaith, *Advanced Functional Materials*, 2014, **24**, 151–157.
13. D. Wang, Z. Liu, Z. Zhou, H. Zhu, Y. Zhou, C. Huang, Z. Wang, H. Xu, Y. Jin, B. Fan *et al.*, *Chemistry of Materials*, 2014, **26**, 7145–7150.
14. T. Salim, S. Sun, Y. Abe, A. Krishna, A. C. Grimsdale and Y. M. Lam, *Journal of Materials Chemistry A*, 2015, **3**, 8943–8969.
15. G. Yang, C. Wang, H. Lei, X. Zheng, P. Qin, L. Xiong, X. Zhao, Y. Yan and G. Fang, *Journal of Materials Chemistry A*, 2017, **5**, 1658–1666.

16. N. J. Jeon, J. H. Noh, Y. C. Kim, W. S. Yang, S. Ryu and S. I. Seok, *Nature materials*, 2014, **13**, 897.
17. A. J. Pearson, *Journal of Materials Research*, 2017, **32**, 1798–1824.
18. M. Xiao, F. Huang, W. Huang, Y. Dkhissi, Y. Zhu, J. Etheridge, A. Gray-Weale, U. Bach, Y.-B. Cheng and L. Spiccia, *Angewandte Chemie International Edition*, 2014, **53**, 9898–9903.
19. M. Saliba, T. Matsui, J.-Y. Seo, K. Domanski, J.-P. Correa-Baena, M. K. Nazeeruddin, S. M. Zakeeruddin, W. Tress, A. Abate, A. Hagfeldt *et al.*, *Energy & environmental science*, 2016, **9**, 1989–1997.
20. Y. Zhou, M. Yang, W. Wu, A. L. Vasiliev, K. Zhu and N. P. Padture, *Journal of Materials Chemistry A*, 2015, **3**, 8178–8184.
21. Y. Zhou, M. Yang, O. S. Game, W. Wu, J. Kwun, M. A. Strauss, Y. Yan, J. Huang, K. Zhu and N. P. Padture, *ACS applied materials & interfaces*, 2016, **8**, 2232–2237.
22. D. Bi, W. Tress, M. I. Dar, P. Gao, J. Luo, C. Renevier, K. Schenk, A. Abate, F. Giordano, J.-P. C. Baena *et al.*, *Science advances*, 2016, **2**, e1501170.
23. M. Yavari, M. Mazloun-Ardakani, S. Gholipour, M. M. Tavakoli, S.-H. Turren- Cruz, N. Taghavinia, M. Grätzel, A. Hagfeldt and M. Saliba, *Advanced Energy Materials*, 2018, 1800177.
24. S. Paek, P. Schouwink, E. N. Athanasopoulou, K. Cho, G. Grancini, Y. Lee, Y. Zhang, F. Stellacci, M. K. Nazeeruddin and P. Gao, *Chemistry of Materials*, 2017, **29**, 3490–3498.
25. T. Bu, L. Wu, X. Liu, X. Yang, P. Zhou, X. Yu, T. Qin, J. Shi, S. Wang, S. Li *et al.*, *Advanced Energy Materials*, 2017, **7**, 1700576.
26. M. D. Hanwell, D. E. Curtis, D. C. Lonie, T. Vandermeersch, E. Zurek and G. R. Hutchison, *Journal of cheminformatics*, 2012, **4**, 17.
27. F. Neese, *Wiley Interdisciplinary Reviews: Computational Molecular Science*, 2018, **8**, e1327.
28. J. Stevenson, B. Sorenson, V. H. Subramaniam, J. Raiford, P. P. Khlyabich, Y.-L. Loo and P. Clancy, *Chemistry of Materials*, 2016, **29**, 2435–2444.
29. B. A. Sorenson, S. S. Hong, H. C. Herbol and P. Clancy, *Computational Materials Science*, 2019, **170**, 109138.
30. S. Grimme, *J. Comp. Chem.*, 2006, **27**, 1787–1799.
31. S. Grimme, S. Ehrlich and L. Goerigk, *Journal of computational chemistry*, 2011, **32**, 1456–1465.

32. F. Weigend and R. Ahlrichs, *Physical Chemistry Chemical Physics*, 2005, **7**, 3297–3305.
33. S. Grimme, J. Antony, S. Ehrlich and H. Krieg, *The Journal of chemical physics*, 2010, **132**, 154104.
34. Y. Zhao and D. G. Truhlar, *The Journal of Physical Chemistry A*, 2005, **109**, 5656–5667.
35. H. Kruse and S. Grimme, *The Journal of chemical physics*, 2012, **136**, 04B613.
36. G. Eperon and V. Burlakov, *Adv. Funct. Mater.*, 2014, **24**, 151–157.
37. A. Klamt and G. Schüürmann, *Journal of the Chemical Society, Perkin Transactions 2*, 1993, 799–805.
38. D. M. York and M. Karplus, *The Journal of Physical Chemistry A*, 1999, **103**, 11060–11079.
39. <https://depts.washington.edu/eoopic/linkfiles/dielectricchart>TheUniversityofWashington; Accessed June 12 2020-919.
41. P. Wang and A. Anderko, *Fluid Phase Equilibria*, 2001, **186**, 103–122.
42. A. E. Nielsen, *Kinetics of precipitation*, Pergamon, 1964, vol. 18.
43. M. Jung, S.-G. Ji, G. Kim and S. I. Seok, *Chemical Society Reviews*, 2019, **48**, 2011–2038.
44. T. D. Storm, R. A. Hazleton and L. E. Lahti, *Journal of Crystal Growth*, 1970, **7**, 55–60.
45. K. G. Stamplecoskie, J. S. Manser and P. V. Kamat, *Energy & Environmental Science*, 2015, **8**, 208–215.
46. A. Sharenko, C. Mackeen, L. Jewell, F. Bridges and M. F. Toney, *Chemistry of Materials*, 2017, **29**, 1315–1320.
47. G. Zhang and C. B. Musgrave, *The journal of physical chemistry A*, 2007, **111**, 1554–1561.
48. J.-L. Bredas, *Materials Horizons*, 2014, **1**, 17–19.
49. J. P. Perdew, *International Journal of Quantum Chemistry*, 1985, **28**, 497–523.
50. I. R. Kleckner and M. P. Foster, *Biochimica et Biophysica Acta (BBA)-Proteins and Proteomics*, 2011, **1814**, 942–968.
51. F. Coleman, G. Feng, R. W. Murphy, P. Nockemann, K. R. Seddon and M. Swadźba-Kwaśny, *Dalton Transactions*, 2013, **42**, 5025–5035.
52. I. G. Shenderovich, A. P. Burtsev, G. S. Denisov, N. S. Golubev and H.-H. Limbach, *Magnetic Resonance in Chemistry*, 2001, **39**, S91–S99.
53. J. De Yoreo, *Nature materials*, 2013, **12**, 284.
54. D. Gedamu, I. M. Asuo, D. Benetti, M. Basti, I. Ka, S. G. Cloutier, F. Rosei and R. Nechache, *Scientific reports*, 2018, **8**, 1–11.

55. B.-E. Cohen, S. Aharon, A. Dymshits and L. Etgar, *The Journal of Physical Chemistry C*, 2016, **120**, 142–147.
56. Y. Yu, S. Yang, L. Lei, Q. Cao, J. Shao, S. Zhang and Y. Liu, *ACS applied materials & interfaces*, 2017, **9**, 3667–3676.
57. K. Yan, M. Long, T. Zhang, Z. Wei, H. Chen, S. Yang and J. Xu, *Journal of the American Chemical Society*, 2015, **137**, 4460–4468.
58. A. A. Petrov, I. P. Sokolova, N. A. Belich, G. S. Peters, P. V. Dorovatovskii, Y. V. Zubavichus, V. N. Khrustalev, A. V. Petrov, M. Gratzel, E. A. Goodilin et al., *The Journal of Physical Chemistry C*, 2017, **121**, 20739–20743.

3.7. Supplementary Information

3.7.1. Solvent-antisolvent interaction

Table S1. Intermolecular binding energies (in kcal/mol) of solvent pairs used in perovskite precursor solution processing as a function of the dielectric constant (column 1), arranged in decreasing value of the pair. Columns 2 and 3: Binding energy results for DMF interacting with five different antisolvents. Columns 4 and 5: Binding energy results for same-solvent pairs, for comparison.

ϵ	DMF-ATS	Binding Energy	Same solvents	Binding Energy
36.7	DMF-DMF	-1.95	DMF-DMF	-1.95
28.54	DMF-DCM	-2.86	DCM-DCM	-2.29
26.64	DMF-THF	-0.80	THF-THF	-1.92
24.38	DMF-CB	-3.45	CB-CB	-2.44
23.73	DMF-ANS	-3.60	ANS-ANS	-3.88
22.66	DMF-TOL	-3.96	TOL-TOL	-3.46

3.7.2. Solvent-HOIP precursor interactions

Table S2. Comparison of the intermolecular binding energy of a variety of solvents to a MAPbI₃ monomer (column 3) to the binding energy of a MA⁺ cation to a complex formed by PbI₃⁻ and a solvent molecule (column 5) in the perovskite precursor solution. Intermolecular binding energies are given in kcal/mol.

ϵ	Solvent-MAPbI ₃ Interaction	Binding Energy	MA ⁺ -PbI ₃ solvent Interaction	Binding Energy
36.7	DMF- MAPbI ₃	-6.58	MA ⁺ -(PbI ₃ DMF)	-6.70
28.54	DMF- MAPbI ₃	-4.07	MA ⁺ -(PbI ₃ DCM)	-6.72
26.64	DMF- MAPbI ₃	-7.33	MA ⁺ -(PbI ₃ THF)	-7.74
24.38	DMF- MAPbI ₃	-7.38	MA ⁺ -(PbI ₃ CB)	-7.60
23.73	DMF- MAPbI ₃	-8.59	MA ⁺ -(PbI ₃ ANS)	-7.86
22.66	DMF- MAPbI ₃	-8.88	MA ⁺ -(PbI ₃ TOL)	-8.19

3.7.3. Effect of changing PbI_2 concentration

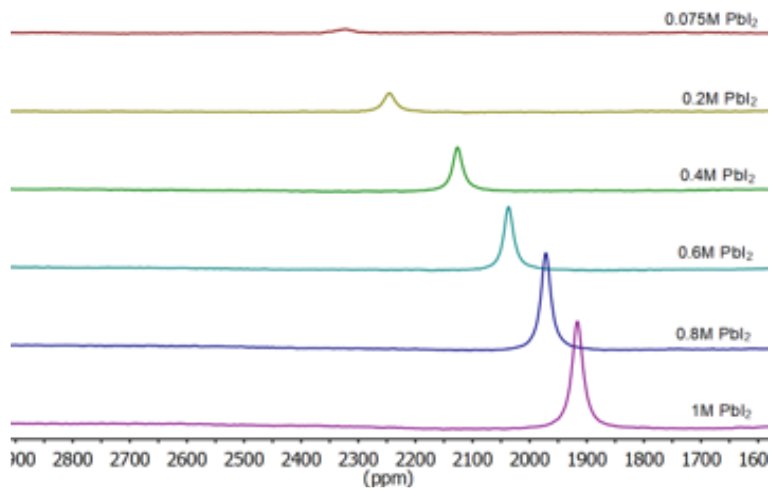


Figure S1. Solution-state ^{207}Pb -NMR spectra for various concentrations of PbI_2 ranging from 0.075 M to 1 M. An upfield shift and stronger peak intensity were observed with increasing PbI_2 concentration.

3.7.4. Effect of changing MAI concentration

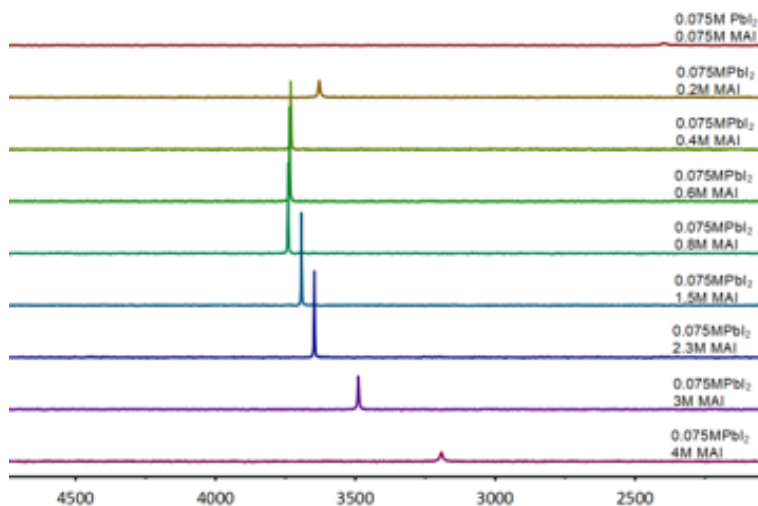


Figure S2. Solution-state ^{207}Pb -NMR spectra of 0.075 M PbI_2 with varying MAI concentration from 0.075 M (equimolar) to 4 M. Initially, a downfield shift was observed until the molar ratio is

0.075 M PbI_2 :0.8 M MAI; MAI concentrations greater than 0.8 M resulted in an upfield shift. The presence of considerable excess MAI also yielded a significant decrease in peak intensity.

3.7.5. Effect of antisolvents of varying dielectric constant and increasing MAI concentration

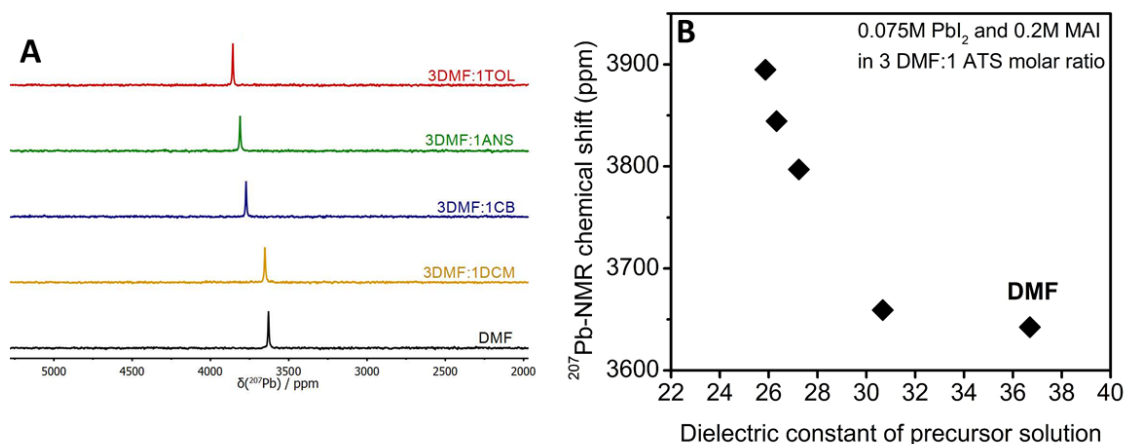


Figure S3. (A) Solution-state ^{207}Pb -NMR spectra of 0.075 M PbI_2 and 0.2 M MAI in pure DMF and in a 3:1 molar ratio of DMF to antisolvents with varying dielectric constants. (B) ^{207}Pb -NMR chemical shift as a function of the dielectric constant of the precursor solution. A clear trend in downfield shift is observed when an antisolvent with a lower dielectric constant is incorporated into the precursor solution.

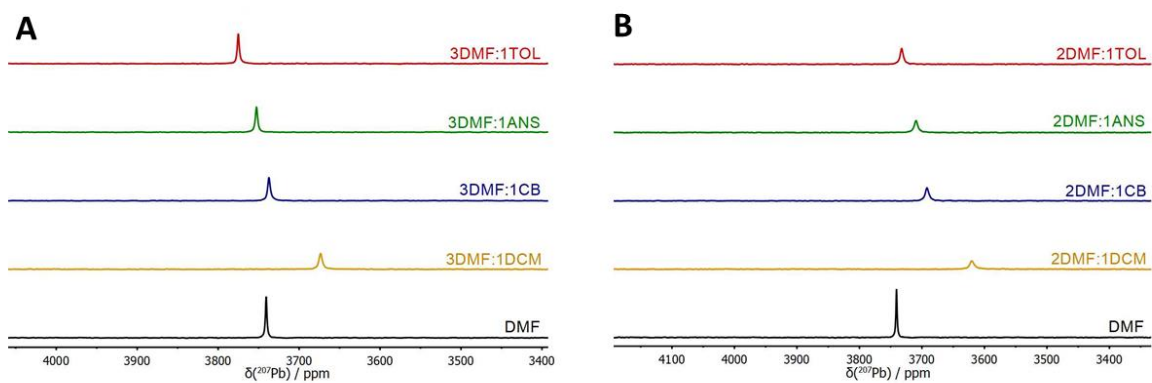


Figure S4. Solution-state ^{207}Pb -NMR spectra of 0.075 M PbI_2 and 0.8 M MAI in pure DMF and in a (A) 2:1 molar ratio and (B) 3:1 molar ratio of DMF to antisolvents with varying dielectric constants.

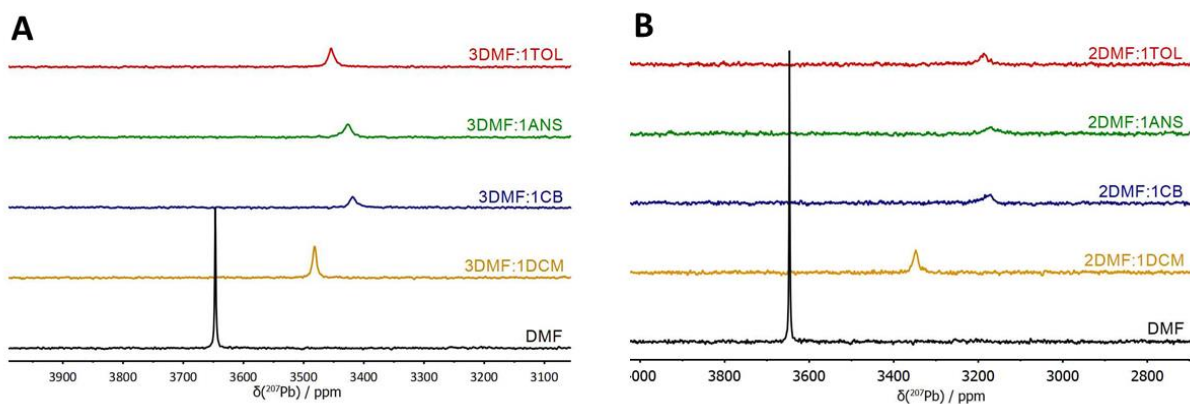


Figure S5. Solution-state ^{207}Pb -NMR spectra of 0.075 M PbI_2 and 2.3 M MAI in pure DMF and in a (A) 2:1 molar ratio and (B) 3:1 molar ratio of DMF to antisolvents with varying dielectric constants.

3.7.6. Fabricated thin films

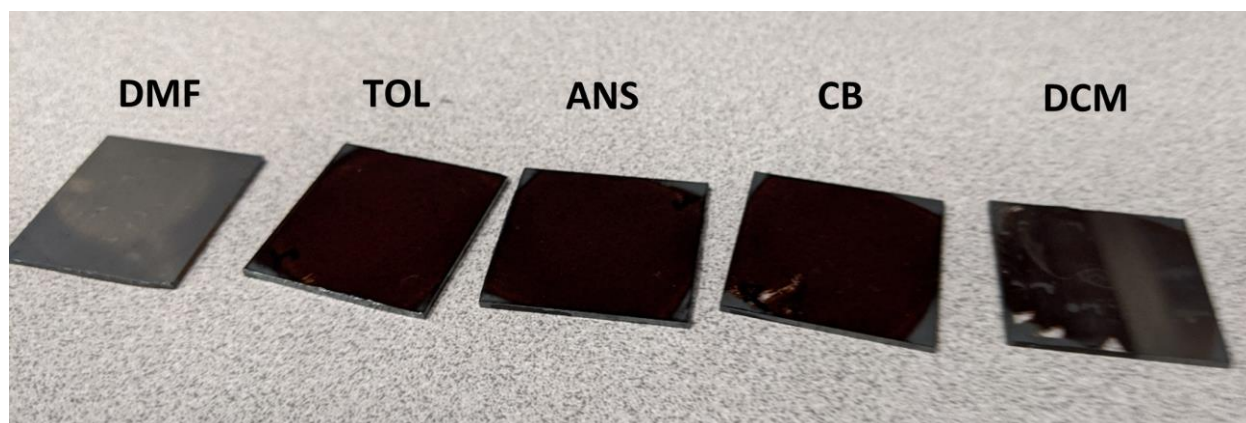


Figure S6. Images of thin films fabricated using 1 M MAPbI₃ in DMF prepared using an antisolvent dripping method. The film denoted as DMF (leftmost image) was prepared with no antisolvent. The surfaces of the films prepared with DMF (leftmost) and DCM (rightmost) show significant dullness and roughness compared to those of the other films.

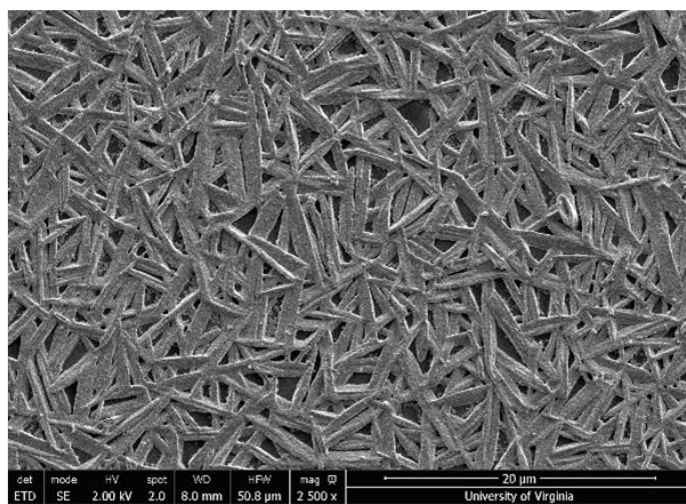


Figure S7. SEM image of a film fabricated using 1 M MAPbI₃ in DMF with no antisolvent. The film shows a needle-like morphology with pinholes. A magnification of 2.5k was used with a scale bar of 20 μm.

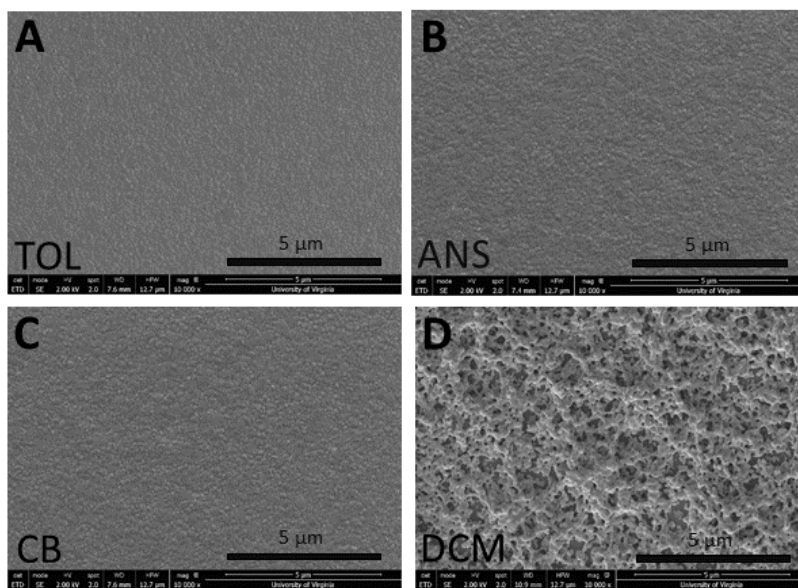


Figure S8. SEM images of the films fabricated with 1M MAPbI₃ in DMF using antisolvent dripping method with the antisolvent (A) TOL (B) ANS (C) CB and (D) DCM. 10 k magnification was used with the scale bar 5 μm.

Chapter 4: Exciton Dissociation in Quantum Dots Connected with Photochromic Molecule Bridges

This chapter was adopted from the manuscript submitted in July 2021.

4.1. Abstract

We report modulation of exciton dissociation dynamics in quantum dots (QD) connected with photochromic molecules. Our results show that switching the configuration of photochromic molecules changes the inter-QD potential barrier height which has a major impact on the charge tunneling and exciton dissociation. The switching of the dominant exciton decay pathway between the radiative recombination and exciton dissociation results in switchable photoluminescence intensity from QDs. Implications of our findings for the optical memory and optical computing applications are discussed.

4.2. Introduction

Quantum dots (QDs) are scientifically intriguing and technologically promising nanoscale building blocks for hierarchical materials with tunable emergent properties.¹⁻⁷ A wide range of tunable properties of QDs has been demonstrated, the most prominent being the size-tunable optical properties from programmable atomic-like energy levels⁷⁻⁹ from which the view of QDs as 'designer atoms' originates. Moreover, in assemblies of multiple QDs, the electronic interaction between adjacent QDs can be viewed as programmable 'designer bonds' because of the tunable inter-QD distances and electronic coupling strengths. Considering that manipulating the structure

of QD assemblies is possible by controlling the rich self-assembly behaviors of QDs,¹⁰⁻¹⁵ one can imagine building 'designer QD solids' that give rise to novel properties.¹⁶⁻¹⁷

Previous studies have shown that the length of the molecules that inter-connect QDs and their end group moieties can have major influence over charge conduction,¹⁸⁻²⁷ exciton dissociation²⁸⁻²⁹ and surface trap densities.^{25, 27} Most of studies so far have been focused on achieving strong electronic coupling required for optoelectronic device applications. To this end, a variety of short organic molecules such as ethanedithiol,^{28, 30-32} benzenedithiol³³, mercaptopropionic acid²⁹ and thiocyanate³⁴⁻³⁵ has been employed. Also, short metal chalcogenide complex ligands³⁶ have been shown to result in extremely strong inter-CQD electronic coupling.³⁷ Atomic anions, as the ultimate short ligands, have been demonstrated in CQD solar cells²⁵ and field-effect transistor devices.³⁸

Despite progress in achieving large electronic coupling using short ligands, the microscopic understanding of the impact of physical and electronic structure of bridge molecules on charge transfer and exciton dynamics in QD assemblies is still lacking. To effectively leverage the large library of possible bridge molecules and realize the full potential of QD 'designer solids', a deeper understanding that goes beyond merely tuning the length of bridge molecule is required. Specifically, the effect of changing potential barrier heights through different molecular structure on charge transfer and exciton dynamics in QD assemblies is still poorly understood. This is challenging to study because employing a set of bridge molecules designed to provide different potential barrier height in general will also introduce differences in other key factors such as molecule length and binding groups that have major impact on charge transfer. Moreover, comparing charge transfer behavior in multiple samples with different molecular structures will

introduce variability in charge donors and acceptors due to inhomogeneities in QD populations such as different sizes, shapes and different bonding with molecules.

Here, we report a study that tests a hypothesis that optically switching the configuration and the energy levels of the photochromic bridge molecules will enable tuning of the potential barrier height between the QDs and therefore the charge transfer rate and exciton dynamics (Figure 1). QDs connected with a configuration of photochromic molecules with large energy gap between highest occupied molecular orbital (HOMO) and lowest unoccupied molecular orbital (LUMO) will provide a larger potential barrier height and smaller electronic coupling between the QDs compared to a configuration with a smaller energy gap. A direct consequence of changing inter-QD electronic coupling and the degree of exciton delocalization is different rates of exciton dissociation.²⁸⁻²⁹ Our results indeed show that the changing the photochromic molecules' configuration and its associated inter-QD potential barrier height can switch the dominant pathway for the excitons in QDs between radiative recombination or tunneling induced exciton dissociation (Figure 1). Our approach of exploiting configuration switching of the photochromic molecules while keeping other key factors constant (exactly identical charge donor-acceptor QD pairs, identical binding at contacts between the molecules and QD surface, etc.) is an advantageous method to isolate and study how changing potential barrier height impact inter-CQD exciton dissociation and charge transfer. The switching of the dominant exciton decay pathway between the radiative recombination and exciton dissociation results in switchable photoluminescence (PL) intensity from QDs which can be exploited in optical memory and optical computing applications.

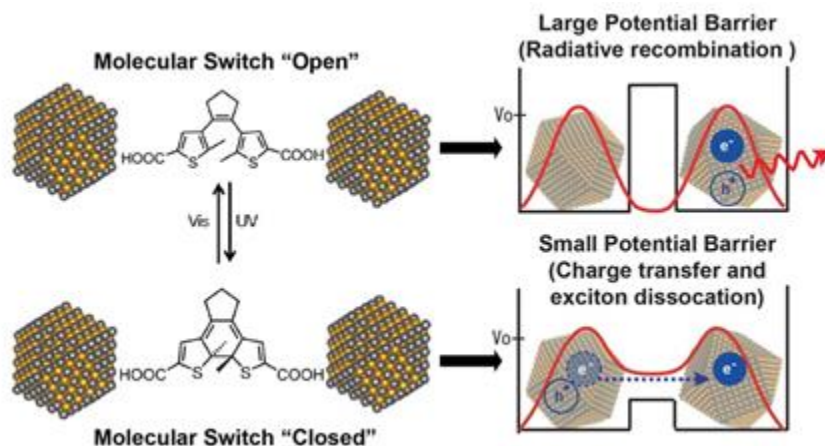


Figure 1. A schematic showing a mechanism of modulating charge transfer and exciton dissociation in QD assemblies by optically switching the configuration of bridge molecules to change the inter-QD potential barrier heights.

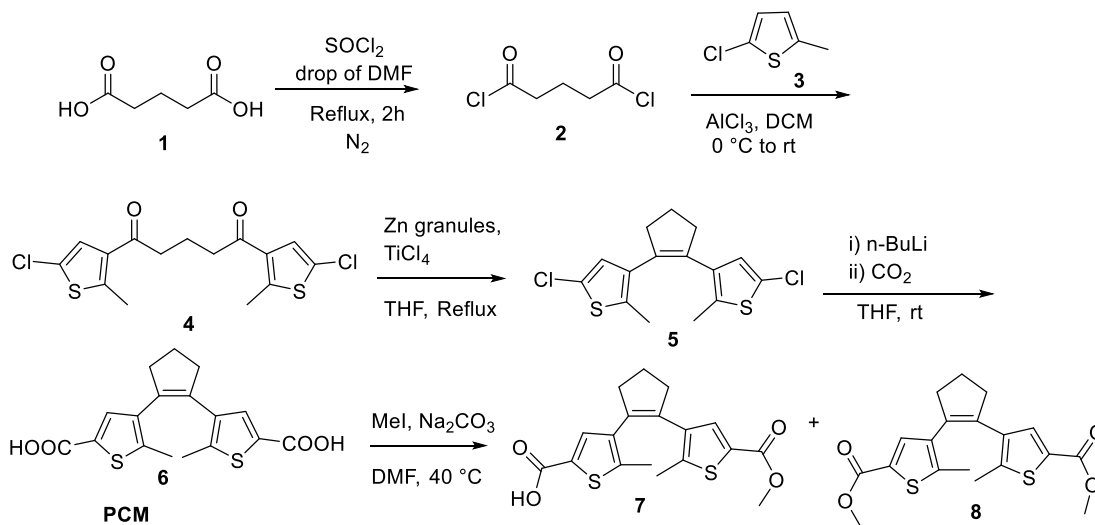
Dithienylethenes derivatives were chosen as the photochromic molecules in this study for the following reasons: (1) reversible configuration change with ultraviolet or visible light irradiation,³⁹⁻⁴³ (2) minimal differences in molecular length between the configurations ($\sim 1 \text{ \AA}$),⁴⁰ (3) a large change in HOMO-LUMO energy gap upon configuration change ($\sim 2 \text{ eV}$)⁴⁴ and (4) fast switching speeds of a few picoseconds.⁴⁵ As for the QDs, PbS QDs were selected because of their high degree of electronic coupling and low exciton binding energy.²⁸ This will enable more sensitive detection of change in exciton dissociation.²⁸ Also importantly, the near-IR absorbance and PL of PbS QDs will allow monitoring of the exciton dynamics in QD assemblies in the range of light wavelength regions that do not disturb the configuration of the dithienylethene molecules.

4.3. Methods

4.3.1. Photochromic molecules (PCMs) syntheses

All reactions were carried out under anhydrous conditions at 1 atm, these were typically carried out in flame dried glassware under nitrogen or argon atmosphere. All reagents and solvents were obtained from commercial suppliers such as Sigma-Aldrich, VWR, and Fisher and used directly without any purifications. All reactions unless otherwise noted were carried out in flame dried glassware under nitrogen or argon atmosphere. All purification was conducted by flash chromatography using 230-400 mesh silica gel using gradient solvent systems.

Thin-layer chromatography (TLC) analysis was performed with aluminum backed TLC plates with UV and fluorescence indicator and visualized using UV lamp at 254 nm, then stained with PMA solution. ^1H NMR and proton-decoupled ^{13}C NMR spectra were obtained with Bruker 400 MHz spectrometers in $\text{DMSO-}d_6$ or CDCl_3 . The chemical shifts were reported using $\text{CDCl}_3/\text{DMSO-}d_6$ as internal standard at 7.26/2.50 ppm and at 77.0/39.5 ppm, respectively. 2D NMR experiments (HSQC, COSY) were also conducted to assist the compound characterizations.



Scheme S1. Synthesis of photochromic compound **6** and **7**.

Synthesis of compound 2:

Glutaric acid (200.0 mg, 1.51 mmol, 1.0 equiv.) was dissolved in 5.0 mL of thionyl chloride along with a drop of DMF, in nitrogen flushed 50.0 mL RBF and refluxed for 3 hr to see the intermediate formation. The reaction was further refluxed for 30 min and directly taken to the next step.

Synthesis of compound 4:

To a stirring mixture of an ice-cooled solution of dry AlCl_3 powder (605.5 mg, 4.54 mmol, 3.0 equiv.) in DCM (6.0 mL), glutaryl chloride (255.8 mg, 1.51 mmol, 1.0 equiv.) and 2-Chloro-5-methylthiophene (0.35 mL, 3.18 mmol, 2.1 equiv.) were successively added dropwise. The reaction mixture was stirred for 3 hr at RT, until the mixture turned dark red. A mixture of concentrated HCl (4.0 mL) and ice (6.0 g) was carefully added to the reaction flask. The water layer was extracted with DCM (3×10.0 mL). The combined organic phases were washed with a saturated aqueous solution of NaHCO_3 (6.0 mL), water (5.0 mL) and saturated NaCl solution (5.0 mL). The organic layer was then dried using anhydrous Na_2SO_4 and filtered. The solvent was evaporated using a rotavap under reduced pressure to yield a brown tar. The crude product was further purified by 3% EtOAc in hexanes to obtain the desired product as a white solid, in 84% (458.0 mg). yield

Synthesis of compound 5:

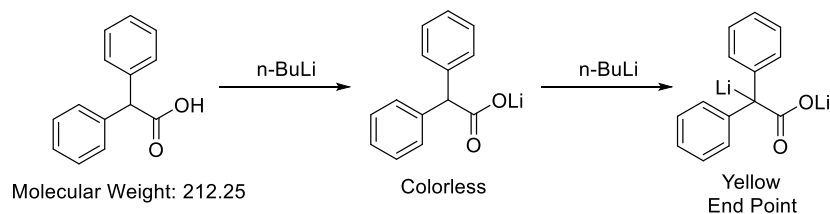
A mixture of TiCl_4 (0.15 mL, 1.38 mmol, 2.5 equiv.), Zn granules (434.4 mg, 6.64 mmol, 12.0 equiv) and THF (10.0 ml) was added to a round bottom flask under nitrogen, the mixture was stirred at refluxing condition for 1 hr. The mixture was cooled to 0 °C, and compound **4** (200.0 g, 0.55 mmol, 1.0 equiv.) dissolved in 2 mL THF was added. The mixture was refluxed for 14 hr

after which a full conversion was observed. The reaction mixture was then quenched with two drops of saturated aqueous K_2CO_3 and passed through celite and washed with EtOAc (20 mL X 3). The combined organic layers were washed with H_2O (20.0 mL) and saturated $NaHCO_3$ (20.0 mL) and then dried with anhydrous Na_2SO_4 and filtered. The solvent was removed using a rotavap under reduced pressure. Further purification was done using flash column chromatography using hexane as the eluent, the desired product was obtained as a white solid in 76% (139 mg) yield.

Synthesis of compound 6 (PCM):

Compound **5** (500.0 mg, 1.52 mmol, 1.0 equiv.) was dissolved in anhydrous THF (20.0 mL) in a round bottom flask equipped with drying tube and nitrogen atmosphere. To this solution, *n*-BuLi (4.0 mL, 0.94 M in hexanes, ACROS, 2.5 equiv.) was added. After a yellowish slurry was obtained, it was further stirred for 1 hr. Then, excess CO_2 solid was added at RT and the mixture was stirred for 45 min. The reaction was quenched by adding H_2O (10.0 mL) dropwise. The aqueous layer was acidified to pH of 1 with 2 M HCl and extracted with DCM (3 x 25 mL). The organic layer was washed with H_2O (30 mL) and dried over Na_2SO_4 . The organic layer was filtered and concentrated to obtain a brown slurry. The crude slurry was purified by flash column chromatography using solvent systems of hexanes/DCM to 2% MeOH/DCM to obtain a light brown solid as the desired product in 56% (296 mg) yield.

The concentration of *n*-butyl lithium was determined prior to reaction by the following method in Scheme S2.



Scheme S2. Detection of endpoint by titration.

Diphenylacetic acid (50.0 mg, 0.235 mmol, 1 equiv.) was added to a dried scintillation vial under N₂ atmosphere. Anhydrous THF (1.0 mL) was added to the scintillation vial. 700 μL of 1.6 N *n*-butyl lithium solution in hexanes was added slowly. The *n*-butyl lithium solution was added until the solution in the vial turned deep yellow. At the end of the titration, 450 μL of the *n*-butyl lithium solution remained in the syringe. The titration required 250 μL of the *n*-butyl lithium solution. The concentration of the *n*-BuLi was calculated using the following formula:

$$\frac{0.235 \text{ mmole Diphenylacetic acid}}{0.250 \text{ mL}} = 0.94 \text{ M}$$

Synthesis of compound 7 (mono-esterified PCM):

A mixture of compound **6** (100.0 mg, 0.29 mmol, 1.0 equiv.), DMF (5.0 mL), and Na₂CO₃ (121.7 mg, 1.15 mmol, 4.0 equiv.) was stirred for 30 min at rt. To this solution, CH₃I (19.6 μL, 0.29 mmol, 1.0 equiv.) was added dropwise and the mixture was stirred for 2 hr at 40 °C. The reaction was then stopped and DMF was removed under vacuum, the residue was diluted with H₂O and acidified with 2 M HCl solution (~pH 2). The aqueous layer was then extracted with DCM (10 mL X 2). The combined organic layer was washed with H₂O (20 mL) to remove residual DMF, dried over anhydrous Na₂SO₄ and concentrated under reduced pressure. The crude product was then purified by using flash chromatography (DCM to 1% MeOH/DCM) to afford a brown solid as the desired monoester **7** in 22% yield (23 mg, 0.063 mmol). The dimethyl ester byproduct **8** was also isolated in 27 mg (0.072 mmol, 50% yield based on CH₃I). R_f = 0.29 in 5% MeOH/DCM for compound **7**. m.p. 172.0-174.0 °C; ¹H NMR (400 MHz, CDCl₃) δ 7.57 (s, 1H), 7.50 (s, 1H), 3.84 (s, 3H), 2.79 (t, *J* = 7.4 Hz, 4H), 2.08 (m, *J* = 7.5 Hz, 2H), 1.94 (s, 3H), 1.92 (s, 3H); ¹³C NMR (100 MHz, CDCl₃) δ 166.5, 162.5, 144.6, 142.7, 137.0, 136.5, 135.9, 135.1, 134.6, 134.4, 129.4, 128.4, 52.0, 38.63, 38.61, 22.8, 14.9, 14.8.

4.3.2. PbS QD synthesis

3 mmol of lead (II) oxide (PbO) (99.999%, Alfa Aesar), 6 – 96 mmol of oleic acid (HOA) (90%, Sigma Aldrich), and 1-octadecene (90%, Alfa Aesar) were added to make 30 mL total volume in a three-neck flask. To synthesize different sizes of QD (2.9 – 4.7 nm in diameter), the molar ratio between PbO and HOA was varied from 2:1 to 32:1. The solution was stirred in a vacuumed flask at 130 °C for 1 hr until PbO was fully dissolved. Under Argon flow, the temperature was adjusted to 90 – 95 °C and stabilized prior to the precursor injection. In the N₂-filled glovebox, 0.1 M of hexamethyldisilathiane ((TMS)₂S) solution was prepared by mixing 378 μL of (TMS)₂S in 18 mL of 1-octadecene (ODE). 15 mL of 0.1 M (TMS)₂S solution was taken out of the glovebox and quickly injected into the three-neck flask. After 60 s, the reaction flask was put in an ice bath to quickly quench the temperature of the reaction solution. During the purification process, unreacted species were removed by a series of centrifuge steps after cleaning the product with methyl acetate and hexane. The final QD was stored in a solid form in the N₂ glovebox.

4.3.3. PCM treated PbS QD assembly preparation

Solutions of 10 mg/mL concentration of PbS QD in tetrachloroethylene (TCE) and 1.8 mM of PCM in methanol (MeOH) were prepared and stirred overnight in the N₂ glovebox prior to use. The glass substrates were sequentially cleaned by sonicating in Hellmanex soap solution, deionized water, iso-propanol and then acetone. Subsequently, the clean substrates were UV-ozone treated for 10 min. In the glovebox, 100 μL of PbS QD solution was statically dispensed onto the glass substrate, followed by a spin-coating at 2000 rpm for 60 s. Ligand exchange was done by placing 100 μL of the PCM solution onto the QD thin film for 60 s. The process was repeated two

more times. The film was rinsed with MeOH to remove any unbound excess ligands. The film was encapsulated with a glass slide using epoxy curing to prevent any complications from exposure to ambient air.

4.3.4. Absorbance, photoluminescence (PL), time-resolved photoluminescence (TR-PL) and Raman spectroscopy measurements

Absorbance measurement was performed using PerkinElmer Lambda 950S spectrophotometer equipped with an integrating sphere. PL measurements were taken using PTI Quantamaster 400 system. Time-resolved PL was taken with a time correlated single photon counting set-up with a pulsed 633 nm laser diode as the excitation light source. Raman spectroscopy measurement was performed using Renishaw Raman microscope with 514 nm laser as an excitation source and a 50x objective to focus the laser on the sample.

4.3.5. PL measurements on PCM treated QD samples

The encapsulated PCM treated QD thin film samples were placed on the stage in the spectrofluorometer. The light wavelength was changed to 300 nm or 541 nm to induce the configuration change of PCM. After inducing the configuration change of PCMs, without changing the position of the sample or any other parts of the setup, the excitation light wavelength was changed to 750 nm to obtain the PL spectra from QDs. All instrumental parameters such as slit widths, detector voltage, stage angle and etc. were kept constant throughout the measurements.

4.3.6. GISAXS measurement

GISAXS characterizations were performed at the 11-BM Complex Materials Scattering (CMS) beamline at the National Synchrotron Light Source II (NSLS-II) in the Brookhaven National Laboratory. Thin film samples were measured at incident angles from 0.10 to 0.25° with a $200\ \mu\text{m}$ (H)* $50\ \mu\text{m}$ (V) beam at $13.5\ \text{keV}$ (wavelength $\lambda = 0.9184\ \text{\AA}$). 2D scattering patterns were obtained using Dectris Pilatus2M at $2\ \text{m}$ downstream the samples.

4.4. Results and Discussion

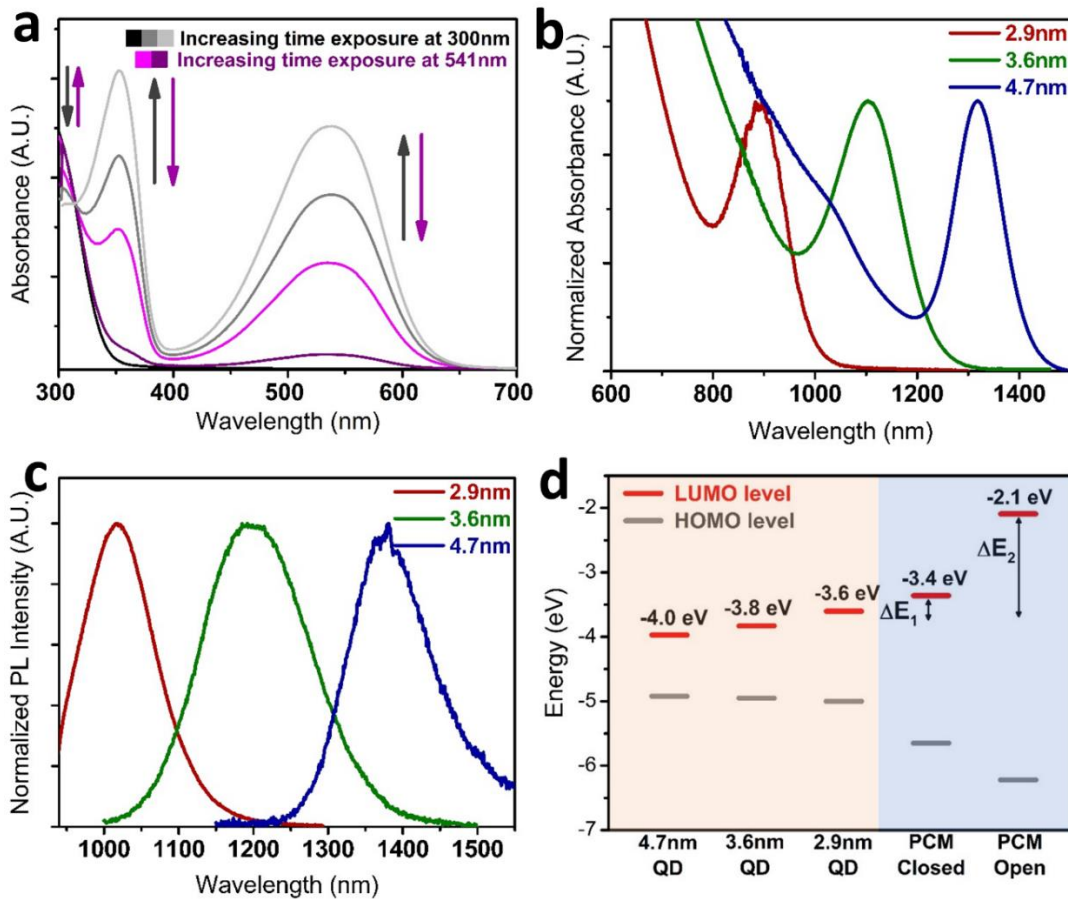


Figure 2. (a) Absorbance spectra of PCM in methanol solution after light irradiation at 300 nm or 541 nm to induce configuration switch. (b) Normalized absorbance spectra and (c) PL spectra of PbS QDs with different sizes (2.9 nm, 3.6 nm, and 4.7 nm) used for this study. (d) The HOMO-LUMO energy levels of QD with different sizes and PCM with “closed” or “open” configuration.⁶⁶

Specifically, dithienylethenes derivatives with carboxylic acid functional groups (compound **6** in Scheme S1 of the Supporting Information) were employed for the experiments in this study. From this point on, we will refer to the compound **6** simply as PCM (photochromic molecule). The PCM undergoes a photo-induced transition between its unconjugated open-ring isomer (referred to as an “open” state) and the conjugated closed-ring isomer (a “closed” state) (Figure 1).⁴² The change in electronic transition energies upon the configuration switch can be observed in the absorbance spectra of PCM shown in Figure 2a. As the configuration switch in the PCM populations progresses, the absorbance spectra show an isosbestic point at 320 nm. Upon exposure at 300 nm wavelength light, the absorbance peaks at 541 nm and 360 nm increase as more PCMs switch to the “closed” configuration. In contrast, irradiating the molecules with 541 nm wavelength light switches PCMs to the “open” state and therefore the absorbance peaks at 541 nm and 360 nm decrease. Based on these results, we selected 300 nm and 541 nm wavelength light to switch the configuration of the PCM to “closed” and “open” state respectively throughout this study.

Three different sizes of PbS QDs were employed for this study (see the Supporting Information for synthesis method). The size dependent energy gaps of QDs result in different energy levels of HOMO and LUMO, allowing us to systematically tune the potential barrier height with respect to the PCM’s energy levels. The absorbance and PL spectra of the synthesized PbS QDs are shown in Figure 2b and 2c. Based on the first excitonic peak energy of 1.39 eV, 1.03 eV,

and 0.90 eV in the absorbance spectra (Figure 2b), the diameter of PbS QDs were estimated to be 2.9 nm, 3.6 nm and 4.7 nm respectively, using a sizing curve in the literature.⁴⁶ Figure 2d shows a plot of corresponding HOMO and LUMO energy levels of PbS QDs and PCM according to the literature.⁴⁴ As the QD diameter gets smaller from 4.7 nm to 2.9 nm, the LUMO energy level increases from -4.0 eV to -3.6 eV with respect to the vacuum while the HOMO energy level decreases from -4.9 eV to -5.0 eV. The energy levels of the LUMO in the “closed” and “open” state of PCM are -3.4 eV and -2.1 eV, respectively. Based on these values, the potential barrier height formed by the difference in LUMO energy levels with a closed state of PCM varies from 0.6 eV to 0.2 eV depending on the QD sizes. Additionally, it should be noted that the HOMO-LUMO energy levels of both closed and open state of PCM form type-I alignment⁴⁴ with respect to all three QD sizes, indicating that the direct charge transfer⁴⁷ from band edge states in QD to the PCM is not likely to occur in either configuration.

The PCM bridged QD assembly samples were prepared in a nitrogen environment glovebox through spin-coating as-synthesized QDs on a cleaned glass slide and performing ligand exchange procedure to replace the native ligands, oleates, with the PCM (see the Supporting Information for details of the sample preparation method). The carboxylic acid functional groups on both ends of the PCM readily exchange with oleates on the PbS QD surface.⁴⁸ After getting bridged and cross-linked by PCMs, the QD assemblies were no longer dispersible in solvents such as hexane or toluene. The cross-linking induced solvent orthogonality allowed the ligand exchange procedures to be repeated multiple times with the samples being thoroughly washed in between to remove excess ligand molecules. Raman spectroscopy measurements were performed on the samples to monitor the extent of the ligand exchange. As shown in Figure. S6, peaks at 1425 cm^{-1} and 1550 cm^{-1} correspond to oleate molecules as native ligands on PbS QD surface. As the number

of ligand exchange procedure increases, the intensity of these peaks gradually decreases. The sample with three cycles of ligand exchange shows almost a complete elimination of these peaks, indicating that most of the oleate molecules in the QD assembly sample has been exchanged with PCM (Figure S6).

PL measurements were performed to monitor the effect of switching PCM configuration on exciton recombination in QD assemblies (Figure 3). Samples with QD sizes of 2.9 nm, 3.6 nm, and 4.7 nm were prepared and encapsulated with two glass slides and epoxy around all edges to avoid any potential complications from ambient air exposure during the measurement. First, the samples were irradiated with 300 nm light to switch PCMs to the “closed” state and then PL spectra was taken using 750 nm light irradiation which excites the QDs only without disturbing the PCM state. Afterwards, the samples were exposed to 541 nm light to switch the PCMs to the “open” state after which PL spectra were taken with 750 nm light excitation. This process was repeated multiple times to check for cyclability. Additional details of this experimental procedure are described in the Supporting Information. Figure 3a-c show that PL intensities from all samples show reversible decrease and increase with the “open” and “closed” PCM state respectively. For 2.9 nm sized QDs, the PL intensity is ~46% higher with “open” PCM state compared to the “closed” state (Figure 3a and 3d). The differences in the PL intensity are considerably smaller for bigger QDs with ~25% higher for 3.6 nm QDs (Figure 3b and 3e) and ~23% higher for 4.7 nm QDs (Figure 3c and 3f) for the “open” PCM state. These results suggest that the different potential barrier heights formed by the offset in energy levels of PCM with QDs of different sizes may be influencing the fractions of excitons that go through inter-CQD dissociation. However, since other key factors such as size dependent properties of QDs, inter-QD distances, and etc. that influence exciton recombination dynamics are also different in these samples, further studies are required to

delineate them. Repeating the PL measurement cycle results in an alternating PL intensity from QDs indicating that the response in the fraction of excitons undergoing radiative recombination to switching the PCM configuration is a reversible and non-destructive process. The absorbance spectra of the samples with the PCM in “closed” and “open” states (Figure S7) show that there is no noticeable difference due to the configuration switching. Therefore, we conclude that the reversible switching of PL intensity observed in Figure 3 is not due to irreversible changes in QDs such as degradation and other processes but instead is governed by the structural changes in the PCMs that bridge QDs.

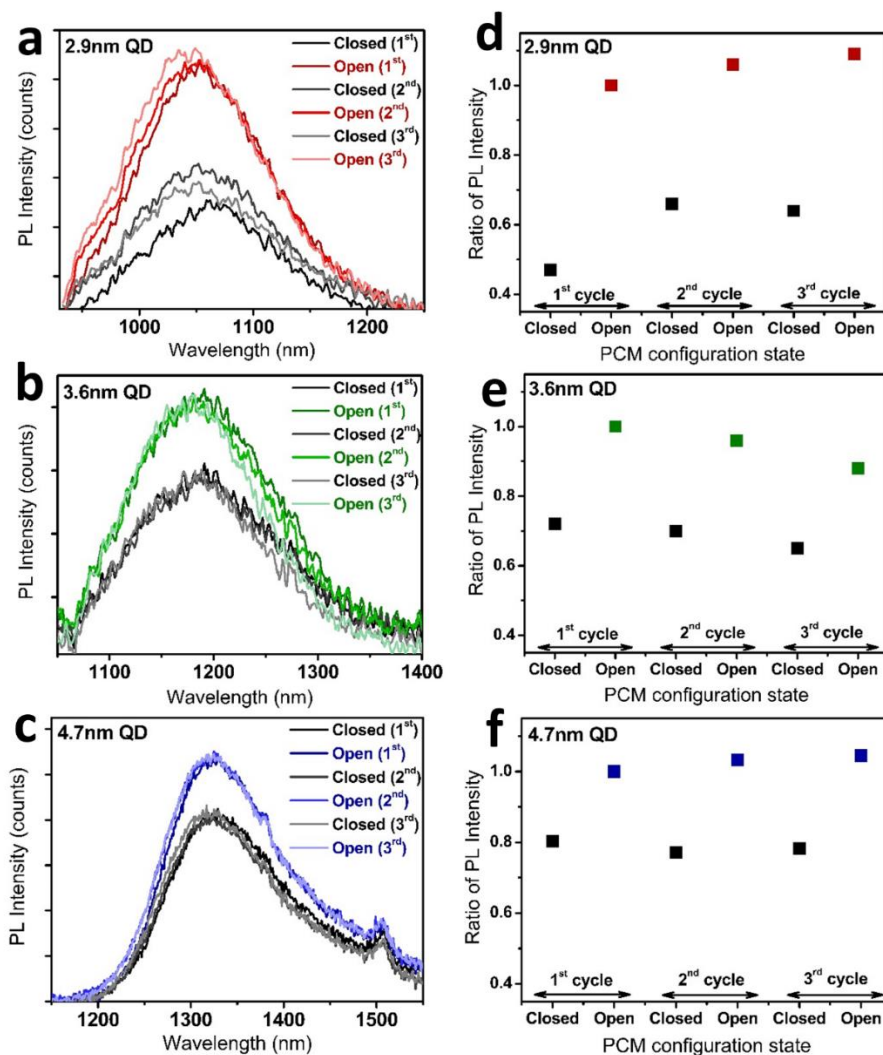


Figure 3. PL spectra of (a) 2.9 nm, (b) 3.6 nm, and (c) 4.7 nm QD assemblies after the configuration of PCM bridge molecules is switched between “closed” and “open” states. As a function of repeated cycles of PCM configuration switching, the ratio of PL intensity to the first cycle “open” configuration intensity is plotted for (d) 2.9 nm, (e) 3.6 nm, and (f) 4.7 nm QD assemblies.

To further investigate the nature of the reversible PL intensity switching, we performed time-resolved PL (TR-PL) measurement to gain insights into the exciton decay pathway. Based on the mechanism of exciton delocalization and dissociation through tunneling^{28, 49}, lower potential barrier between QDs due to “closed” PCM state would lead to faster exciton dissociation and decreased PL lifetime. Figure 4a-c show that PL lifetimes are indeed shorter in QDs when the PCM is in the “closed” state compared to the “open” state. To quantify the lifetimes, bi-exponential decay functions were fitted and the lifetime values were calculated through weighted averaging of the two terms.⁵⁰ Our results show that the 2.9 nm QD assembly shows the biggest differences in the PL lifetimes of 31 ns and 61 ns when the PCMs are in the “closed” and “open” state respectively. The differences in the PL lifetimes in 3.6 and 4.7 nm QD assemblies also show the same trend but to a smaller degree compared to the 2.9 nm QD sample. These trends in PL lifetimes are consistent with the differences in PL spectra intensity as a function of PCM state and QD size (Figure 3).

The shorter PL lifetime and lower PL intensity of QD assembly with the “closed” PCM state are consistent with our proposed inter-QD exciton dissociation mechanism^{28, 49} due to lower inter-QD potential barrier height. It is possible that the change in the PL behavior may also draw contributions from any changes in inter-QD distances due to the PCM configuration switch. However, based on the molecular structure of the dithienylethene backbone, the PCM employed in this work is expected to have a difference of only ~ 1 Å in lateral length upon configuration change. To experimentally quantify inter-QD distances with different PCM configurations, we

performed grazing incidence small angle x-ray scattering (GISAXS) measurements at the National Synchrotron Light Source II at Brookhaven National Laboratory (see the Supporting Information for detailed GISAXS measurement method). The GISAXS scattering plots of 2.9 nm QD assemblies with the “open” and “closed” PCM states are shown in Figure S8a-b and their azimuthally integrated scattering X-ray intensities show peaks that correspond to the periodicity in inter-QD spacing (Figure S8c-d). The inter-QD distance values with the “open” and “closed” PCM state in samples with different QD sizes are summarized in Table S1. The amount of change in measured inter-QD distance between the “open” and “closed” PCM states varies from 0.07 Å to 1.4 Å across different samples. It is likely that the small change of ~ 1.0 Å in the inter-QD distance change is not the major cause for the observed PL behavior. However, further studies are needed to quantify and delineate contributions from various different parameters.

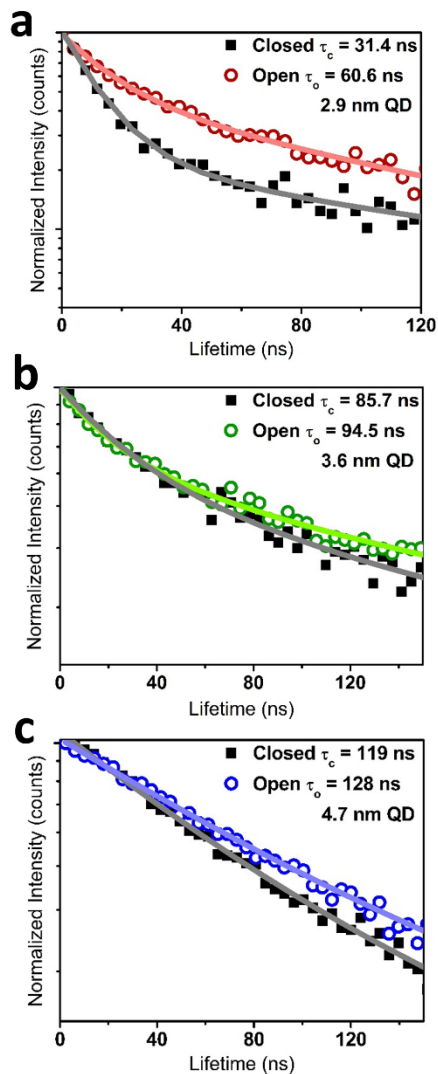


Figure 4. Time-resolved PL results from (a) 2.9 nm QD, (b) 3.6 nm QD, and (c) 4.7 nm QD assemblies with “open” or “closed” configuration of PCM bridges.

Other possible mechanisms responsible for the observed changes in PL intensity and lifetime are surface charge trapping, Förster resonant energy transfer (FRET)⁵¹⁻⁵⁴ to some energy acceptors, and direct charge transfer^{47, 55-56} from QD to PCM molecules. Based on the fact that the PL and TR-PL measurements were performed on the identical sample wherein the only difference was in the history of light exposure sequence to switch the PCM configuration, we argue that

changes in charge trapping amount being responsible for the reversible changes in PL as observed in this work are highly unlikely. As for the FRET mechanism, which is an energy transfer process through dipole–dipole interaction, occurs when there is a resonance in energy between the electronic transitions in the donor and the acceptor. As such, the PL spectra of the QDs need to overlap with the absorption energy of any suitable acceptors nearby. Possible energy acceptors are surface ligands⁵⁷⁻⁵⁹ and nearby QDs that have not been photoexcited^{28, 60-61}. As shown in Figure 2a and 2c, the light absorption by the PCM occurs in the UV-visible spectrum range which is significantly higher in energy than the near-IR PL of the QDs, indicating that FRET from QDs to PCM is not responsible for the observed PL changes. Also, in our samples, neighboring QDs are exactly identical before and after the PCM configuration change and therefore changes in FRET between QDs, if any, will be insignificant. Lastly, we consider the possibility of direct charge transfer from QDs to PCM in the “closed” state being responsible for the reduction in PL intensity and lifetime observed in this work. Based on the information shown in Figure 2d, the type-I energy alignment between QD and PCM would not facilitate direct charge transfer from the QD to the PCM. Moreover, previous studies in the literature show that direct charge transfer from PbS QD to surface ligands typically occur in the picosecond to few nanosecond time scale⁵⁷ which is more than an order of magnitude faster than the PL lifetimes observed in this work, suggesting distinctive mechanisms.

In order to confirm the absence of direct charge transfer from PbS QD to the PCM more directly, we performed a control experiment by employing a mono-esterified PCM (also referred as compound **7** in Scheme S1 of the Supporting Information) that has the identical chemical structure to the PCM except for an esterified group on one end of the dithienylethene (Figure 5). Because binding to PbS QD surface occurs through a deprotonated carboxylate by replacing native

oleates⁴⁸, the mono-esterified PCM molecule will not cross-link two QDs, thereby eliminating the possibility of inter-QD exciton dissociation mechanism. If the direct charge injection from the QD to the PCM is indeed the dominant non-radiative pathway, then a significant PL quenching from QDs should occur when bound with mono-esterified PCM. The control experiment was conducted using the solution-state QD sample in which the mono-esterified PCMs were added to the QD solution (Figure S9). Conducting the PL measurements with solution samples, instead of solid-state thin film samples, further ensures that the QDs are isolated from each other to better isolate the effect of charge transfer from QDs to surface ligands, if any. Our result (Figure 5) shows that there is no difference in PL intensity when the mono-esterified PCM is switched between “open” and “closed” state. We also performed similar experiments with solution form samples with the PCM (compound **6** with carboxylic acid groups on both ends) by adding the same concentration of ligands into the solution. In contrast to the mono-esterified PCM experiment, we observed switchable PL intensity from the QD solution samples with PCM depending on the PCM configuration (Figure S10). These results indicate that, with PCM addition, some fractions of QDs become cross-linked by PCMs into dimers, trimers and etc. that maintain colloidal stability and the inter-QD exciton dissociation becomes enhanced with the “closed” PCM configuration in those cross linked QD species in solution. In contrast, mono-esterified PCM cannot bridge multiple QDs with each other and the exciton dissociation is not influenced by the configuration of the mono-esterified PCMs. Therefore, these control experiments show that the direct charge transfer from QD to PCM does not occur in these systems but instead the changes in PL intensity observed in this work is due to changes in the amount of excitons going through inter-QD tunneling and dissociation.

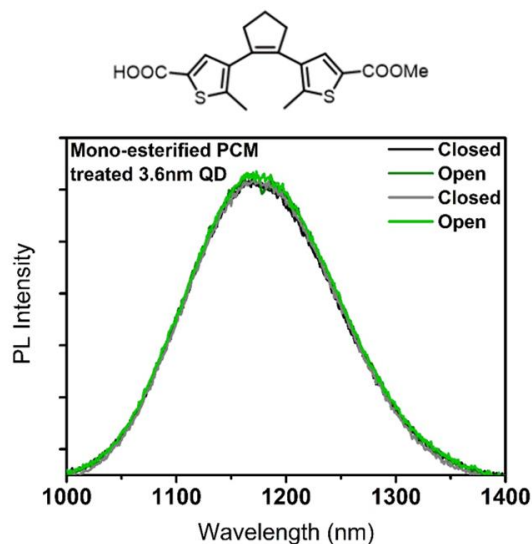


Figure 5. PL spectra of 3.6 nm QDs with mono-esterified PCMs (compound 7) ligands in “closed” or “open” configuration.

4.5. Conclusion

In summary, this study shows that lowering the inter-QD potential barrier height increases the exciton delocalization and dissociation through tunneling. To the best of our knowledge, this study is the first to investigate the impact of bridge molecule configuration on exciton dynamics all with identical donor-acceptor QD pairs. This work demonstrates that exploiting the configuration changes of photochromic molecules can provide fertile future directions for QD, molecular electronics and nanoscale charge transfer research communities. For application, the switchable PL intensity from QD found in this work can provide unique opportunities for optical memory and computing technologies. The major challenges facing the current state-of-the-art non-volatile on-chip compatible optical memory materials, such as phase change materials and photochromic molecules, are that phase change materials require large energy light excitations to induce melting and photochromic molecules lack non-destructive readout capabilities due to the

readout operation itself causing the switch because both operations use the same wavelength light. In contrast, our PCM bridged QD assemblies exhibit near-IR light emission that can be increased or decreased with UV and visible light exposure. The “read” operations can be performed all in near-IR region that does not cause flipping of PCM configuration. Therefore, the findings in this study can lead to solving the photochromic materials switching their configuration during the “read” operation and provide a new class of materials for non-volatile optical memory and computing applications.

4.6. Reference

1. Kamat, P. V. Quantum Dot Solar Cells. Semiconductor Nanocrystals as Light Harvesters. *J. Phys. Chem. C* **2008**, *112* (48), 18737-18753.
2. Klimov, V. I. Spectral and Dynamical Properties of Multiexcitons in Semiconductor Nanocrystals. *Annu. Rev. Phys. Chem.* **2007**, *58*, 635-673.
3. Murray, C. B.; Kagan, a. C.; Bawendi, M. Synthesis and Characterization of Monodisperse Nanocrystals and Close-Packed Nanocrystal Assemblies. *Annu. Rev. Mater. Sci.* **2000**, *30* (1), 545-610.
4. Nozik, A. J.; Beard, M. C.; Luther, J. M.; Law, M.; Ellingson, R. J.; Johnson, J. C. Semiconductor Quantum Dots and Quantum Dot Arrays and Applications of Multiple Exciton Generation to Third-Generation Photovoltaic Solar Cells. *Chem. Rev.* **2010**, *110* (11), 6873-6890.
5. Talapin, D. V.; Lee, J.-S.; Kovalenko, M. V.; Shevchenko, E. V. Prospects of Colloidal Nanocrystals for Electronic and Optoelectronic Applications. *Chem. Rev.* **2010**, *110* (1), 389-458.
6. Tang, J.; Sargent, E. H. Infrared Colloidal Quantum Dots for Photovoltaics: Fundamentals and Recent Progress. *Adv. Mater.* **2011**, *23* (1), 12-29.
7. Wise, F. W. Lead Salt Quantum Dots: The Limit of Strong Quantum Confinement. *Acc. Chem. Res.* **2000**, *33* (11), 773-780.
8. Brus, L. E., Electron–Electron and Electron-Hole Interactions in Small Semiconductor Crystallites: The Size Dependence of the Lowest Excited Electronic State. *J. Chem. Phys.* **1984**, *80* (9), 4403-4409.
9. Ekimov, A. I.; Efros, A. L.; Onushchenko, A. A. Quantum Size Effect in Semiconductor Microcrystals. *Solid State Commun.* **1985**, *56* (11), 921-924.
10. Bian, K.; Choi, J. J.; Kaushik, A.; Clancy, P.; Smilgies, D.-M.; Hanrath, T. Shape-Anisotropy Driven Symmetry Transformations in Nanocrystal Superlattice Polymorphs. *ACS Nano* **2011**, *5* (4), 2815-2823.

11. Chen, Q.; Bae, S. C.; Granick, S., Directed Self-Assembly of a Colloidal Kagome Lattice. *Nature* **2011**, *469* (7330), 381-384.
12. Choi, J. J.; Bealing, C. R.; Bian, K.; Hughes, K. J.; Zhang, W.; Smilgies, D.-M.; Hennig, R. G.; Engstrom, J. R.; Hanrath, T. Controlling Nanocrystal Superlattice Symmetry and Shape-Anisotropic Interactions Through Variable Ligand Surface Coverage. *J. Am. Chem. Soc.* **2011**, *133* (9), 3131-3138.
13. Choi, J. J.; Bian, K.; Baumgardner, W. J.; Smilgies, D.-M.; Hanrath, T. Interface-Induced Nucleation, Orientational Alignment and Symmetry Transformations in Nanocube Superlattices. *Nano Lett.* **2012**, *12* (9), 4791-4798.
14. Damasceno, P. F.; Engel, M.; Glotzer, S. C. Predictive Self-Assembly of Polyhedra Into Complex Structures. *Science* **2012**, *337* (6093), 453-457.
15. Dong, A.; Chen, J.; Vora, P. M.; Kikkawa, J. M.; Murray, C. B. Binary Nanocrystal Superlattice Membranes Self-Assembled at the Liquid–Air Interface. *Nature* **2010**, *466* (7305), 474-477.
16. Markovich, G.; Collier, C. P.; Henrichs, S. E.; Remacle, F.; Levine, R. D.; Heath, J. R. Architectonic Quantum Dot Solids. *Acc. Chem. Res.* **1999**, *32* (5), 415-423.
17. Claridge, S. A.; Castleman Jr, A.; Khanna, S. N.; Murray, C. B.; Sen, A.; Weiss, P. S. Cluster-Assembled Materials. *ACS Nano* **2009**, *3* (2), 244-255.
18. Bakkers, E.; Roest, A.; Marsman, A.; Jenneskens, L.; De Jong-Van Steensel, L.; Kelly, J.; Vanmaekelbergh, D. Characterization of Photoinduced Electron Tunneling in gold/SAM/Q-CdSe Systems by Time-Resolved Photoelectrochemistry. *J. Phys. Chem. B* **2000**, *104* (31), 7266-7272.
19. Murphy, J. E.; Beard, M. C.; Nozik, A. J. Time-Resolved Photoconductivity of PbSe Nanocrystal Arrays. *J. Phys. Chem. B* **2006**, *110* (50), 25455-25461.

20. Mora-Seró, I.; Giménez, S.; Moehl, T.; Fabregat-Santiago, F.; Lana-Villareal, T.; Gómez, R.; Bisquert, J. Factors Determining the Photovoltaic Performance of a CdSe Quantum Dot Sensitized Solar Cell: The Role of the Linker Molecule and of the Counter Electrode. *Nanotechnology* **2008**, *19* (42), 424007.
21. Zabet-Khosousi, A.; Dhirani, A.-A. Charge Transport in Nanoparticle Assemblies. *Chem. Rev.* **2008**, *108* (10), 4072-4124.
22. Liu, Y.; Gibbs, M.; Puthussery, J.; Gaik, S.; Ihly, R.; Hillhouse, H. W.; Law, M. Dependence of Carrier Mobility on Nanocrystal Size and Ligand Length in PbSe Nanocrystal Solids. *Nano Lett.* **2010**, *10* (5), 1960-1969.
23. Zarghami, M. H.; Liu, Y.; Gibbs, M.; Gebremichael, E.; Webster, C.; Law, M. p-Type PbSe and PbS Quantum Dot Solids Prepared with Short-Chain Acids and Diacids. *ACS Nano* **2010**, *4* (4), 2475-2485.
24. Hyun, B.-R.; Bartnik, A.; Sun, L.; Hanrath, T.; Wise, F. Control of Electron Transfer from Lead-Salt Nanocrystals to TiO₂. *Nano Lett.* **2011**, *11* (5), 2126-2132.
25. Tang, J.; Kemp, K. W.; Hoogland, S.; Jeong, K. S.; Liu, H.; Levina, L.; Furukawa, M.; Wang, X.; Debnath, R.; Cha, D. Colloidal-Quantum-Dot Photovoltaics Using Atomic-Ligand Passivation. *Nat. Mater.* **2011**, *10* (10), 765-771.
26. Gao, Y.; Aerts, M.; Sandeep, C. S.; Talgorn, E.; Savenije, T. J.; Kinge, S.; Siebbeles, L. D.; Houtepen, A. J. Photoconductivity of PbSe Quantum-Dot Solids: Dependence on Ligand Anchor Group and Length. *ACS Nano* **2012**, *6* (11), 9606-9614.
27. Jeong, K. S.; Tang, J.; Liu, H.; Kim, J.; Schaefer, A. W.; Kemp, K.; Levina, L.; Wang, X.; Hoogland, S.; Debnath, R. Enhanced Mobility-Lifetime Products in PbS Colloidal Quantum Dot Photovoltaics. *ACS Nano* **2012**, *6* (1), 89-99.

28. Choi, J. J.; Luria, J.; Hyun, B.-R.; Bartnik, A. C.; Sun, L.; Lim, Y.-F.; Marohn, J. A.; Wise, F. W.; Hanrath, T. Photogenerated Exciton Dissociation in Highly Coupled Lead Salt Nanocrystal Assemblies. *Nano Lett.* **2010**, *10* (5), 1805-1811.
29. Sun, L.; Choi, J. J.; Stachnik, D.; Bartnik, A. C.; Hyun, B.-R.; Malliaras, G. G.; Hanrath, T.; Wise, F. W. Bright Infrared Quantum-Dot Light-Emitting Diodes Through Inter-Dot Spacing Control. *Nat. Nanotechnol.* **2012**, *7* (6), 369-373.
30. Choi, J. J.; Lim, Y.-F.; Santiago-Berrios, M. E. B.; Oh, M.; Hyun, B.-R.; Sun, L.; Bartnik, A. C.; Goedhart, A.; Malliaras, G. G.; Abruna, H. D. PbSe Nanocrystal Excitonic Solar Cells. *Nano Lett.* **2009**, *9* (11), 3749-3755.
31. Luther, J. M.; Law, M.; Beard, M. C.; Song, Q.; Reese, M. O.; Ellingson, R. J.; Nozik, A. J. Schottky Solar Cells Based on Colloidal Nanocrystal Films. *Nano Lett.* **2008**, *8* (10), 3488-3492.
32. Luther, J. M.; Law, M.; Song, Q.; Perkins, C. L.; Beard, M. C.; Nozik, A. J. Structural, Optical, and Electrical Properties of Self-Assembled Films of PbSe Nanocrystals Treated with 1, 2-ethanedithiol. *ACS Nano* **2008**, *2* (2), 271-280.
33. Koleilat, G. I.; Levina, L.; Shukla, H.; Myrskog, S. H.; Hinds, S.; Pattantyus-Abraham, A. G.; Sargent, E. H. Efficient, Stable Infrared Photovoltaics Based on Solution-Cast Colloidal Quantum Dots. *ACS Nano* **2008**, *2* (5), 833-840.
34. Fafarman, A. T.; Koh, W.-k.; Diroll, B. T.; Kim, D. K.; Ko, D.-K.; Oh, S. J.; Ye, X.; Doan-Nguyen, V.; Crump, M. R.; Reifsnyder, D. C. Thiocyanate-Capped Nanocrystal Colloids: Vibrational Reporter of Surface Chemistry and Solution-Based Route to Enhanced Coupling in Nanocrystal Solids. *J. Am. Chem. Soc.* **2011**, *133* (39), 15753-15761.

35. Koh, W.-k.; Saudari, S. R.; Fafarman, A. T.; Kagan, C. R.; Murray, C. B. Thiocyanate-Capped PbS Nanocubes: Ambipolar Transport Enables Quantum Dot Based Circuits on a Flexible Substrate. *Nano Lett.* **2011**, *11* (11), 4764-4767.
36. Kovalenko, M. V.; Scheele, M.; Talapin, D. V. Colloidal Nanocrystals with Molecular Metal Chalcogenide Surface Ligands. *Science* **2009**, *324* (5933), 1417-1420.
37. Lee, J.-S.; Kovalenko, M. V.; Huang, J.; Chung, D. S.; Talapin, D. V. Band-Like Transport, High Electron Mobility and High Photoconductivity in All-Inorganic Nanocrystal Arrays. *Nat. Nanotechnol.* **2011**, *6* (6), 348-352.
38. Nag, A.; Kovalenko, M. V.; Lee, J.-S.; Liu, W.; Spokoyny, B.; Talapin, D. V. Metal-Free Inorganic Ligands for Colloidal Nanocrystals: S^{2-} , HS^- , Se^{2-} , HSe^- , Te^{2-} , HTe^- , TeS_3^{2-} , OH^- , and NH_2^- as Surface Ligands. *J. Am. Chem. Soc.* **2011**, *133* (27), 10612-10620.
39. Fukaminato, T.; Ishida, S.; Métivier, R. Photochromic Fluorophores at the Molecular and Nanoparticle Levels: Fundamentals and Applications of Diarylethenes. *NPG Asia Mater.* **2018**, *10* (9), 859-881.
40. Irie, M. Photochromism of Diarylethene Single Molecules and Single Crystals. *Photochem. Photobiol. Sci.* **2010**, *9* (12), 1535-1542.
41. Irie, M., Diarylethenes for Memories and Switches. *Chem. Rev.* **2000**, *100* (5), 1685-1716.
42. Tian, H.; Yang, S. Recent Progresses on Diarylethene Based Photochromic Switches. *Chem. Soc. Rev.* **2004**, *33* (2), 85-97.
43. Zhang, J.; Zou, Q.; Tian, H. Photochromic Materials: More Than Meets the Eye. *Adv. Mater.* **2013**, *25* (3), 378-399.

44. Guirado, G.; Coudret, C.; Hliwa, M.; Launay, J.-P. Understanding Electrochromic Processes Initiated by Dithienylcyclopentene Cation-Radicals. *J. Phys. Chem. B* **2005**, *109* (37), 17445-17459.
45. Owrutsky, J.; Nelson, H.; Baronavski, A.; Kim, O.-K.; Tsivgoulis, G.; Gilat, S.; Lehn, J.-M. Optical Properties and Dynamics of a Photochromic Bisthienylethene in Solution and in a Polymer Film. *Chem. Phys. Lett.* **1998**, *293* (5-6), 555-563.
46. Jasieniak, J.; Califano, M.; Watkins, S. E. Size-Dependent Valence and Conduction Band-Edge Energies of Semiconductor Nanocrystals. *ACS Nano* **2011**, *5* (7), 5888-5902.
47. Padgaonkar, S.; Eckdahl, C. T.; Sowa, J. K.; López-Arteaga, R.; Westmoreland, D. E.; Woods, E. F.; Irgen-Giorgio, S.; Nagasing, B.; Seideman, T.; Hersam, M. C. Light-Triggered Switching of Quantum Dot Photoluminescence Through Excited-State Electron Transfer to Surface-Bound Photochromic Molecules. *Nano Lett.* **2021**, *21* (1), 854-860.
48. Anderson, N. C.; Hendricks, M. P.; Choi, J. J.; Owen, J. S. Ligand Exchange and the Stoichiometry of Metal Chalcogenide Nanocrystals: Spectroscopic Observation of Facile Metal-Carboxylate Displacement and Binding. *J. Am. Chem. Soc.* **2013**, *135* (49), 18536-18548.
49. Lingley, Z.; Lu, S.; Madhukar, A. The Dynamics of Energy and Charge Transfer in Lead Sulfide Quantum Dot Solids. *J. Appl. Phys.* **2014**, *115* (8), 084302.
50. Lakowicz, J. R. *Principles of Fluorescence Spectroscopy*; 3rd ed.; Springer, 2006.
51. Dworak, L.; Reuss, A. J.; Zastrow, M.; Rück-Braun, K.; Wachtveitl, J. Discrimination Between FRET and Non-FRET Quenching in a Photochromic CdSe Quantum Dot/Dithienylethene Dye System. *Nanoscale* **2014**, *6* (23), 14200-14203.

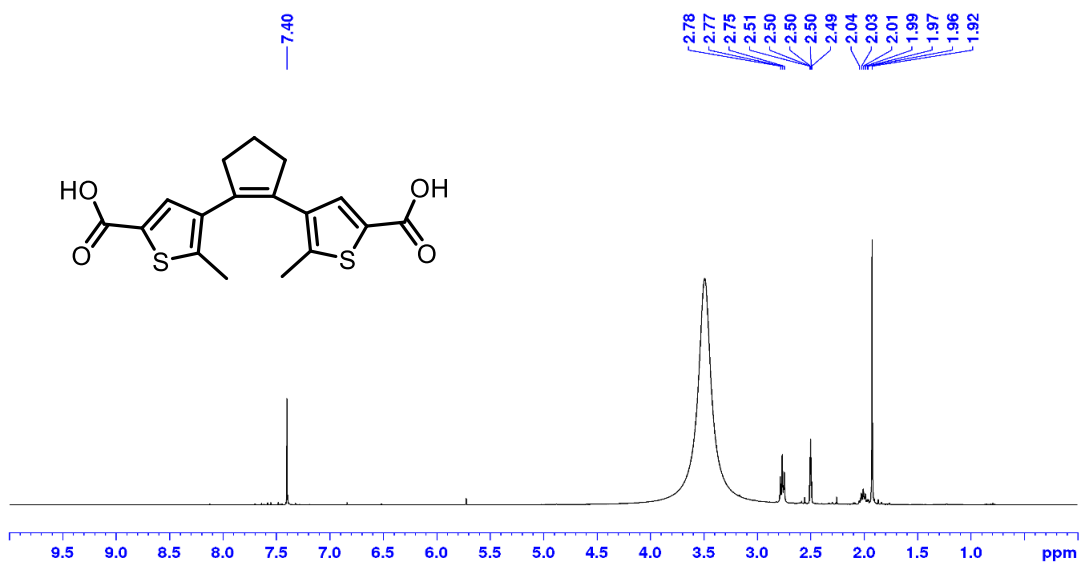
52. Yano, N.; Yamauchi, M.; Kitagawa, D.; Kobatake, S.; Masuo, S. Photoluminescence On/Off Switching of a Single Colloidal Quantum Dot Using Photochromic Diarylethene. *J. Phys. Chem. C* **2020**, *124* (31), 17423-17429.
53. Seto, Y.; Yamada, R.; Kitagawa, D.; Kim, D.; Kobatake, S. Photoluminescence ON/OFF Switching of CdSe/ZnS Core/Shell Quantum Dots Coated with Diarylethene Ligands. *Chem. Lett.* **2019**, *48* (11), 1394-1397.
54. Akaishi, Y.; Pramata, A. D.; Tominaga, S.; Kawashima, S.; Fukaminato, T.; Kida, T. Reversible ON/OFF Switching of Photoluminescence from CsPbX₃ Quantum Dots Coated with Silica Using Photochromic Diarylethene. *Chem. Commun.* **2019**, *55* (56), 8060-8063.
55. Krivenkov, V.; Samokhvalov, P.; Zvaigzne, M.; Martynov, I.; Chistyakov, A.; Nabiev, I. Ligand-Mediated Photobrightening and Photodarkening of CdSe/ZnS Quantum Dot Ensembles. *J. Phys. Chem. C* **2018**, *122* (27), 15761-15771.
56. Saeed, S.; Yin, J.; Khalid, M. A.; Channar, P. A.; Shabir, G.; Saeed, A.; Nadeem, M. A.; Soci, C.; Iqbal, A. Photoresponsive Azobenzene Ligand as an Efficient Electron Acceptor for Luminous CdTe Quantum Dots. *J. Photochem. Photobiol. A: Chem.* **2019**, *375*, 48-53.
57. Knowles, K. E.; Peterson, M. D.; McPhail, M. R.; Weiss, E. A. Exciton Dissociation within Quantum Dot–Organic Complexes: Mechanisms, Use as a Probe of Interfacial Structure, and Applications. *J. Phys. Chem. C* **2013**, *117* (20), 10229-10243.
58. Harris, R. D.; Bettis Homan, S.; Kodaimati, M.; He, C.; Nepomnyashchii, A. B.; Swenson, N. K.; Lian, S.; Calzada, R.; Weiss, E. A. Electronic Processes within Quantum Dot-Molecule Complexes. *Chem. Rev.* **2016**, *116* (21), 12865-12919.

59. Peterson, M. D.; Cass, L. C.; Harris, R. D.; Edme, K.; Sung, K.; Weiss, E. A. The Role of Ligands in Determining the Exciton Relaxation Dynamics in Semiconductor Quantum Dots. *Annu. Rev. Phys. Chem.* **2014**, *65*, 317-339.
60. Akselrod, G. M.; Deotare, P. B.; Thompson, N. J.; Lee, J.; Tisdale, W. A.; Baldo, M. A.; Menon, V. M.; Bulović, V. Visualization of Exciton Transport in Ordered and Disordered Molecular Solids. *Nat. Commun.* **2014**, *5* (1), 1-8.
61. Gilmore, R. H.; Lee, E. M.; Weidman, M. C.; Willard, A. P.; Tisdale, W. A. Charge Carrier Hopping Dynamics in Homogeneously Broadened PbS Quantum Dot Solids. *Nano Lett.* **2017**, *17* (2), 893-901.

4.7. Supplementary Information

4.7.1. ^1H and ^{13}C NMR spectra of as-synthesized compound 6 (PCM) and compound 7 (mono-esterified PCM)

1034-128_1H_DMSO-d6-400_post column



1026-028_13C_DMSO-d6-100_post column

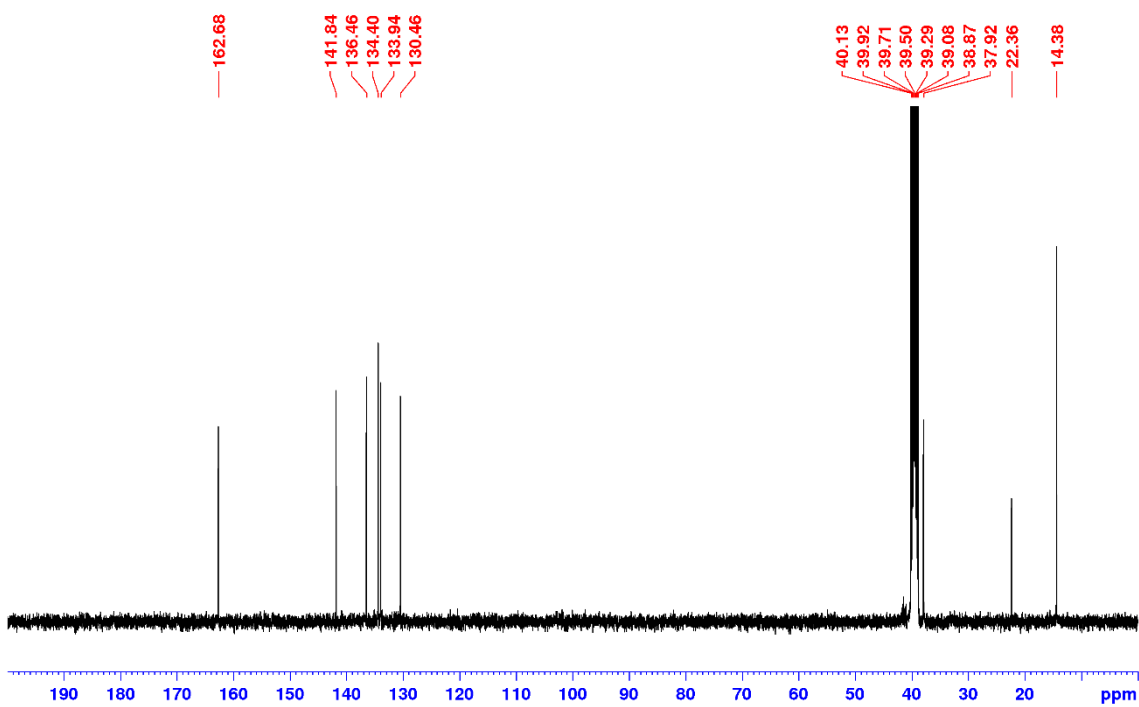
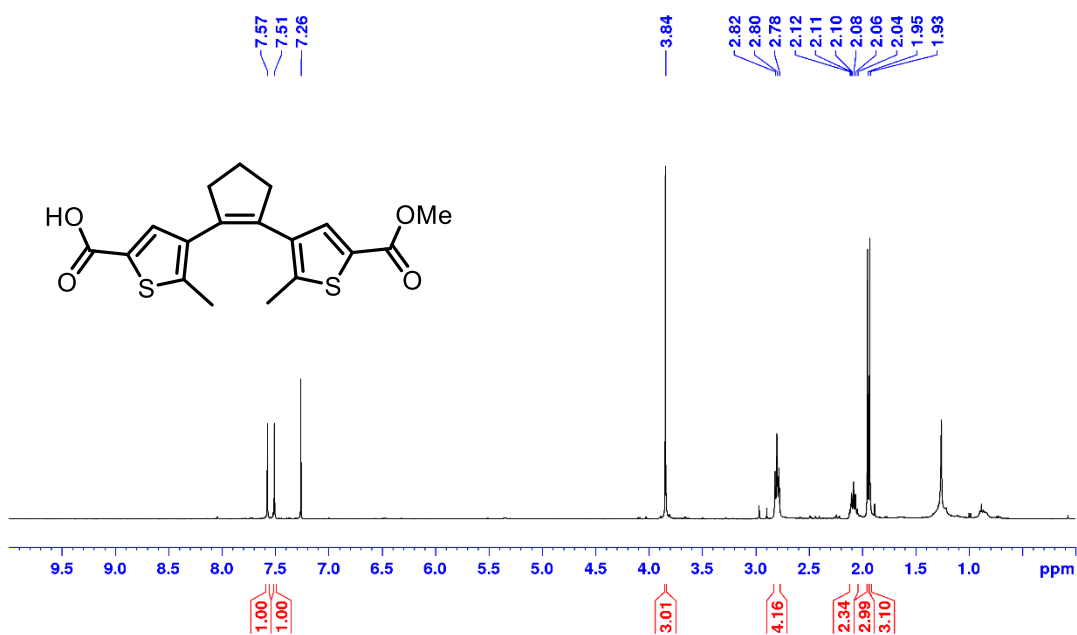


Figure S1. ¹H and ¹³C NMR spectra of compound **6** in DMSO-d₆.

1034-183_1H_CDCl3-400_post column



1034-183_13C_CDCl3-100_post column

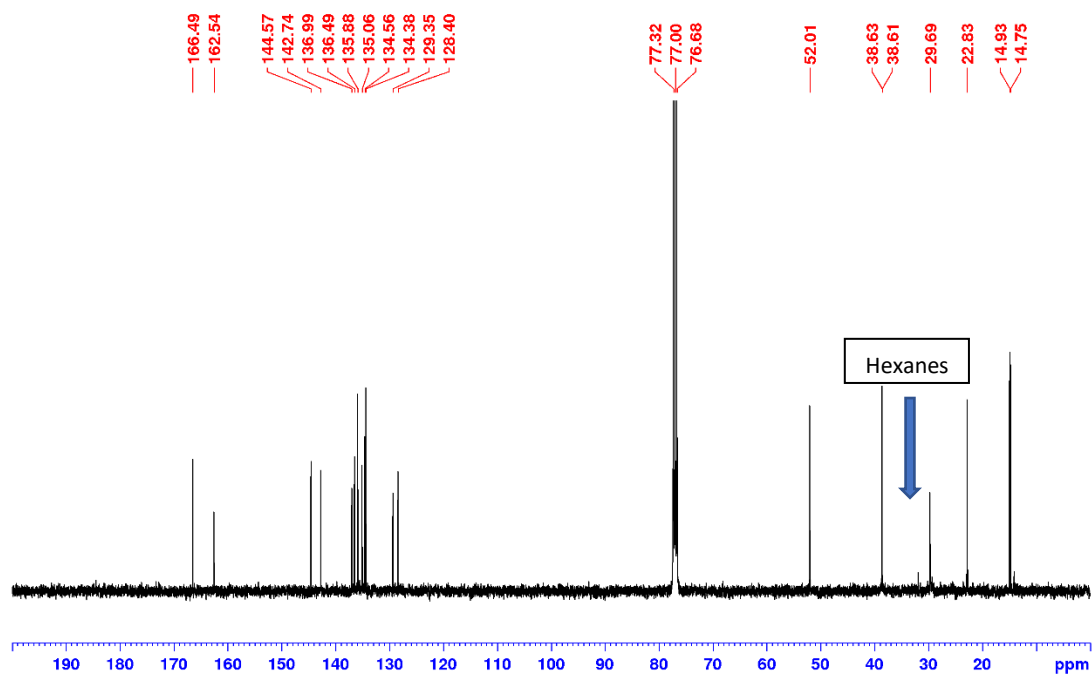


Figure S2. ¹H and ¹³C NMR spectra of compound 7 in CDCl₃.

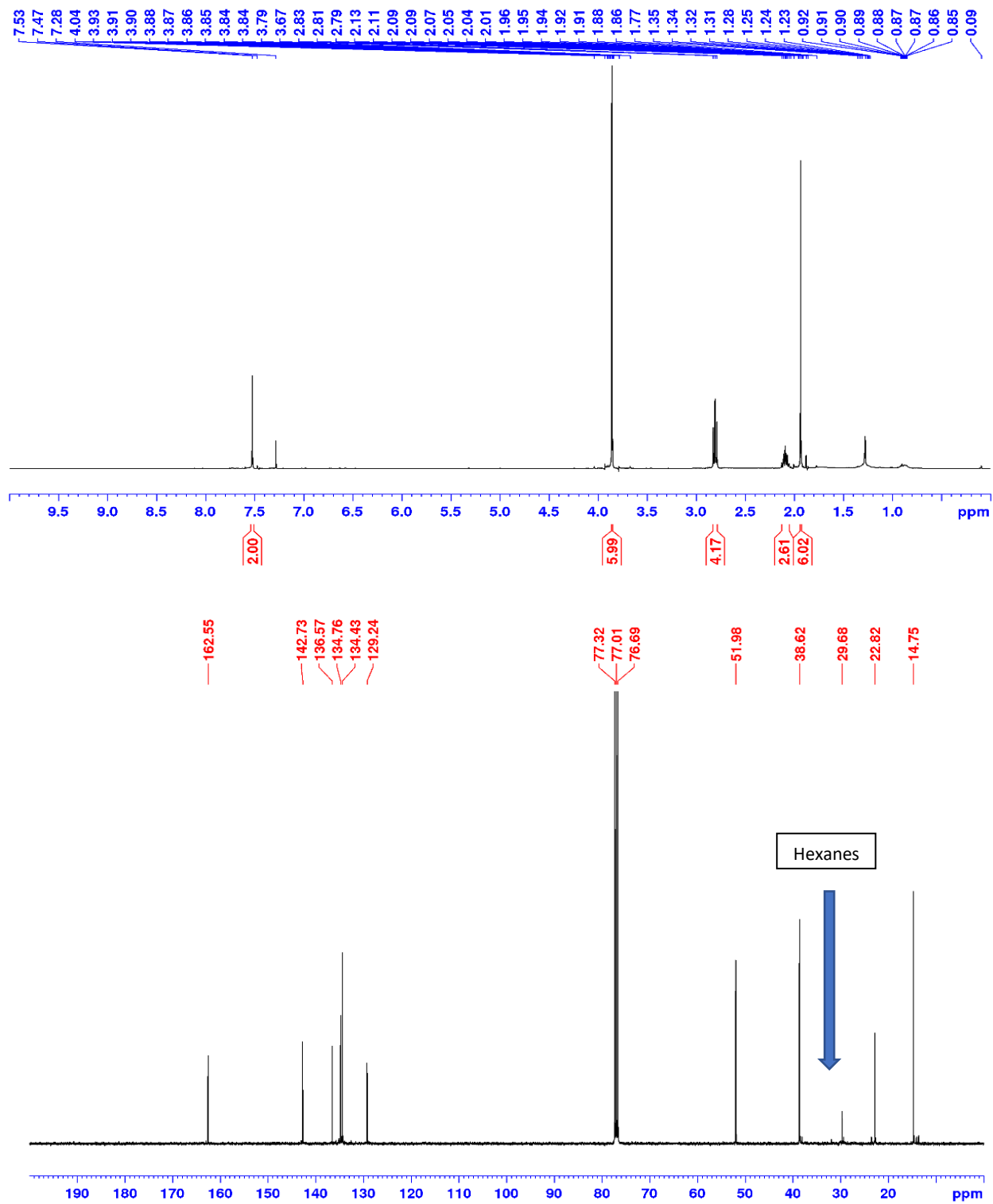


Figure S3. ¹H and ¹³C NMR spectra of compound **8** in CDCl₃.

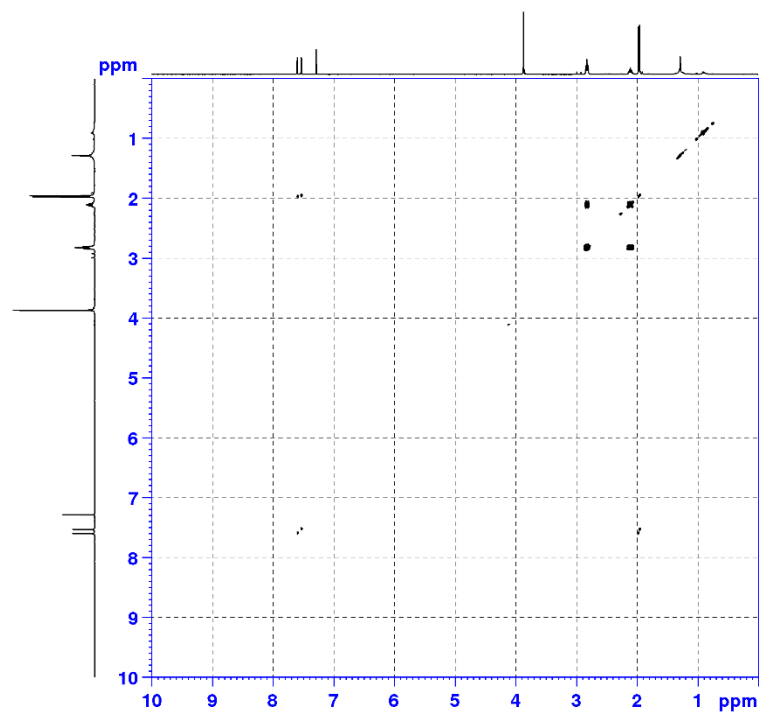
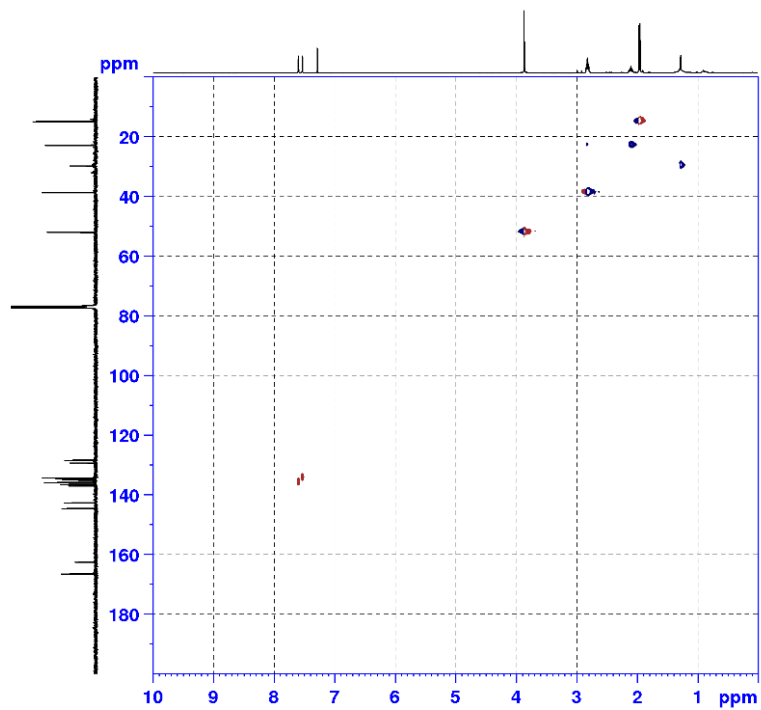


Figure S4. HSQC and COSY NMR spectra of compound **7** in CDCl₃.

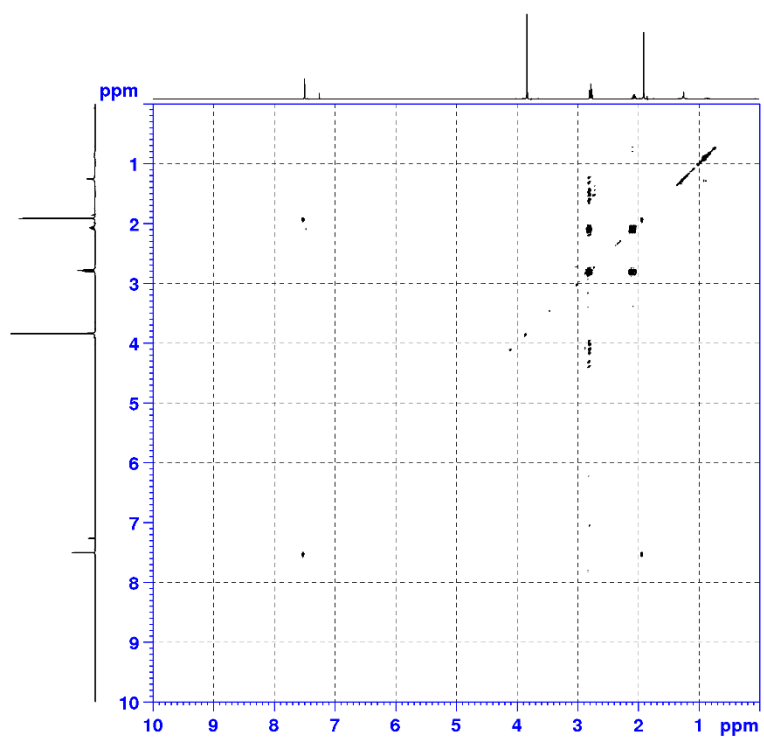
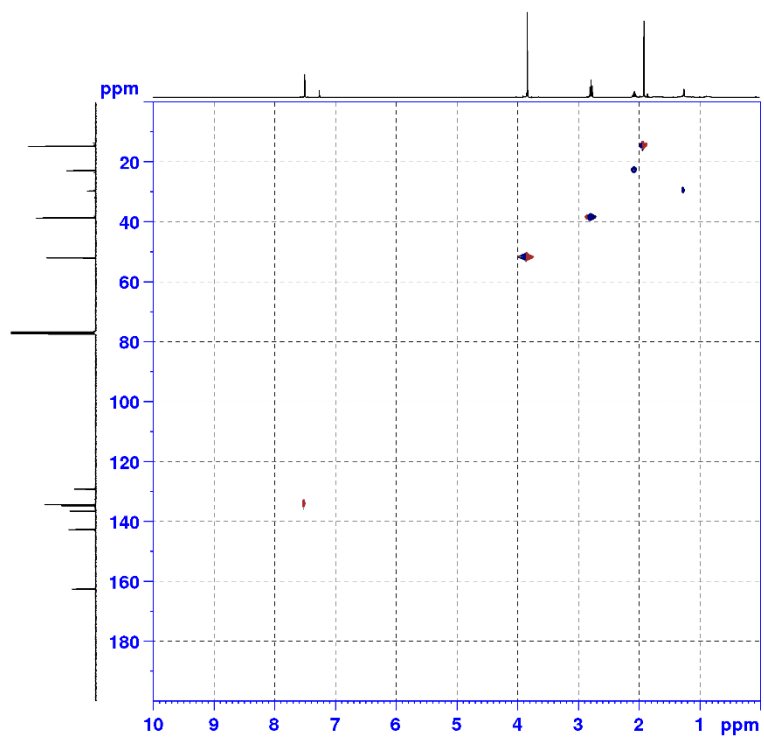


Figure S5. HSQC and COSY NMR spectra of compound **8** in CDCl₃.

4.7.2. Raman spectra for probing ligand exchange on PCM treated QD films

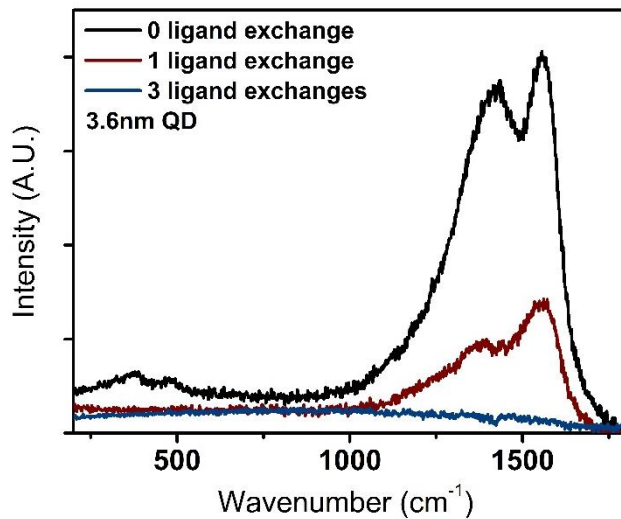


Figure S6. Raman spectra of QD thin film samples with different number of ligand exchange treatment with PCM.

4.7.3. Absorbance spectra of PCM bridged 3.6nm QD assembly with closed and open PCM state

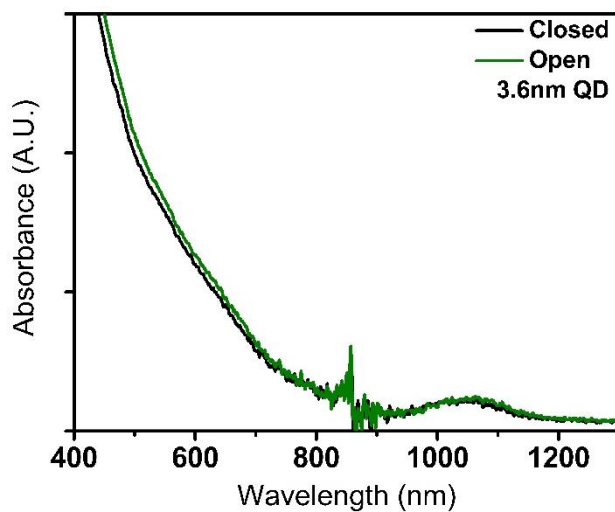


Figure S7. Absorbance spectra of 3.6 nm QD assembly with “closed” PCM (black) and “open” PCM (green).

4.7.4. GISAXS scattering images and integrated intensity plots of 2.9 nm QD films with a closed and open PCM state

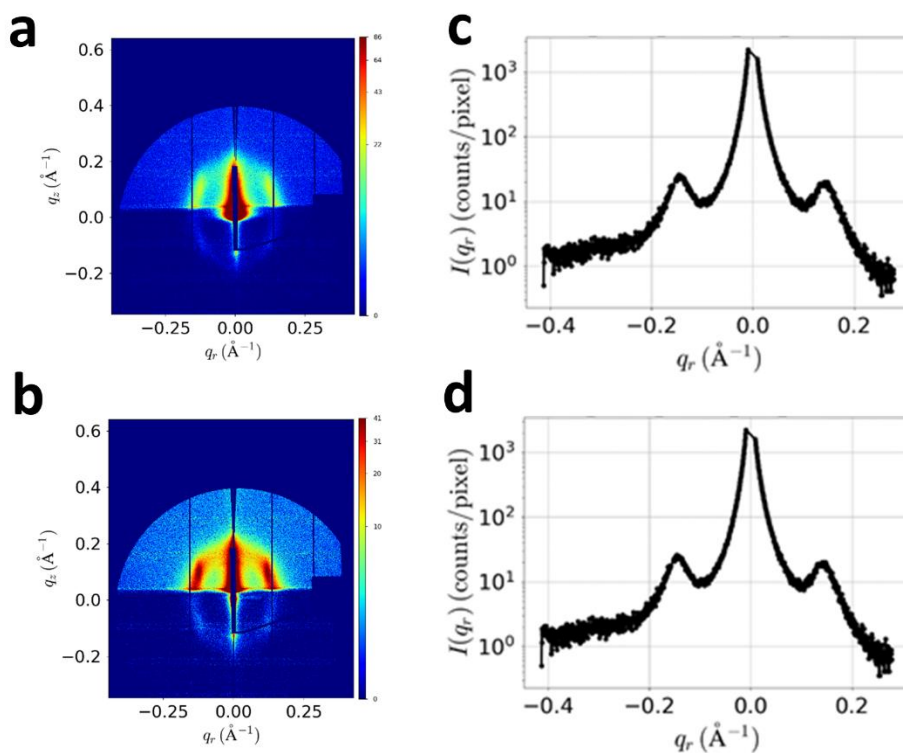


Figure S8. The GISAXS patterns of 2.9nm QD samples with (a) “closed” PCM state and (b) “open” PCM state and the integrated intensity plots as a function of reciprocal-space of (c) “closed” PCM state and (d) “open” PCM state. These results were obtained using x-ray beam incident angle of 0.20° .

4.7.5. The average inter-QD distance values of various QD size assemblies with open and closed PCM state

QD size	PCM – “Closed” state Average Inter-QD Distance	PCM – “Open” state Average Inter-QD Distance
2.9 nm	43.8 Å	45.2 Å
3.6 nm	48.7 Å	48.0 Å
4.7 nm	64.7 Å	65.9 Å

Table S1. Inter-QD distance values obtained from GISAXS measurement. The displayed values are the average of the values obtained by measurements using an incident angle from 0.10 to 0.25°.

4.7.6. Absorbance spectra of mono-esterified PCM (compound 7) in MeOH

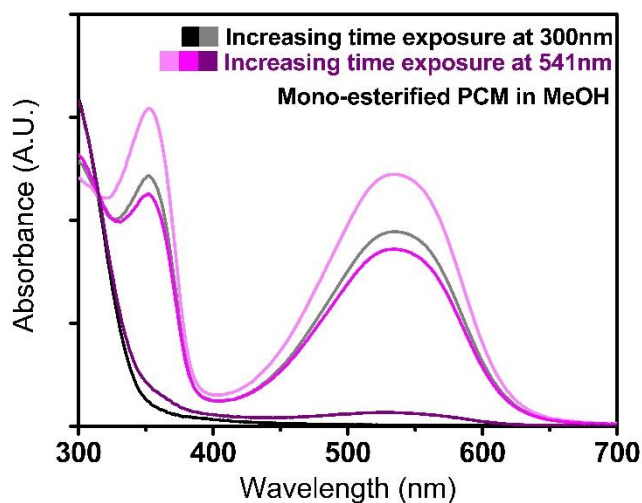


Figure S9. Absorbance spectra of mono-esterified PCM (compound 7) in MeOH after light exposure at 541 nm (magenta) and 300 nm (gray). The absorbance peak locations (350 nm and 537 nm) responsible for the “open” state closely resemble those observed in the PCM (compound 6) in Figure 2a.

4.7.7. PL cycle of PCMs treated 3.6 nm QD solution sample

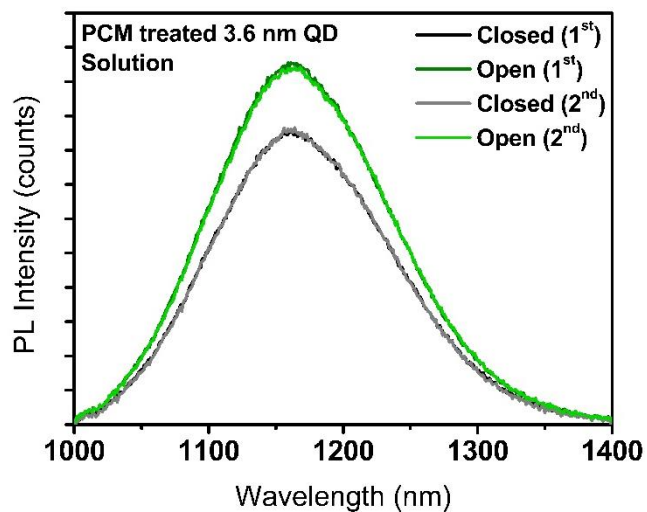


Figure S10. PL spectra of PCM (compound **6**) treated 3.6 nm QD solution. While the identical molar ratio of mono-esterified PCM (compound **7**) to QD solution does not show any noticeable PL switching response as shown in Figure 5, the PCM (compound **6**) treated QD solution shows switchable PL intensity differences upon PCM configuration change.

Chapter 5: Conclusion

The collection of work covered in this thesis attempts to provide scientific insights on the importance of the role of the ligands on charge conservation and transport in the QD or QD assembly. The ligands are not merely the entities that keep the QDs from aggregating each other and therefore preserving their unique, tunable properties; they have a significant contribution on a much broader aspect in the device engineering perspective, and a few including trap-eliminating passivants or as connectors for enhanced charge transport in the QD-based active layer. The studies presented here make an effort to help understand a nanoscale interaction between the QD and the ligand, rationalizing a method to select the one for either/both effective defect passivation or/and charge transport facilitation, by which contribution will impose a substantial impact on the overall QD-based device performance.